Dynamics and Control of a Multi-Tethered Aerostat Positioning System

by

Casey Lambert

Department of Mechanical Engineering
McGill University, Montreal

Canada

October 2006

A thesis submitted to McGill University
in partial fulfillment of the requirements of the degree of
Doctor of Philosophy

Your file Votre référence
ISBN: 978-0-494-32203-1
Our file Notre référence
ISBN: 978-0-494-32203-1

Abstract

The focus of this study is the dynamic behaviour of a novel aerial positioning system, which consists of a lighter-than-air aerostat attached to a series of actuated tethers in the form of a tripod. The objective of the positioning system is to achieve accurate station-keeping of a payload at heights up to 500 m. This work encompasses comprehensive dynamics modeling, experimental investigation, and advanced controller development and analysis of the tri-tethered aerostat system. The system's characteristics and positioning objectives are targeted to receiver placement during the operation of a large-scale radio telescope.

The experimental test facility, built at one-third scale of the proposed radio telescope, was constructed for the dual purpose of measuring the precision of the positioning system and providing a basis for validating our computational model. The main components of the experimental apparatus are a 18-m helium aerostat, three synthetic braided tethers–hundreds of meters in length, an instrumented payload, and three computer-controlled winches. The dynamics model of the tri-tethered aerostat system is achieved by discretizing it into a series of lumped-masses, and estimating the aerodynamic properties of each of its physical elements. The disturbance input to the model is provided by a wind model that includes stochastic turbulent gusts.

A series of experimental flight tests were conducted over a two-year period to study both the uncontrolled and controlled response of the system. This leads to an incremental model validation process where the passive elements of the model, such as the tethers and the aerostat are validated prior to the verification of the entire closed-loop system. The tether model shows excellent agreement with the measured response at a temporal level, while the validation of the aerostat model is conducted at a statistical level due to the uncertainty associated with recreating the actual test wind conditions.

The controlled experiments were performed using basic proportional, integral, and derivative (PID) feedback gains applied to the position error of the payload. The closed-loop system effectively reduces the standard deviation of the payload deflections to less than 10 cm over the range of operating conditions tested. A comparison of the predicted

closed-loop behaviour of the dynamics shows favourable agreement to the experimental results, indicating that the tether actuation system is modeled appropriately.

To improve on the PID controller tested in the field, various optimal control strategies are investigated that exploit the availability of our validated dynamics model. The optimal controllers, which are designed and simulated using linear time invariant versions of the dynamics model, result in approximately double the precision of the PID controller. The control system is improved further by incorporating a feedforward control input based on measurements of the primary disturbance force acting on the system. In general the advanced control techniques, tested in simulation, offer encouraging results that suggest the positioning system should exceed the requirements of the radio telescope application.

Résumé

Cette thèse porte sur l'étude de la dynamique d'un nouveau système de positionnement aérien, composé d'un aérostat attaché à une série de câbles actionnés montés en forme de trépied. L'objectif du système de positionnement est de stabiliser une charge utile à une hauteur de 500 mètres. Cette étude présente la modélisation dynamique complète, une phase d'expérimentation, ainsi que le développement et une analyse avancée du système de positionnement aérien. Les caractéristiques et la position du système sont définies en fonction d'un récepteur d'un radiotélescope à grande échelle.

Un prototype du système à l'échelle 1:3 a été développé dans le but d'évaluer la précision du système et de valider notre modèle mathématique. Les composantes principales de l'appareil expérimental sont : un aérostat gonflé à l'hélium de 18 m; trois câbles tressés synthétiques de plusieurs centaines de mètres de longueur chacun; une charge utile avec des capteurs; et trois treuils commandés par ordinateur. Le modèle dynamique est obtenu en discrétisant le système en une série de masses ponctuelles et en estimant les caractéristiques aérodynamiques de chaque composant physique. La perturbation du modèle est définie par un modèle éolien qui tient compte de rafales turbulentes stochastiques.

Une série d'essais expérimentaux de vol a été effectuée sur une période de deux ans pour étudier la réponse du système avec et sans commande. Ceci nous a mené à un procédé de validation incrémental, les éléments passifs étant validés avant la vérification du système complet. Le modèle des câbles montre un excellent accord avec la réponse mesurée à un niveau temporel. Par contre, la validation du modèle de l'aérostat est effectueé à un niveau statistique dû au fait de l'incertitude liée à la modélisation des conditions réelles du vent.

La commande du système a été réalisée au moyen d'un asservissement de type PID (Proportional-Integral-Derivative) appliqué à l'erreur de position de la charge. Le système réduit considérablement l'écart-type des déplacements de la charge à moins de 10 cm pour nos conditions d'essai. Une comparaison du comportement prévu du modèle dynamique montre un accord favorable avec les résultats expérimentaux, indiquant que les câbles actionnés sont modélisés convenablement.

Afin d'améliorer l'algorithme de commande primaire testé sur le terrain, plusieurs stratégies de commande optimale ont été étudiées, nécessitant entre autres un modèle dynamique validé de notre système. Les contrôleurs optimaux, qui sont développés et simulés en utilisant des versions linéaires du modèle dynamique, donnent une précision approximativement deux fois meilleure que notre contrôleur antérieur. Le système de commande est amélioré davantage en utilisant un asservissement de l'entrée basé sur des mesures de forces de perturbation primaires agissant sur le système. En général, les techniques avancées de commande testées en simulations offrent des résultats encourageants qui suggèrent que le système de positionnement devrait dépasser du radiotélescope.

Acknowledgements

I am sincerely grateful for the assistance and guidance I have received from numerous sources, which have helped make my studies a pleasure instead of a chore. This was my second tour with my supervisor Meyer Nahon and I again would like to thank him for a job well done. He has a knack for supervising with a fortuitous balance of guidance and freedom, while also offering encouragement and criticism in appropriate doses.

I am fortunate to have collaborated with the fine folks at DRAO in Penticton, B.C., and I would like to personally thank Dean Chalmers, Richard Hellyer and Peter Dewdney for their tireless dedication to the LAR project. I appreciate their efforts, often starting at 3:00 AM, to collect the flight data I relied upon for my research.

During my research it often felt like I was walking around with my head in the clouds, but I am grateful that I was not alone. I would like to acknowledge those who played with balloons alongside me including Alistair Howard, Philippe Coulombe-Pontbriand, Jonathan Miller, Francois Deschenes, Gabriel Meunier, Samuel Bouchard, Alexandre Boyer, Etienne Frenette, Dr. Hamid Taghirad, Dr. Wen Bo, Dr. Benoit Boulet and Dr. Clement Gosselin. Special thanks to Dr. Gabriele Gilardi who was always willing to help.

I have only to look around my office to find several others who I would like to thank for their scholastic companionship. Thanks to Melita Hadzagic, Alessio Salerno, Shawn Arseneau, and Dany Dionne for inspiration, ideas, laughs and chocolate.

I would like to thank my McGill colleagues including Aki Sato, Aaron Saunders, Chad Abbey, Brian Wong, Philippe Cardou, James Smith, Jason Evans, Shivakumar Ranganathan, Yuwen Li, Hiba Agha, and Lianzhen Luo. Special thanks to Stéphane Caro and Mathias Legrand for all their help. I would also like to thank Jan Binder, Cynthia Davidson, Donna Morgan, and Joyce Nault for their good moods and administrative assistance.

I thank NSERC, FQRNT, McGill University, and Professor Nahon for providing financial support during my studies and the NRC and NSERC for supporting the LAR project.

Finally, I would like to thank my family members–Mom, Dad, Rachel, Russel, Bridget, Chris, Haillee, and Parker–for sending their support and friendship across this vast country.

Contents

List of Figures

List of Tables

To Bahar,

my partner in crime

Chapter 1

Introduction

1.1 Lighter-than-Air

Lighter-than-air vehicles have been used for centuries to lift people and devices into the sky. Most applications, such as the first hot-air balloon flown by the Montgolfier brothers in France in 1782, and modern helium weather balloons launched into the atmosphere, are free-flying with no intended interaction with ground. Indeed, any interaction with the ground at times other than launch and/or retrieval is usually indicative of serious problems or even catastrophic failure as occurred with the world's most famous lighter-than-air vehicle and also the world's largest ever aircraft, the Hindenburg, when it fell to the ground after its hull ruptured into flames.

Nevertheless, a class of lighter-than-air vehicles exists with permanent interaction with the ground in the form of a cable or tether. Tethered aerostats have one distinct advantage over their free-flying counterparts; they can station-keep or maintain their *general* position in the presence of a wind field without the use of locomotive or thrust forces. This creates relatively simple, quasi-stationary, high endurance aerial platforms that are attractive for many surveillance, communication and atmospheric sensing applications.

1.2 Multi-tethered Aerostat System

The precision of the tethered aerostat's station-keeping abilities can be greatly enhanced by attaching the platform to a series of tethers fixed to the ground in a spatial arrange-

ment [1] [2]. When three tethers with equidistant terminations are used, the tethers form a tripod, which upon loading from the lifting force of the aerostat, form a light-weight tension structure. Additionally, the tethers may be actuated on the ground to enhance the system's stability further and to guide the payload along a specified path [3]. In this manner, the multi-tethered aerostat system may be viewed as a large-scale cable-driven robotic manipulator. The focus of this work is the study of the dynamics behaviour and positioning capabilities of this type of tri-tethered aerostat system. The study combines comprehensive dynamics modeling, designed to assess and improve the capabilities of the system, with large-scale experimental investigations that quantify the behaviour of the system and validate the fidelity of our theoretical modeling techniques.

The specific application targeted by this research is a large-scale radio telescope termed the Large Adaptive Reflector (LAR) [4] [5], however the utility of the aerial positioning system extends to other applications involving payload manipulation and stability at relatively low altitudes (< 2 km). Moreover, the dynamics modeling techniques developed and corroborated with experimental results have broad implications for a range of mechanical systems involving cables and tethers.

1.3 Large Adaptive Reflector

To achieve a dramatic improvement in sensitivity of conventional radio telescope technologies, it is required to drastically increase the instrument's collecting area. This can be achieved by adding to the number of telescopes in an array, by expanding the area of individual reflectors or a combination of both approaches. Three of the world's largest existing radio telescopes are presented in Figure 1.1. The Very Large Array (VLA), located in New Mexico is the world's most powerful radio telescope. It is comprised of a 'Y' shaped array of 27 separate telescopes, each with a diameter of 25 m. The Arecibo telescope, located in Puerto Rico is the world's largest singe-reflector telescope with a diameter of 305 m, but because of its stationary reflector, it is always pointed toward the same location in the sky. The Greenbank telescope, located in West Virginia, is the world's largest steerable reflector

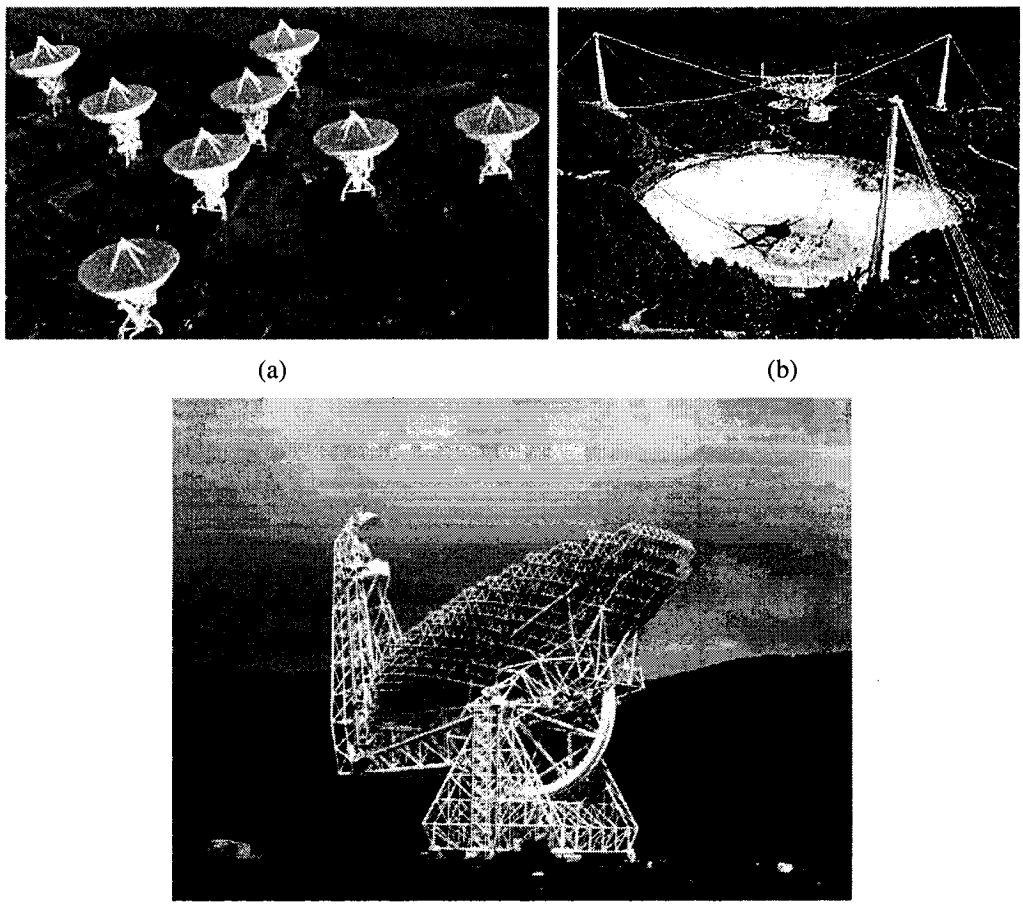

Figure 1.1: Existing large radio telescopes: a) the Very Large Array (VLA) in New Mexico, b) the Arecibo telescope in Puerto Rico, c) the Greenbank telescope in West Virginia.

with a diameter of 100 m.

A novel concept for increasing the collecting area of a single telescope while retaining the functionality of a fully steerable reflector was devised by researchers at the National Research Council of Canada's Dominion Radio Astrophysical Observatory (DRAO) [4] [5]. The proposed LAR design, depicted in Figure 1.2 [6], is based on two central components; the first is a 200-m reflector comprised of actuated panels that form an adjustable paraboloid with a focal length of 500 m, and the second is a focal package that is held in place by a multi-tethered aerostat system. The present work focuses exclusively on the dynamics behaviour of the aerostat positioning system, which uses ground-based winches to

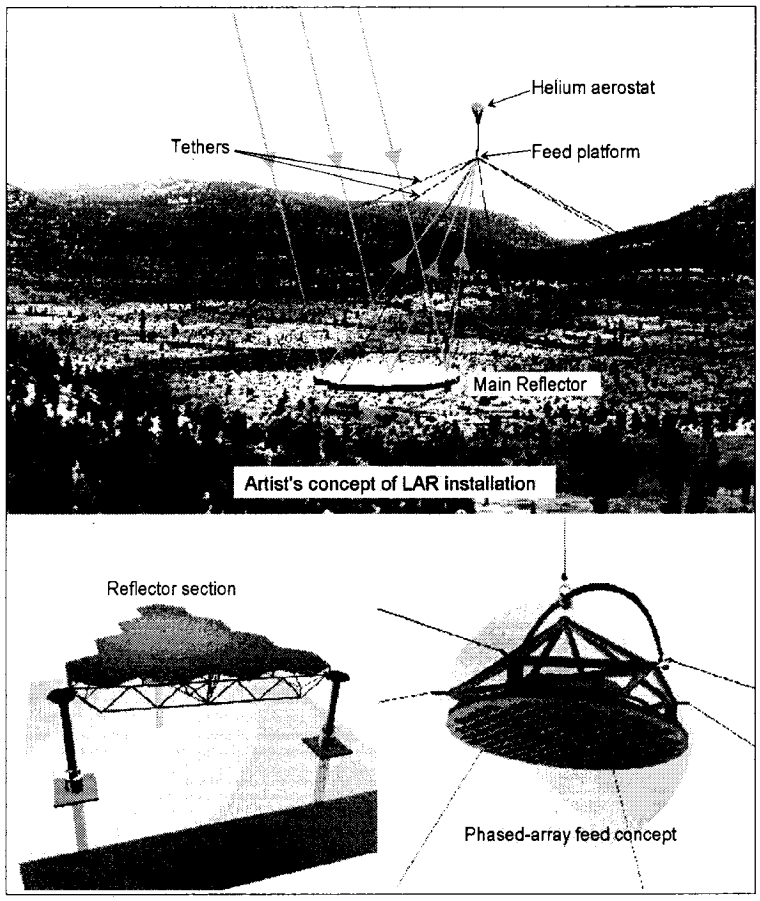

(a)

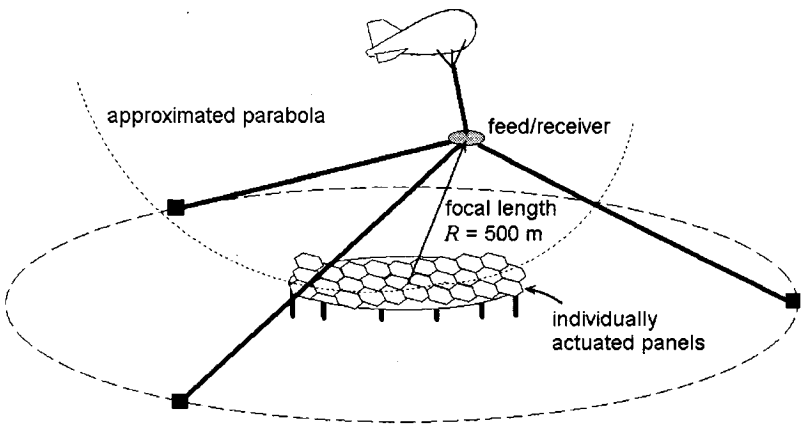

(b)

Figure 1.2: LAR radio telescope concept: a) an artist's rendition including details of a reflector panel and the receiver, b) general schematic displaying the main telescope features.

actuate the tethers to achieve the telescope's desired workspace and stability. A one-third scale testing facility was constructed at DRAO from 2001 to 2003 to study its behaviour and provide a comparison to our theoretical model. The specific details of the system examined in this study including its physical parameters, modes of operation and positioning objectives are drawn from the preliminary design work on the LAR system.

1.4 Related Research

Tethered aerostat systems have received limited attention in the literature, and most of the studies have focused on streamlined aerostats constrained by a single tether. Beyond tethered aerostats, several other mechanical systems utilize cable actuators, such as parallel cable manipulators, elevators, tethered underwater vehicles and tethered satellites. Relevant works pertaining to the modeling and control techniques used for these systems will be reviewed accordingly.

1.4.1 Tethered Aerostats

The earliest documented flights of a tethered aerostat were conducted by the French military in 1794 for the purpose of battlefield observations [7]. The first mathematical analysis of such a system was conducted in 1915 by Bairstow et al. [8], who developed equations of motion that could not be solved without the assistance of computing aids. A modern analysis of a tethered aerostat with a comprehensive cable model was performed by DeLaurier in 1972 [9]. He assessed stability by solving a partial differential equation representing a flexible and inextensible cable with end conditions imposed by the aerostat. His initial work considered only steady-state wind conditions but turbulence was later addressed in 1977 [10]. Redd et al. of NASA performed a linear stability analysis of a tethered aerostat in 1973 and corroborated their model with experiments [11]. Comprehensive aerodynamics of the aerostat were included in the model, but the tether model was not sophisticated as it was represented as a static force.

Jones and Krausman made progress with modeling of a tethered aerostat in 1982 when a

3-D nonlinear dynamics model with a lumped-mass discretized tether was established [12]. This model was expanded by Jones and DeLaurier in 1983 to include semi-empirical estimations of aerodynamic properties of the aerostat and a panel-method of hull modeling to account for unsteady winds. This model was applied to the study of a large 71-m aerostat manufactured by TCOM, while it was moored on the ground [13], and in flight [14]. In 1997, working with the U.S. Army, TCOM performed flights with a fully-instrumented 71-m aerostat to validate this nonlinear model with a lumped-mass tether [15]. The test flight was at an altitude of 2587 m and the aerostat was equipped with six GPS sensors to record its six degree-of-freedom motion, and a 3-axis wind anemometer. The model was shown to predict all six motion variables well. The accuracy of the simulation was somewhat limited by inaccuracies in the wind measurement as the sensor was located on a tail fin, well within the aerostat's boundary layer. An alternative planar aerostat model for TCOM's 71M coupled with a continuous tether was developed by Stanney and Rahn in 2005 to study the survivability of the aerostat in hurricane strength winds [16].

Others have studied tethered aeronautical systems involving vehicles other than aerostats. Etkin has addressed the dynamics and stability of a more general system involving towed bodies [17], while Zhu and Rahn studied stability of towed bodies during circular flights [18]. Williams and Trivailo extended the analysis of circularly towed aerial cables to include potential payload delivery and retrieval [19]. A tethered helicopter has also been studied by Oh et al. to investigate it as a possible shipboard landing solution during heavy seas [20].

1.4.2 Multi-Tethered Aerostats

Few actual studies exist that focus on multi-tethered aerostat systems. Early experimental investigations were performed by the U.S. Air Force in 1973 [1] and by Russian meteorologists in 1978 [21]. Both studies suggested that a tri-tethered system offers significant station-keeping improvement over a single-tethered aerostat, but the Russian findings were purely qualitative. The Air Force performed several flights with a large natural-shaped aerostat and an instrumented payload at altitudes between 400 and 700 m. Although their

tests showed almost an order of magnitude reduction in payload motion with multiple tethers, they relied on steel cables, which, because of a low strength-to weight-ratio compared to modern synthetic braided cables, limited the stiffness of the tripod tension structure. Other interesting outcomes of their testing program were the demonstrated advantage of separating the payload and the aerostat with a leash (this is an important part of the LAR system), and the observation of a transverse vortex-shedding oscillation of the aerostat. The Air Force flight tests involved large truck mounted winches, but the winches were only used during deployment and retrieval stages, not to actively control the payload.

A steady-state or static analysis of a tri-tethered aerostat system was performed at DRAO in 1996 [22] during the early stages of the LAR concept development. The first detailed dynamics study of the multi-tethered system was conducted by Nahon in 1999 [2]. He modeled the system as a series of discretized nodes or lumped-masses connected by visco-elastic elements. The model included a spherical aerostat and actuated tethers with PID feedback. A streamlined aerostat was added to the model in 2002 and slewing maneuvers were investigated [3]. Based on encouraging simulation results, it was decided to construct a one-third scale experimental system to confirm the dynamics and the overall feasibility of the concept. The design of the scaled system was based on scaling laws to maintain dynamic similarity [23] [24], and although it was at one-third scale, the aerostat measured 18 m in length. A linear stability analysis of the 18-m aerostat revealed that its stability improved with longer tether lengths [25], which was reflected in the design of the experimental system. Further modeling and simulation work on the LAR system was performed by Zhao [26]. She incorporated a static analysis to provide suitable initial conditions for the dynamics model, and she investigated the performance with the number of tethers expanded from three to six.

Recent research performed by astronomers in France involved an aerostat system consisting of six tethers in a double-tripod arrangement for a proposed optical telescope [27]. Their design is similar to the LAR concept as it entails winches to actuate the tethers so that the aerial receiver can track a path during astronomical observations. Although no quanti-

tative results were presented for the motion of the payload, the concept proved feasible as an image of a star was recorded.

1.4.3 Cable Manipulators

Starting with *Robocrane* in the early 1990s [28], a new class of parallel manipulators has emerged that employ cable actuators instead of traditional rigid members. The concept for these devices is similar to the multi-tethered aerostat, which is essentially a 3-dof parallel manipulator, but with the distinct difference that they are inverted, relying on gravity to tension the tethers instead of buoyancy. Significant research has been conducted into the kinematics, dynamics and control of cable manipulators [29] [30] [31] [32], however, the size of their workspace is generally limited to only a few meters or possibly up to tens of meters, which is more than an order of magnitude less than the LAR system. Due to the drastic difference in the length of the cables, which are the primary actuators, the modeling and experimental analysis techniques of the smaller mechanisms are not directly applicable to the much larger LAR. For instance, internal cable dynamics are typically neglected as the cables are typically treated as massless, linear actuators. In terms of experimental investigations, it is often possible to negate the scale difference of two systems if dynamic similarity can be maintained, but because of size limitations to critical components such as the cables and the aerostat's hull, it is not possible to scale down the LAR system to the size of existing cable manipulators while maintaining similarity.

Researchers in China have recently studied a cable manipulator that is at a similar scale to the LAR system [33] [34], which is also designed as a receiver positioning device for a large radio telescope. The main difference with the Chinese concept is that instead of using an aerostat for lift, its receiver is suspended from multiple cables extending radially to tall tower supports. The dynamics model of this system goes further than the other cable manipulator works, as some cable dynamics are included. A fuzzy controller was developed to control cable length and it was shown to outperform a PID controller in simulations [34]. However, the cables were modeled as a pure time delay, which is an oversimplicification

that ignores known cable oscillatory modes.

1.4.4 Variable Length Tethers

Long, variable-length cables are used in several mechanical systems, apart from cable manipulators, including elevators, towed undersea vehicles, and tethered satellites. Typically, modeling techniques for length-varying cables can be split into two different categories; those based on continuous partial differential equations of motion (used often in analyzing long linear actuators as in elevators [35] [36]) and those based on discretization strategies (used often in underwater vehicle works [37] [38] [39]). The dynamics of length-varying cables is important for tethered satellite systems as the typical two-body system is unstable during tether shortening or retrieval [40] [41]. Both continuous and discretized tether models have been used to study and address this problem.

The discretized approach is used in the current work because of its relative simplicity, versatility, and the clear physical interpretation of its mathematical representation. In addition, multiple experimental studies have confirmed that discretized models adequately characterize the important longitudinal and lateral cable dynamics [42] [43] [44].

An early discretized 2-D cable formulation was proposed by Walton and Polacheck in 1960 [45], which involved rigid rods attached by pin joints. A variable length 3-D cable model for tethered submersibles using rigid rods attached by spherical joints has been put forth by Banerjee and Do [37] along with Makarenko et al. [38]. Controllers were developed and tested in simulation during deployment or retrieval stages, however, this model only accounts for transverse tether dynamics and ignores viscous damping effects on longitudinal motion. A lumped-mass discretization technique where the point masses are connected by elastic elements [46] or visco-elastic elements [47] [48] overcomes this limitation. Kamman and Huston extended the lumped-mass model to handle deployment and retrieval operations by modifying the length and mass parameters of selected elements connecting successive point-masses [39] [49]. Although, various techniques have been developed for length-varying discretized cables, no work was found in the literature where

the theoretical models have been compared to experimental data.

1.4.5 Tether Control

Controlling cable and tethered systems has been approached by a multitude of control strategies including but not limited to PID [37] [2], optimal [50] [51], fuzzy [52] [34], feedback linearization [53], and robust [31]. Other control strategies have emerged that are pertinent for flexible systems where feedback sensors and actuators are noncollocated, which leads to instabilities if ignored. The common approach to this problem has been to supply the controller with accurate extrapolation of the state at the unsensed actuator input location. For continuous cable actuators, the extrapolation or estimation has been based on a time delay relation [54] [55].

For the LAR system, where the measurement and actuation points are at opposite ends of long tethers, modeling the tethers as a time-delay based on modal excitations of the endpoint is not adequate. However, controllers may be developed based on the discretized lumped-mass system, which inherit the wave propagation characteristics of the tethers. The resulting dynamics model will be of high-order, but with the computational prowess of modern processors, this should not be a serious obstacle.

The optimal control approach used in this work emerged in the 1960s with the advent of the state-space description of dynamical systems [56] [57]. Although this method requires full-state feedback, which is rarely attainable with cable systems, it can be combined with an optimal observer/estimator based on Kalman filtering techniques [58].

1.5 Primary Contributions

The current work extends prior dynamics modeling efforts directed at tethered aerostat systems. The coupling of multiple cables to an aerodynamic body that both supports and disturbs the system creates a unique dynamical system that has not been comprehensively studied. Previous studies were either based exclusively on theoretical models [2] [3] [26] or exclusively on experiments [1] [21] [27], and this work represents the first amalgamation of

mathematical modeling and experimental analysis. A summary of the main contributions of this thesis is as follows:

- Experimental validation of a comprehensive dynamics model of a novel multi-tethered aerostat positioning system. This is the first work to demonstrate favourable agreement between dynamics simulations and experiments for this type of system.

- The first experimental study of an aerostat positioning system controlled with ground based tethers. Accurate positioning (< 10 cm) was achieved with the system at heights up to a few hundred meters. This also represents the first large-scale experiments of a parallel cable manipulator, which is at least two orders of magnitude larger than typical manipulators.

- The closed-loop test results also serve as the first experimental validation of a lumped-mass tether model for representing long tethers with varying lengths.

- Development of optimal and feedforward control strategies that effectively capitalize on the detailed dynamics model of the system.

- Simulation-based demonstration of millimeter-level precision of the closed-loop positioning system using a high-order validated dynamics model disturbed by experimentally measured forces.

1.6 Thesis Outline

The three themes of this work on the behaviour of a multi-tethered aerostat positioning system are theoretical modeling, experimental validation, and control system development. The techniques utilized and the results obtained are presented in five chapters, which are introduced in the following sections.

1.6.1 Experimental System

The general characteristics of the LAR positioning system will be introduced first. Next, the one-third scale testing facility for the LAR positioning system, constructed at DRAO in Penticton B.C., will be presented. Most of the design details for the facility were reported previously and therefore only a general overview of the experimental system is included. The various subcomponents of the system presented are the aerostat, tethers, instrumentation system, and computer-controlled winches.

1.6.2 Dynamics Model

The foundations of the dynamics model including the aerostat aerodynamics, the lumped-mass tethers, the wind turbulence, and tether control system are introduced. Specific details of recent modifications to this previously developed model are included in the presentation. The modifications include improvements to the turbulence model to better reflect the wind conditions of our test site, and improved characterization of the tether's damping characteristics. Apart from the nonlinear dynamics model, a linearized version is also presented, obtained using numerical techniques. The linear simulation is compared to nonlinear results to assess the limitations of the linear approximation.

1.6.3 Passive Response of System

The initial testing phase involved fixed-length tethers resulting in a passive system in response to wind disturbances. Results are presented demonstrating the stiffness of the tethered system and a comparison with the theoretical simulation results is provided. This is an important stage in validation of the fully-operational closed-loop system as the models for the passive elements such as the aerostat and the tethers can be validated independent of the actuation system. The simulation is shown to satisfactorily predict the statistics of the test results, however, uncertainty in measuring the wind field limits the extent to which the model can be evaluated. A second validation approach that involves replacing the aerostat in the model by measured forces transmitted by the aerostat during a flight demonstrates

the lumped-mass tether model's ability to accurately predict the system behaviour. With the passive model validated, the simulation is used in a design study where two aerostat shapes, streamlined and spherical, are compared based on the dynamic response of the positioning system.

1.6.4 Controlled Response of System

The second and final testing phase of the multi-tethered system was with actuated tethers. The model was first corroborated using open-loop frequency response tests and secondly while operating with feedback control based on position measurements. The tests involved only a basic PID controller, but it proved effective at reducing the motion of payload. Using the measured forcing function from the test-flights as input to the dynamics model, the model is shown to predict the closed-loop response well. With the complete model validated, the simulation is used to perform a design study that attempts to improve performance by modifying the geometry of the system and the number of supports tethers used.

1.6.5 Advanced Control

Building on the validated model for the actuated system, a linear time-invariant (LTI) description of the system was obtained to form the basis of controller development to further improve the system's performance beyond that of the PID controller tested. Optimal regulators are shown to significantly enhance the station-keeping precision of the system, but exhibit high sensitivity to measurement noise. A feedforward controller is developed that uses measurements of the disturbing force to improve the response of the winches, and it is shown to benefit both optimal and PID feedback. Finally, the applicability of the optimal controllers over a range of geometric operating conditions is presented.

Chapter 2

Experimental System

2.1 General Features of the LAR

The general study of the feasibility of the LAR telescope can be divided into four separate topics which are: 1) the multi-paneled adaptive reflector, 2) the multi-tethered feed positioning system, 3) the feed electronics and instrumentation, and 4) a secondary mechanism located at the feed that reduces payload motion and adjusts the orientation of the receiver. As mentioned in the introduction, this work is only concerned with the tethered positioning system, which is shown in Figure 2.1.

The operational workspace for the LAR telescope contains all points on a hemispherical surface centered at the reflector's mid-point from a zenith angle from 0° to 60°. The positioning accuracy required is about 1.5 cm in terms of root mean square (RMS) error, however the fine precision positioning will be achieved by the secondary feed mechanism, termed the confluence point mechanism (CPM). Thus, the tethered aerostat system is responsible for limiting payload deflections to approximately 50 cm RMS while the CPM further reduces perturbations to the 1.5-cm level. The desired trajectories along the workspace during astronomical observations are typically of two types: 1) object tracking, which involves following a celestial body or region as it moves across the sky, and 2) scanning, which involves following a repeated straight-line track across the workspace (usually in North-South direction, which maps a 2-D surface after repeated Earth rotations).

The LAR telescope design pursued in this thesis is based on using three tethers, but it is

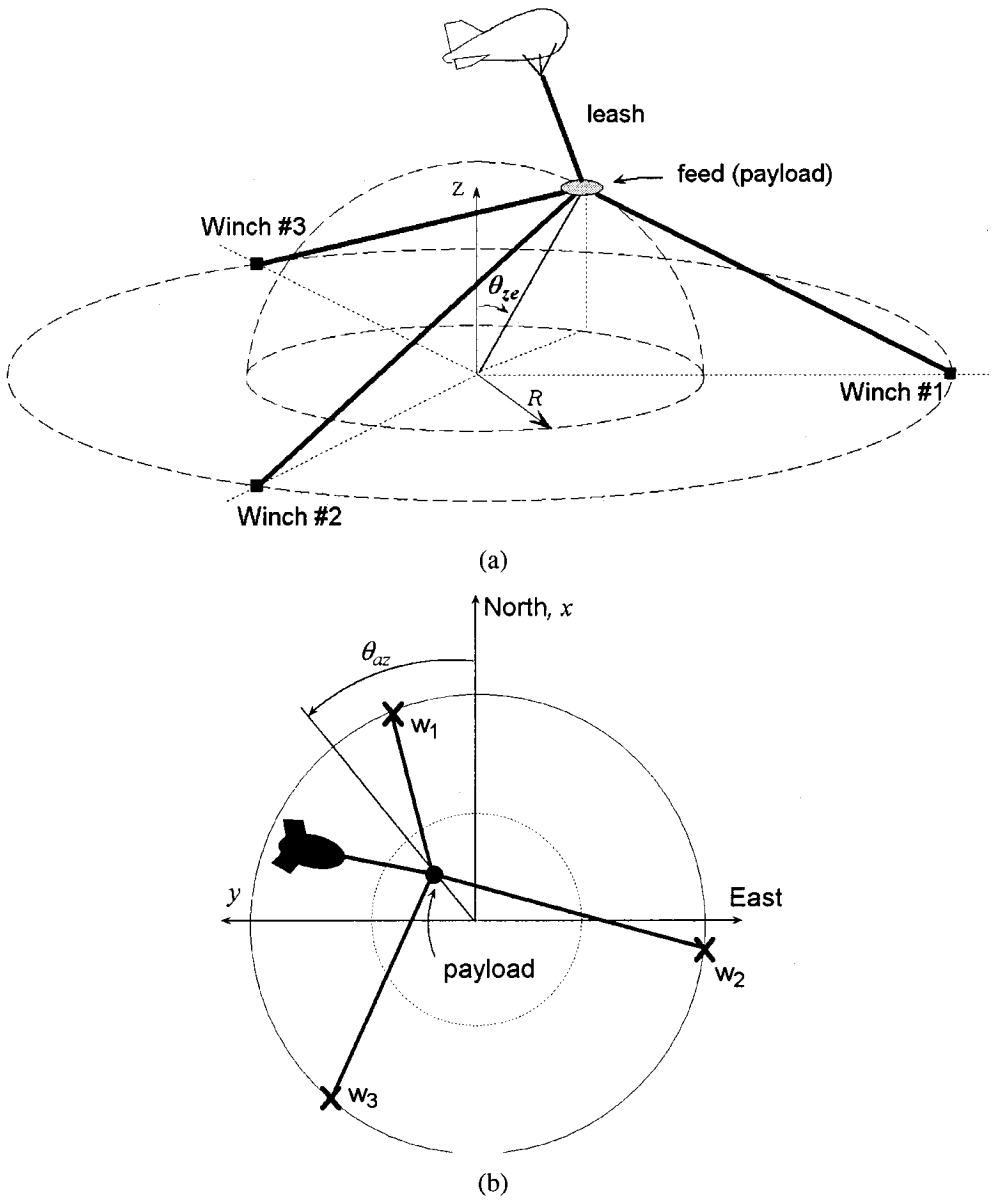

Figure 2.1: a) Layout of LAR multi-tethered positioning system: b) overhead view.

likely that six or more tethers would be used in the final design. Three tethers are adequate to cover the 2-dof workspace in terms of position, but additional tethers have the advantage of, not only stiffening the system, but also expanding the workspace in terms of including the orientation of the feed. The telescope requires that the feed point to the center of the reflector during observations, and although the CPM (in addition to precision positioning)

will be the primary actuator in terms of feed orientation, using more than three ground tethers introduces a certain level of angular controllability of the feed, which should reduce the CPM's design requirements. The motivation for studying the three-tethered tripod arrangement is based on limiting the initial scope of the analysis to a manageable level. The emphasis of this work is to validate a dynamics model of the tripod system, which is an important and arguably critical first step in expanding the model to six or more tethers and including the feed's angular equations of motion. The large size of the positioning system and the precision required create a truly unique system that, as mentioned in Chapter 1, has not been comprehensively analyzed using experimental techniques. Therefore, there is a strong need to test our dynamics model against measured data.

2.2 Scaling Factor

The two goals of the experimental system are to assess the feasibility of operating a relatively large-scale aerostat positioning system and to assess the quality of our dynamics model. For model validation to be convincing, it is essential that the experiments adequately characterize the significant features of the scrutinized system. Ideally, the scale of the test facility would be such that it fits within the confines of an indoor laboratory, but in terms of the LAR system several aspects such as tether diameter and hull thickness, impose a lower limit to the scale of an experimental system that preserves dynamic similarity. For instance, the full-scale LAR system with a focal length of 500 m involves tethers with a 18-mm diameter. To test the system at a scale of 1:50, which with a focal length of 10 m requires a rather large laboratory, the tethers necessary for similarity are only 0.36 mm in diameter. Braided tethers of the required materials do not exist below 1 mm, hence tests with strict dynamic similarity are not possible at this scale. The aerostat creates more grave problems for small-scale testing as it is impossible to reduce hull thickness by any significant factor without seriously compromising helium retention, and thus the required lift to weight ratio is not attainable at a small scale.

A scaling factor of three was chosen for our experimental facility, which was a com-

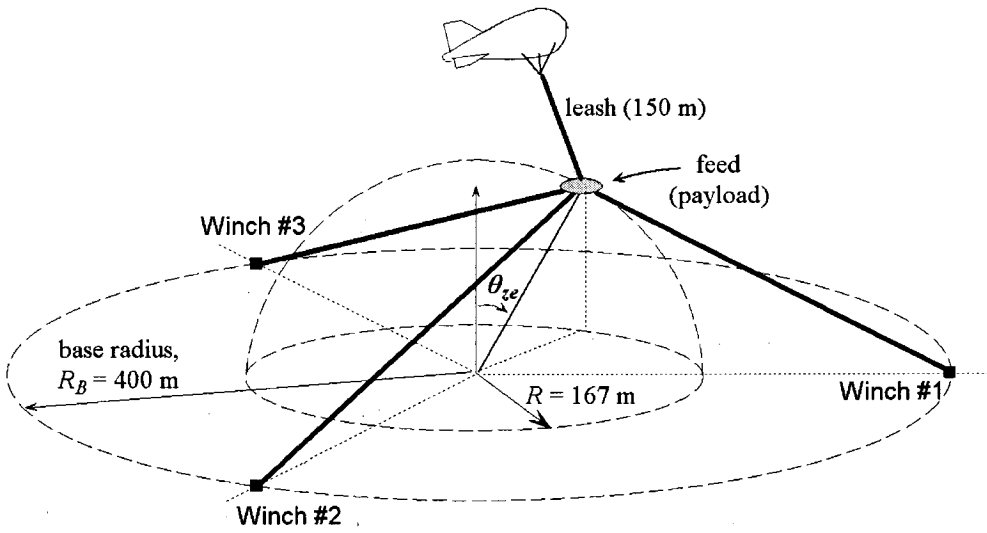

Figure 2.2: Layout of the One-Third Scale Experimental System.

promise between fiscal resources and dynamic similarity. Strict similarity for two outdoor systems at different scales is not possible as the atmospheric parameters are fixed and constant for both the test and the original system [23]. Although dynamic similarity is not retained in the strictest sense, at one-third scale the important dynamics modes should all be present.

The dimensions of the one-third scale system are given in Figure 2.2. The focal length is $R = 167$ m and the winches are placed on a circle with radius, $R_B = 400$ m. The test facility, constructed from 2001 to 2003, is located at the existing radio observatory, DRAO, south of Penticton, B.C. This is an ideal site as there is access to a sufficient open space that is relatively flat. Figure 2.3 shows the test site, which is also sheltered by surrounding foothills, resulting in wind conditions that are mild compared to nearby urban regions. Details of the main components of the system including the aerostat, tethers, instrumentation, winches, and the overall control system are presented in the following sections. The design approach for the test facility was to obtain off-the-shelf parts whenever possible (aerostat, tethers, winch motors, sensors) while designing and fabricating the necessary subcomponents (winch frame, instrument platform, data acquisition software).

Figure 2.3: Outdoor test site at DRAO south of Penticton, B.C.

2.3 Aerostat

Three types of aerostats were considered for the experimental system, streamlined, spherical, and variable-lift or kite-like aerostats, whose buoyant lift is supplemented with wind-induced lift [25]. A streamlined aerostat was chosen based on its proven reliability and smaller drag forces in response to wind perturbations. A subsequent comparison of a spherical and streamlined aerostat using simulation results is performed in Section 4.3. The size of the aerostat was determined by the amount of lift required, which is calculated as the minimum lift required to ensure that none of the three tethers becomes slack throughout the workspace.

The aerostat was manufactured by World Wide Aeros of Los Angeles, California and its shape and features were based on their previous aerostats. Upon delivery, the aerostat became affectionately known as BOB, which is an acronym for big orange balloon. BOB's length is 18 m and its other physical parameters are summarized in Table 2.1. Figure 2.4 shows three photos of BOB along with its launch trailer and hangar. The trailer is equipped

(a)

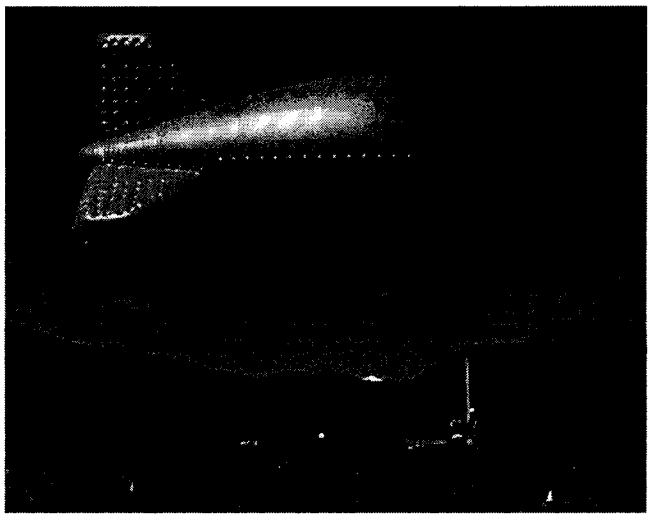

(b)

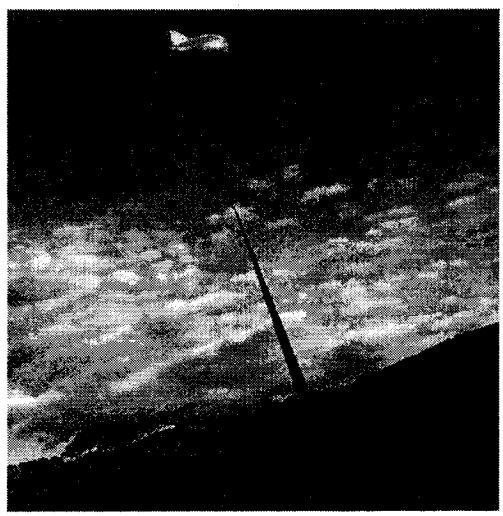

(c)

Figure 2.4: The aerostat BOB: a) during move from hangar to launch site, b) in profile during early launching stage, c) in flight looking up a support tether.

with one large and five small electronic winches. The large winch is used to reel-in and pay-out the aerostat's main tether line while the five smaller winches are used for 50-m handling lines that are suspended from the aerostat. The main bed of the trailer can rotate about a vertical axle to ensure that the aerostat is not exposed to excessive cross-winds while it is anchored to the trailer.

Both the hull and the three tail fins are inflated with helium and the helium pressure is regulated by an internal air bladder, known as a ballonet. The ballonet is attached to a small plate on the underside of the aerostat where two blowers regulate the pressure inside

Diameter	7.7 m
Length	18 m
Volume	530 m^3
Mass	270 kg
Ballonet volume	44 m^3
Fineness ratio	2.4
Max. net lift	2500 N
Tail fins	Inverted Y

Table 2.1: Summary of BOB's characteristics.

the balloon by either taking-in or venting air. For high altitude aerostats, a fully-inflated ballonet may account for as much as 30 to 40% of the total aerostat volume. In contrast, our ballonet volume is only 8% of the aerostat (44 m^3 of 530 m^3), but it is sufficient for low altitude flights (< 1000 m) where pressure fluctuations are not dramatic.

2.4 Tethers

Although the thin support tethers are not visible with the naked eye when viewed from opposing sides of the test facility, they are critical in achieving the LAR's demands for precision positioning. In the absence of recent advances in synthetic tether technology, the multi-tethered aerostat system would lack the stiffness and responsiveness required for the LAR telescope. The most important property for the tether material is its strength-to-weight ratio. The tether's dead weight is not the serious issue as the amount of lift required to raise the tethers off the ground is minor compared to the amount of lift required to reduce the inevitable catenary sag due to gravitational loading. The elevation angle for the support tethers is about 23° and any tether sag significantly reduces the stiffness of the system.

Table 2.2 presents the properties of several potential tether materials that were considered [6] [59]. It should be noted that the properties listed are for a braided tether and thus differ from the constituent material properties. It is clear that Plasma is the best option for the LAR system as it has the highest strength-to-weight ratio and also the highest modulus of elasticity apart from steel. Plasma is the trade name for a ultra-high density polyethylene

Tether material	Density ρ_t (kg/m^3)	Ultimate stress S_b (GPa)	Young's Mod. E (GPa)	Strength-to-weight S_b/ρ_t ($\times 10^5$ m^2/s^2)
Kevlar 49	1000	0.86	11	8.6
Spectra	840	0.98	17	12
Plasma	840	1.26	38	15
Vectran	1050	1.09	28	10
Steel	4400	0.71	80	1.6

Table 2.2: Properties of various tether materials.

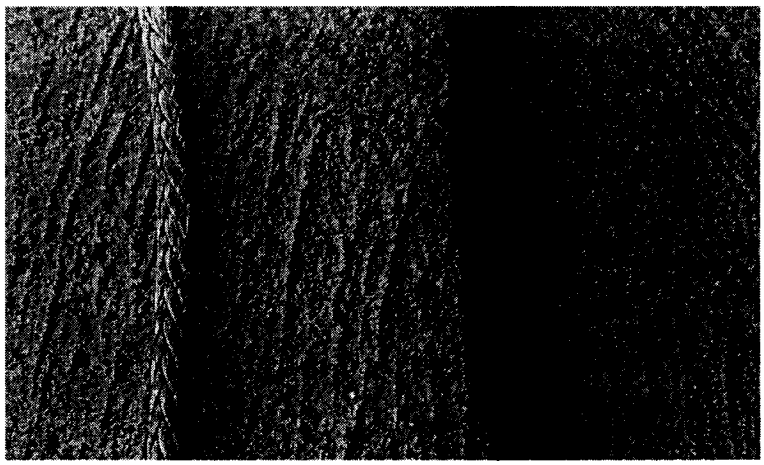

Figure 2.5: 5-mm diameter Plasma tether next to 12-mm aerostat leash which has interior conductors and a protective sheath.

based tether manufactured by Cortland Cable, NY. The tether is composed of 12 strands of Honeywell Spectra fiber that has been recrystallized and braided for high strength.

The diameter of the tether was determined by estimating tether loads during extreme wind conditions for the region. Designed to maintain a safety factor of five (as suggested by Cortland Cable), it was found that a 6-mm diameter tether with a break strength of 35.6 kN is sufficient. The initial tests (Chapter 4) were performed with 6-mm tethers, but in attempt to reduce weight, they were replaced by 5-mm tethers during the closed-loop tests (Chapter 5). Consequently, the system no longer had a safety factor of five, but the testing regimen included strict monitoring of weather conditions to ensure that test flights were only performed when mild weather was forecast.

A second type of tether is also required for the aerostat's main line, which has a lower part and an upper part. The lower part runs from the trailer winch to the confluence point. It is used during launch and retrieval, but during flights its tension is taken up by the three support tethers and it becomes slack, and therefore only minimally intrusive on the behaviour of the system. The upper portion, referred to as the aerostat leash, extends from the confluence point to the aerostat. The main difference with this type of tether is that it is not simply a strength member, but instead consists of electrical conductors and an outer protective cover. The strength member is a 6-mm core of Spectra tether, but the total diameter of the line is 12 mm. A photograph showing both the 5-mm support tethers and the the 12-mm leash is shown in Figure 2.5.

2.5 Instrumentation

In order to monitor environmental conditions and the performance of the system, an instrument platform was incorporated into the system at the confluence point of the tripod/aerostat system, since this is where the telescope's payload is located. The instrument platform is a thin circular plate 0.8 m in diameter that houses an array of sensors and instrumentation as shown in Figure 2.6. It was designed to hang freely on the tethers using Teflon hanger fittings. This non-rigid method of securing the instrument platform to the tethers at the confluence point is intended to maintain the platform's horizontal attitude while it rests on the tethers. The complement of sensors on the instrument platform and their functions are summarized as follows:

- 4 load cells–used to measure the tension in the three tethers and the leash,
- ultrasonic 2-axis anemometer–measures horizontal wind speed and direction,
- differential GPS–antenna and receiver used to measure the position of the platform; a similar fixed unit on the ground completes the differential system,
- 2-axis tilt sensor–used to measure the pitch and roll of the platform,

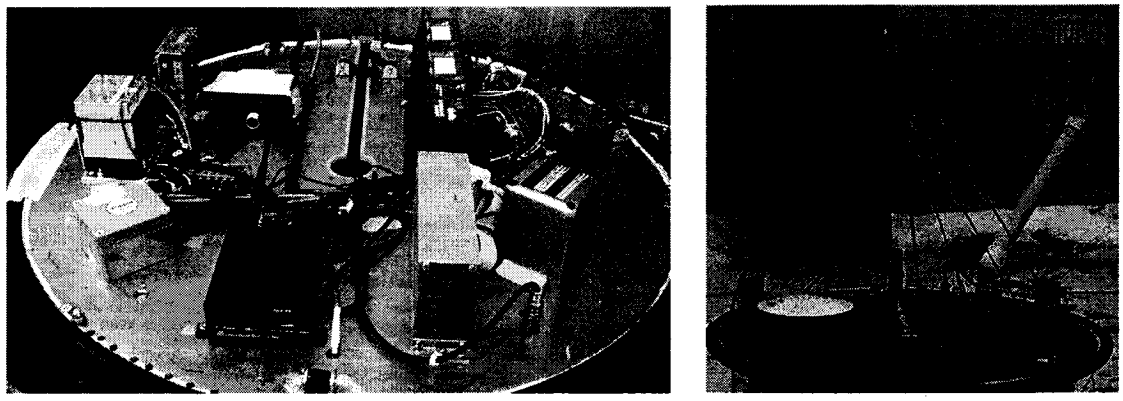

(a) (b)

Figure 2.6: The instrument platform a) under-side with array of sensors and A/D modules b) top-side with ultrasonic wind sensor and GPS receiver.

- digital compass–to measure the heading or yaw of the platform,
- inertial measurement unit–comprised of three accelerometers and three rate gyros to provide auxiliary motion data
- temperature probe–to measure ambient air temperature.

The aerostat also was equipped with a host of sensors mounted to its under-side ballonet plate, which are summarized as follows:

- internal pressure and temperature sensors–to monitor the conditions inside the aerostat's envelope,
- differential GPS–antenna and receiver used to measure the position of the aerostat,
- the same tilt sensor and digital compass as the platform–to measure roll pitch and yaw of the aerostat.

Both airborne GPS sensors transmit their measurements to the ground via radio modems, while all the the other sensors transmit through a single transmission line. Analog to digital conversions are performed prior to transmission by onboard National Instrument's Field-Point I/O modules. Table 2.3 presents the specific manufacturers and models of the main sensors.

Sensor	Manufacturer	Model
Load cell	Mass Load Technologies	ML200
Anemometer	Gill Instruments	Windsonic
GPS receiver	Novatel	FlexPak-G2L with RT-2 functionality
GPS antennas	Novatel	GPS-702 (airborne), GPS-503 (base)
tilt sensor	Cross-bow	CXTA02
Compass	KVH Industries	C-100
IMU	BEI Systron Donner	MotianPak

Table 2.3: Summary of instrumentation.

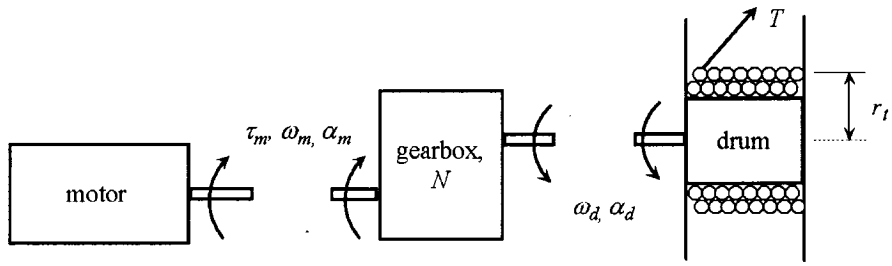

Figure 2.7: Mechanical components of winch system.

2.6 Winches

The ground winches were designed based on specifications estimated from prior simulation results [23]. The mechanical winch system shown schematically in Figure 2.7 consists of three coupled components, which are a servomotor, gearing, and the winch drum. The maximum tether tension, T_{max}, speed, $\dot{u}_{max}$ and acceleration $\ddot{u}_{max}$, provided by simulations were used to estimate the required motor torque τ_m, speed ω_m and acceleration α_m, using the following relationships:

$$\tau_m = \frac{T_{\max} r_t}{N}, \quad \omega_m = \frac{N\dot{u}_{\max}}{r_t}, \quad \alpha_m = \frac{N\ddot{u}_{\max}}{r_t} \tag{2.1}$$

where N is the gear ratio and r_t is the tension radius on the drum. It is clear that the motor requirements depend on the gear ratio and the size of the winch drum (diameter and width). Specifically, the required torque, τ_m is directly proportional to the radial location of the tether, r_t, while the speed ω_m and acceleration α_m are both inversely proportional

	Torque (Nm)	Speed (rpm)	Acceleration (rad/s^2)
Required	11.05	1274	3502
Bosch MHD090	12	2500	3800

Table 2.4: Motor requirements and manufacturer's specifications.

	Gear Ratio	Output torque (Nm)
Required	100	1105
Alpha SP210	100	1000 cont. 1520 peak

Table 2.5: Gearing requirements and manufacturer's specifications.

to r_t. Numerous combinations of drum sizes and gear ratios were investigated in order to match the required motor torque, speed and acceleration to available motors. A high gear ratio, N is required since the available motor output is typically high speed and low torque.

A review of numerous motor manufacturers produced several off-the-shelf servosystems that could meet the requirements. The specific requirements for the motor and gear box are given in Table 2.4 [60] and 2.5 [61] respectively along with the chosen components. It is observed that the gear output torque exceeds the manufacturer's rating for a continuous load by 10%, however this is not anticipated to be a problem since the peak tether load and velocity were used to determine the continuous winch requirements.

With the selection of the motor and gearbox complete, the detailed design of the winch frame and the communication system was performed. Figure 2.8(a) shows the winch drum housed in its frame with the gear box and Figure 2.8(b) shows a winch in the field. The main feature of the winch frame is the ability of the drum and drive system to rotate about a vertical axis. This is an essential feature of the winch for accommodating the various tether angles that lie within the operating range of the positioning system. A level-wind was added to the winch near the drum to ensure that the tether wraps are even and uniform, and a fair-lead arm was added to extend the moment arm for vertical axis rotation.

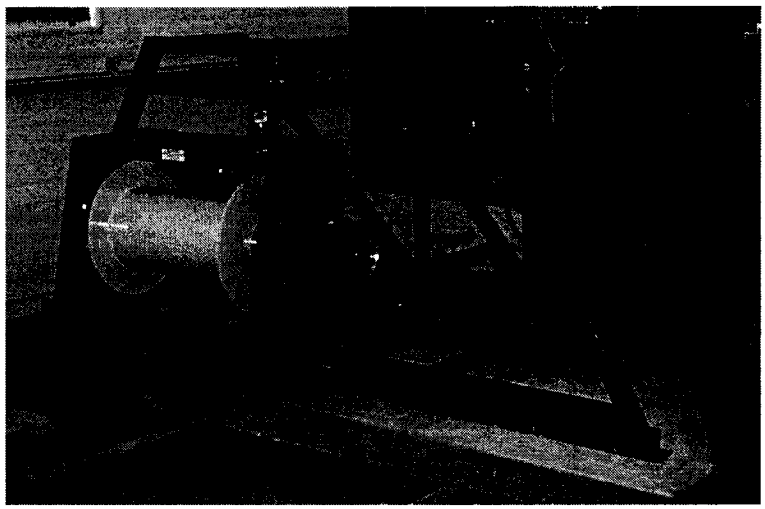

(a)

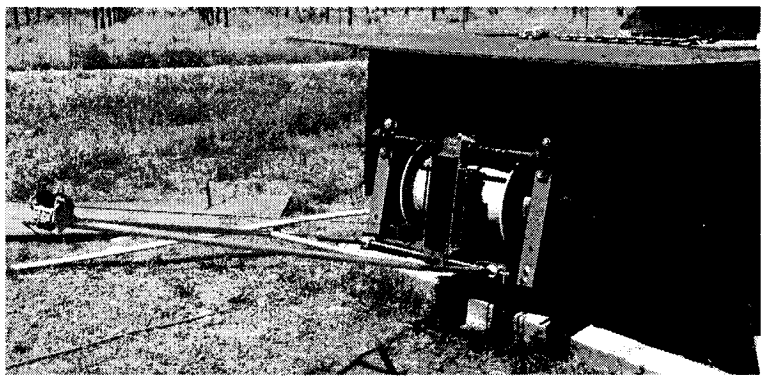

(b)

Figure 2.8: Winch a) frame during assembly b) installed in the field with level-wind and fair-lead accessories.

2.7 Control System

The winch control system involves the integration of all the system's components, as feedback control based on GPS position measurements are used to adjust tether length in response to wind disturbances. A schematic of the PC-based control architecture is shown in Figure 2.9.

Three PCs are used to retrieve and record measurements and transmit control commands. The basic operation of the control system is summarized as follows:

- PC #1 collects, displays and records data using Labview. The ground or base GPS

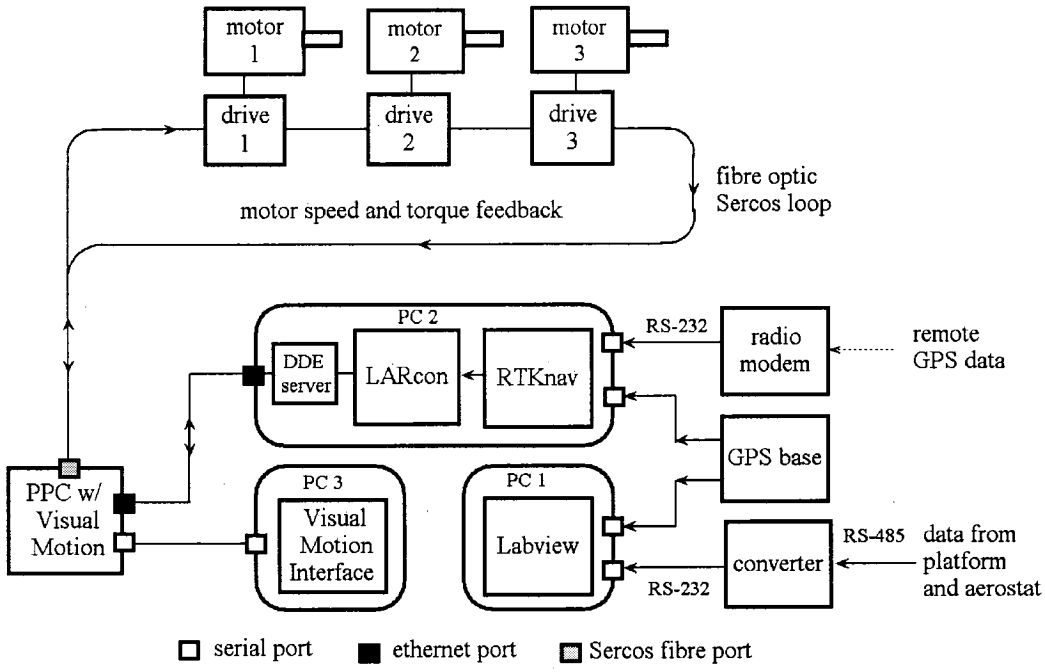

Figure 2.9: Architecture for PC-based measurement and motor control system.

signal is used to time-stamp or synchronize the measurements.

- PC #2 collects data from both the platform and aerostat GPS units via a wireless radio link and produces real-time position measurements using commercial RTKnav software developed by Waypoint Consulting of Calgary, AB. The platform position in Cartesian coordinates is passed to the feedback control software, LARCon at 10 Hz, which computes winch commands. The winch commands are passed to the Bosch Rexroth PPC motor controller hardware using the Windows dynamic data exchange (DDE) server.

- PC #3 runs Bosch's commercial Visual Motion software interface which lets the user specify functional parameters and monitor the operation of the motors. Visual Motion communicates directly through a serial link to the PPC.

- The PPC receives parameters from PC #3 and 10-Hz commands from PC #2, but it has its own internal motor control loop that operates with encoder feedback at

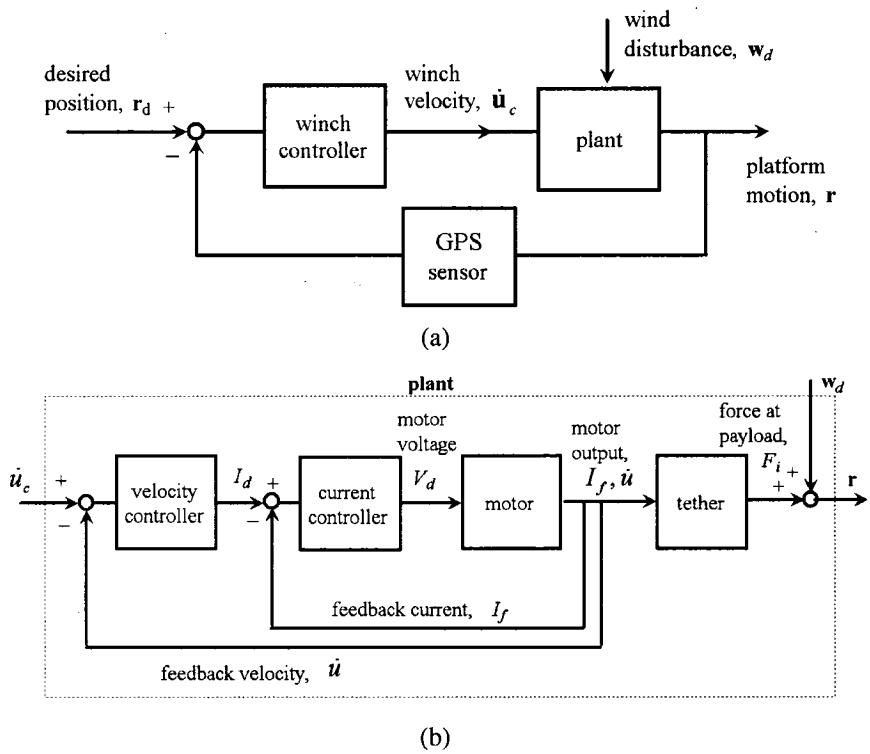

Figure 2.10: a) Block diagram of overall control system with 10-Hz position feedback b) system plant with 500-Hz internal motor current and velocity feedback.

500 Hz. The motors are connected in series by a fiber optic SERCOS loop (which is over 1 km in length). The individual control signals received at each winch are amplified to the desired voltage by the motor's drive or amplifier.

Block diagrams of the 10-Hz overall control system and the 500-Hz internal motor control system are given in Figure 2.10

2.8 Testing Program

2.8.1 Flights Summary

Test flights commenced at DRAO in April 2002 and by the end of 2005, over 30 flights had been performed. For the first few flights, BOB was launched and flown on a single tether to test its functionality and provide training to the operations personnel. The first

multi-tethered aerostat flights occurred in October 2002 with the tethers anchored to the ground. There were many lessons learned during the first testing phase as launch/retrieval procedures were refined and instrumentation was upgraded.

The first flight with the updated and complete sensor package occurred in March 2004. Several flights were conducted with constant tether lengths to be used to validate the uncontrolled simulation results. It was a full year later in March 2005 that operational winches were added to the system and closed-loop results were obtained. The tests performed with the winches used PID feedback to regulate about a fixed location within the workspace, not tracking trajectories along the workspace. By the end of 2005, the operational life of BOB expired and the LAR testing program at DRAO was suspended.

2.8.2 Flight Procedures

The typical duration of a test flight was three to four hours, and most took place in the early morning hours to take advantage of calm winds during launch. Occasionally, flights lasted into the afternoon when winds typically increased. Extreme weather was not encountered during any of the flights, nor did any tests extend overnight.

Prior to a flight, BOB is driven from its hangar while fastened firmly to the trailer bed. Once it arrives at the desired launch site, the trailer is connected to electrical power, which is transmitted through the main winch, central tether and leash to the aerostat. During the initial launch phase, the trailer bed is unlocked and allowed to rotate with the aerostat into the oncoming wind. All six trailer winches pay-out slowly until the handling lines are free of their winches and the aerostat is only attached to the leash, which is unwinding on the main winch. When the aerostat reaches a height of 160 m, the leash is fully payed-out and its terminal emerges from the main winch drum. The lower end of the leash is attached to a small circular ring (approx. 10 cm), which acts as the confluence point for the multi-tethered system. The three support tethers are then attached to the ring and the instrument platform is suspended by a wire from the ring with the tethers passing through its hanger fittings. When the support tethers become taut, the suspension wire becomes slack and the

platform rests horizontally on the tethers.

The central tether, which is composed of the same material/conductors as the leash, is attached to the bottom of the confluence ring. Its conductors are plugged into the platform and a second power connection is made from the platform to the leash completing the circuit with the platform and the aerostat's instrument loads in series. With the power connected and the platform in place, the central tether is let out slowly until the full load is transfered to the three support tethers. The central tether then becomes slack and based on its slender profile and relatively low mass ($\approx$ 20 kg), it is expected to have a minor impact on the system's overall dynamics.

To achieve different geometrical configurations within the workspace, two different methods were used. Prior to testing with functional winches, the tether lengths were specified and measured before the flight to ensure the desired workspace location. With operational winches, the tether lengths need not be adjusted beforehand, and different locations were achieved by manually jogging the winches or using the closed-loop control. It is reiterated that this type of feedback control was simply fixed-point tracking for the purposes of regulating the system about one specific location.

Chapter 3

Dynamics Model

A mathematical model is typically the least resource-intensive method to study the dynamics behaviour of a mechanical system. Therefore, to evaluate the positioning capabilities of the multi-tethered aerostat system, a dynamics model was developed following the conceptual stage of the LAR study. During any modeling process, assumptions must be made as to what are the dominant aspects of the real system and what aspects can be neglected. For the multi-tethered aerostat system the most influential aspects of the system in terms of dynamics were deemed to be the aerostat, the tethers and the wind disturbance; as a result the majority of the modeling effort was directed toward obtaining convincing models for these components of the model.

3.1 Model Overview

The dynamics model for the multi-tethered aerostat system evolved from dynamics models developed by Nahon for underwater vehicles [62] and by Buckham and Nahon for long marine cables [63]. Nahon combined the basic vehicular aerodynamics model with multiple lumped-mass tethers, a winch controller and a wind input that includes turbulence [2].

The location and layout of the relevant reference frames, including the inertial frame (X_I Y_I Z_I), the aerostat's body frame (X_A Y_A Z_A) and an elemental frame for one of the discretized tether elements(p_1 p_2 q) are presented in Figure 3.1. The inertial frame is fixed to the center of the LAR's imaginary telescope reflector, which is located at the center

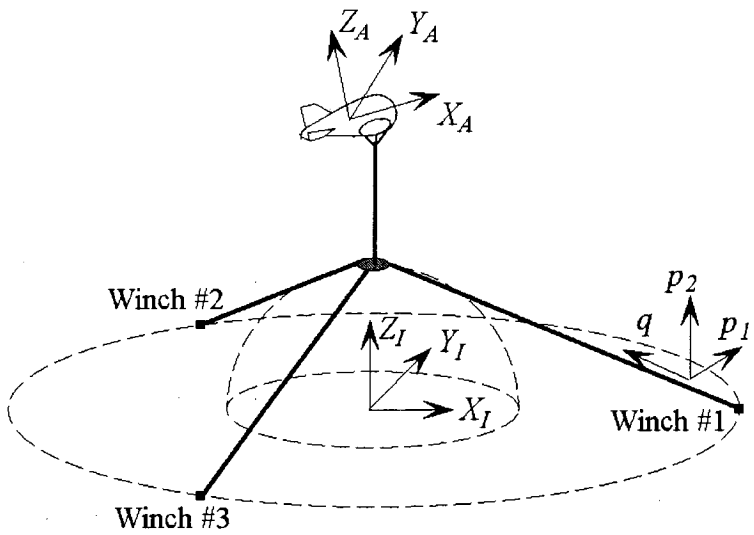

Figure 3.1: Reference frames for dynamics model.

of the winch circle. The X_I axis is aligned with North, Y_I is aligned with West, and Z_I points upward. The aerostat's body frame is attached to its center of mass, with the X_A axis pointing forward, its Y_A axis out the port side and Z_A pointing upward. The individual body-frame for each discretized tether element is located at the center of the element, with p_1 and p_2 directed in the local normal and binormal directions, and q is the local tangent to the tether.

The complete dynamics model of the system consists of the following elements: 1) a discretized cable model for the three support tethers and the aerostat leash; 2) the feed or receiver; 3) the aerostat and 4) the wind input. The general characteristics of each aspect of the dynamics model are presented next.

3.2 Tether Model

In reality tethers are a continuous or distributed parameter system whose dynamic behaviour, described by a second-order partial differential equation, is not readily solvable when subjected to a general external force. To simplify the analysis, the tethers are modeled using a lumped-mass discretization approach, which leads to a series of motion equa-

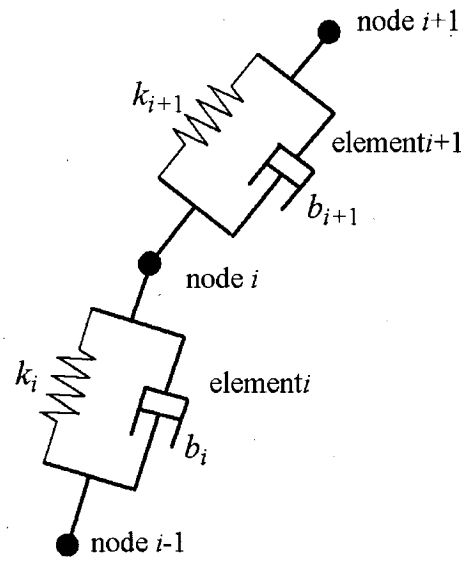

Figure 3.2: Lumped-mass visco-elastic tether model.

tions that are solvable using standard numerical integration techniques. The reliability of lumped-mass cable models for predicting the dynamics behaviour of long cables has been previously established through experimental validation with marine systems [47] [63] [44].

The lumped-mass discretization approach involves a series of point masses or nodes which are connected by massless visco-elastic elements as shown in Figure 3.2. Each element has its mass equally distributed to its two connected nodes. The forces generated by each element and that are applied to its two end nodes can be split into external forces, including aerodynamic and gravity components, and internal forces, which include elastic and damping components.

The aerodynamic forces on the i-th element are characterized by a drag force that has two normal components, $\mathbf{D}_{p1}$ and $\mathbf{D}_{p2}$ and one tangential $\mathbf{D}_q$ component given by:

$$
\begin{aligned}
D^i_{p1} &= -(\frac{1}{2}\rho C_d d_t l^i_u) f_p \left|\mathbf{v}^i\right|^2 \frac{v^i_{p1}}{\sqrt{(v^i_{p1})^2 + (v^i_{p2})^2}} \\
D^i_{p2} &= -(\frac{1}{2}\rho C_d d_t l^i_u) f_p \left|\mathbf{v}^i\right|^2 \frac{v^i_{p2}}{\sqrt{(v^i_{p1})^2 + (v^i_{p2})^2}} \\
D^i_q &= -(\frac{1}{2}\rho C_d d_t l^i_u) f_q \left|\mathbf{v}^i\right|^2
\end{aligned}
\tag{3.1}
$$

where ρ is the local density of air, d_t is the tether diameter, C_d is the normal drag coefficient of the cable, l_u^i is the unstretched length of the i-th element, and $\mathbf{v}^i$ is the velocity of the geometric center of the i-th cable element with respect to the surrounding air, with components v_{p1}^i, v_{p2}^i, and v_q^i. The elemental velocity, $\mathbf{v}^i$, is found by averaging the relative velocities of its two end-nodes. In each equation of eq.(3.1), the drag coefficient is modified by a loading function, f_p or f_q, which account for the nonlinear breakup of drag between the normal and tangential directions. The loading functions are dependent on the relative angle, η, between the i-th element and the incident fluid flow. The nonlinear loading functions, synthesized by Driscoll and Nahon by modifying relations presented by several sources on towed marine cables [47], are as follows:

$$\begin{aligned} f_p &= 0.5 - 0.1\cos\eta + 0.1\sin\eta - 0.4\cos 2\eta - 0.011\sin 2\eta \\ f_q &= 0.01(2.008 - 0.3858\eta + 1.9159\eta^2 - 4.1615\eta^3 + 3.5064\eta^4 - 1.1873\eta^5) \end{aligned} \tag{3.2}$$

where η is expressed in radians and $0 \leq \eta \leq \pi/2$.

The gravitational force acting on the i-th element, W^i, in the inertial frame is given by the following equation:

$$W^i = \rho_t \frac{\pi d_c^2}{4} l_u^i g \tag{3.3}$$

where ρ_t is the density of the tether material.

The internal elastic and damping forces of the i-th cable element are calculated based on the following linear relationship with the strain, ε and strain rate $\dot{\varepsilon}$ of each element:

$$T^i = AE\varepsilon + bl_u^i\dot{\varepsilon} \tag{3.4}$$

where the strain is defined as:

$$\varepsilon = \frac{l^i - l_u^i}{l_u^i} \tag{3.5}$$

and l^i is the stretched length of the i-th element, A is its cross-sectional area, E is Young's modulus and b is the viscous damping coefficient of the tether. The stiffness of each tether element, k_i, is related to Young's modulus, E, by:

$$k_i = \frac{EA}{l_u^i} \tag{3.6}$$

The manufacturer's published value of $E = 38$ GPa for Plasma as presented in Table 2.2 was confirmed by observations of vibration tests conducted with a vertically suspended weight [24] [64].

3.2.1 Tether Damping Coefficient

In general, damping forces in cable systems tend to be much smaller than the elastic forces, and for this reason, in many cable dynamics studies, damping is neglected altogether. Through simulations of the closed-loop LAR system, it has been observed that tether damping does play an important role when considering high frequency motions and during aggressive control inputs. Specifically, the closed-loop system tended to experience instabilities if little or no damping was included.

The precise damping characteristics of the tethers are difficult to model accurately due to the complexity of the energy dissipation mechanism. The first challenge is to find a suitable damping model, and then to estimate the damping parameters. The damping behaviour of a braided tether is due to internal friction, but precise models of the damping mechanism depend on the structure of the composite strands. For example, Huang and Vinogradov have developed a detailed nonlinear damping model for cables which exhibits hysteresis and corresponds well to experimental data [65]. In the interest of retaining a relatively simple tether model, the internal damping forces were assumed to be proportional to velocity as in the common viscous damping model. Vibration tests of a vertical tether have demonstrated that the damping behaviour can be estimated adequately with viscous damping [24].

Estimates for the tether's damping coefficient b were also obtained from the vertical vibration test. The damping ratio, ζ is first estimated based on the logarithmic decrement of peak tensions, and next the damping coefficient is calculated based on the following relationship:

$$b = 2\zeta m\omega_n \tag{3.7}$$

where m is the payload mass and ω_n is the natural frequency of the system. The initial

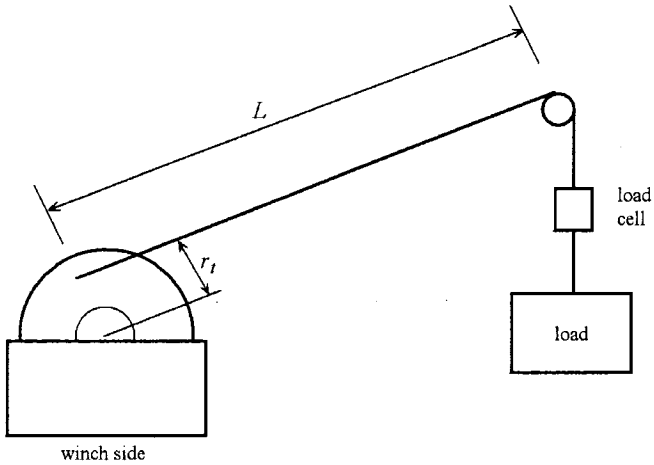

Figure 3.3: Experimental set-up for damping estimation.

experiment was performed at the University of Victoria in 2001, and it involved tethers varying in length between 1.4 and 2.1 m [24]. Longer cables resulted in lower damping coefficients; however, the dimensionless damping ratio appeared to be constant at approximately $\zeta = 0.017$. Similar vertical suspension tests were performed in 2004 at McGill University to study a larger range of tether lengths, from 2 m to 25 m [66]. The results indicated that the damping ratio was not constant with tether length as it varied from $\zeta = 0.034$ at 1.85 m to $\zeta = 0.015$ at 25 m. Alternatively, the damping coefficient multiplied by the tether length, $bL \approx 2200$ Ns was found to be relatively constant over the tether lengths tested. This shows that the damping coefficient has the same length variability relationship as the stiffness k since $kL = EA$, which is constant for a uniform cable. This explains why the damping ratio, despite its nondimensionality, varies with length as it is a ratio between the actual damping, which is inversely proportional to length, to the critical damping $b_c = 2m\omega_n$, which is inversely proportional to the square root of the length.

The total damping characteristics of the tethers of the LAR system will differ from those of the vertical tether tested because there are other dissipative sources besides internal axial friction. Because the tethers have an elevation angle of about 25°, they are more horizontal than vertical. This causes the tether to experience sag, thus altering its vibrational response to include not only axial motion but certain transverse motion as well. Any

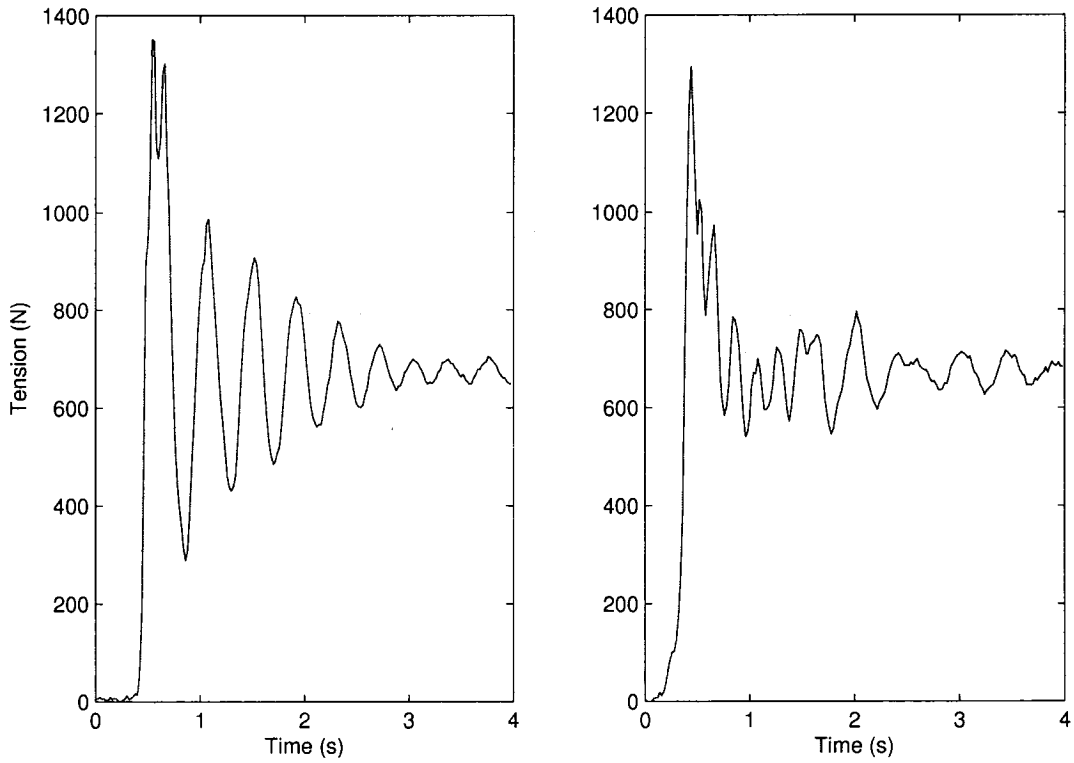

Figure 3.4: Comparison of oscillatory damping tests for tether lengths of 9 m on the left and 19 m on the right.

bending experienced by the tether during transverse motion results in frictional energy dissipation that is not reflected in the axial damping characteristics tested in the vertical configuration. Another source of energy dissipation in the real system are the physical components introduced at both ends of the tether. At the bottom end of the tether, the winch itself may introduce damping into the system and at the upper-end there are several connective housings and an in-line load cell that inevitably introduce friction to the system.

In attempt to quantify the magnitude of additional cable damping for the LAR experimental system, simple vibratory tests were performed on tethers connected to a winch as shown in Figure 3.3. A truck with an extendable hydraulic boom was used to hold the pulley approximately 8 m off the ground and a 60-kg weight was used for the load. The impulse response of the tether tension was measured by the load cell for two tether lengths, 9 m and 19 m, and results are presented in Figure 3.4. A third length of 41 m was also tested

and the results were similar to those at 19 m. The results from the 9-m test show a typical logarithmic decrement, whereas the 19-m test has more erratic behaviour and higher damping. The damping ratio estimated from the logarithmic decrement of the 9-m case is $\zeta = 0.08$, which is significantly higher than $\zeta = 0.02$ found for similar tether lengths during the vertical tests. However, it is unknown how much of this additional damping is contributed by the pulley and the extendable boom. Therefore the results from this series of test were not comprehensive or conclusive enough to produce a reliable estimate for the product of damping coefficient and tether length, bl.

To arrive at a suitable bl coefficient, the actual LAR experimental results were used in conjunction with simulation results. It was found that a fairly large range of damping produced similar results when comparing time histories of the payload motion, since damping tends to mainly affect high frequency motion that has a small amplitude. However when closed-loop results were considered, the range of suitable damping decreased as low damping coefficients produced instability in the simulation, as certain modes were excited leading to oscillatory motion with increasing amplitude. Similar instabilities were also observed in the experimental system when the control gains were set too high (see Section 5.2.2), and by matching the conditions in the simulation at which the onset of instability occurred, a suitable damping estimate was made for the tethers of $bl = 20000$ Ns, a value much larger than $bl = 2200$ Ns found for a vertical tether.

3.3 Aerostat Model

The aerostat was modeled as a rigid body using a component breakdown approach, where the aerodynamics forces on the hull, tail fins and flying harness are determined separately and combined to estimate the dynamic motion of the aerostat [3]. The rigid body model of the aerostat includes the tail fins and the flying harness, both of which are held in place using flexible tethers. This approach assumes that the tethers are sufficiently taut to approximate rigid structures fixed to the hull.

3.3.1 Equations of Motion

The aerostat was considered as a rigid body with translational equations of motion derived from Newton's second law and rotational equations of motion using Euler's equation.

$$\begin{aligned} \mathbf{F}_I &= \mathbf{m}\mathbf{a}_I \\ \mathbf{M}_{cm} &= \mathbf{I}_{cm}\dot{\boldsymbol{\omega}} + \boldsymbol{\omega} \times \mathbf{I}_{cm}\boldsymbol{\omega} \end{aligned} \tag{3.8}$$

where $\mathbf{F}_I$ and $\mathbf{M}_{cm}$ are the net force and moments acting on the aerostat, $\mathbf{m}$ and $\mathbf{I}_{cm}$ are the aerostat's mass matrix and inertia tensor, $\mathbf{a}_I$ is the linear acceleration of its mass center expressed in the inertial frame, and $\boldsymbol{\omega} = [p\ q\ r]^T$ is its angular velocity. The aerostat's mass is represented by a diagonal matrix instead of a scalar because it includes added-mass terms whose directional components depend on geometry. Added mass and added moment of inertia will be discussed in Section 3.3.3. It is easier to actually solve the equations of motion with respect to the aerostat's body-fixed frame ($X_A\ Y_A\ Z_A$) since it represents the principal axis of the aerostat's mass matrix and inertia tensor. Therefore the translational equations of motion expressed in the aerostat's body frame are as follows:

$$\mathbf{F}_A = \mathbf{m}\left(\frac{^A d\mathbf{V}_A}{dt} + \omega \times \mathbf{V}_A\right) \tag{3.9}$$

where $\mathbf{V}_A = [u\ v\ w]^T$ is the velocity of the aerostat and its time derivative with respect to the aerostat's body frame is $\frac{^A d\mathbf{V}_A}{dt} = [\dot{u}\ \dot{v}\ \dot{w}]^T$. The force $\mathbf{F}_A$ and moment, $\mathbf{M}_{cm}$, which act on the aerostat are the sum from the following sources: gravity, buoyancy, aerodynamic and tether tension. The translational equations of motion in the body axes are as follows:

$$\begin{aligned} (mg - F_B)\sin\theta + F_{Hx} + F_{Px} + F_{Sx} + F_{Ux} + F_{Lx} &= m_x(\dot{u} + qw - rv) \\ -(mg - F_B)\sin\phi\cos\theta + F_{Hy} + F_{Py} + F_{Sy} + F_{Uy} + F_{Ly} &= m_y(\dot{v} + ru - pw) \\ -(mg - F_B)\cos\phi\cos\theta + F_{Hz} + F_{Pz} + F_{Sz} + F_{Uz} + F_{Lz} &= m_z(\dot{w} + pv - qu) \end{aligned} \tag{3.10}$$

where F_H, F_P, F_S, and F_U are the respective aerodynamic force contributions from the hull, port fin, starboard fin, upper fin, while F_L is the force exerted by the leash and F_B is the buoyancy force. The masses m_x, m_y, and m_z are the diagonal terms of the mass matrix. The Euler angles ϕ, θ, and ψ represent the aerostat's roll, pitch, and yaw. The three

rotational equations of motion are:

$$\begin{aligned}
-z_b F_b \sin\phi\cos\theta + M_{Hx} + M_{Px} + M_{Sx} + M_{Ux} + M_{Lx} = \\
I_{xx}\dot{p} - (I_{yy} - I_{zz})qr - I_{xz}(\dot{r} + pq) \\
-x_b F_b \cos\phi\cos\theta - z_b F_b \sin\theta + M_{Hy} + M_{Py} + M_{Sy} + M_{Uy} + M_{Ly} = \\
I_{yy}\dot{q} - (I_{zz} - I_{xx})pr - I_{xz}(r^2 - p^2) \\
-x_b F_b \sin\phi\cos\theta + M_{Hz} + M_{Pz} + M_{Sz} + M_{Uz} + M_{Lz} = \\
I_{zz}\dot{r} - (I_{xx} - I_{yy})pq - I_{xz}(\dot{p} - qr)
\end{aligned} \tag{3.11}$$

where M_H, M_P, M_S, and M_U are the respective aerodynamic moment contributions from the hull, port fin, starboard fin, upper fin and M_L is the moment caused by the leash force. The aerostat is symmetric with respect to the xz-plane ($I_{xy} = I_{yz} = 0$), and this is reflected in eq. 3.11.

Two additional kinematic equations are required to solve for the motion of the system as the above six equations of motion contain eight unknowns. The rigid body kinematic relationship between the angular rates, p, q, and r and the time rate of change of the Euler angles provide the additional equations required.

$$\begin{aligned}
\dot{\phi} &= p + (\sin\phi\tan\theta)\, q + (\cos\phi\tan\theta)\, r \\
\dot{\theta} &= (\cos\phi)\, q - (\sin\phi)\, r \\
\dot{\psi} &= (\sin\phi\sec\theta)\, q + (\cos\phi\sec\theta)\, r
\end{aligned} \tag{3.12}$$

Strictly speaking, the equation for the yaw rate, $\dot{\psi}$ is not required to solve for the motion of the aerostat as the motion equations and the kinematics equations are independent of the the yaw angle ψ.

3.3.2 Aerostat Aerodynamics

The component breakdown approach for modeling BOB has been presented in [3] and [25]. It relies on estimating individual lift and drag forces for the aerostat's components such as the hull, tail fins and flying harness. A summary of the aerodynamics forces are provided in Figure 3.5. Once these forces are estimated, the components in the body frame are applied to equations (3.10) and (3.11).

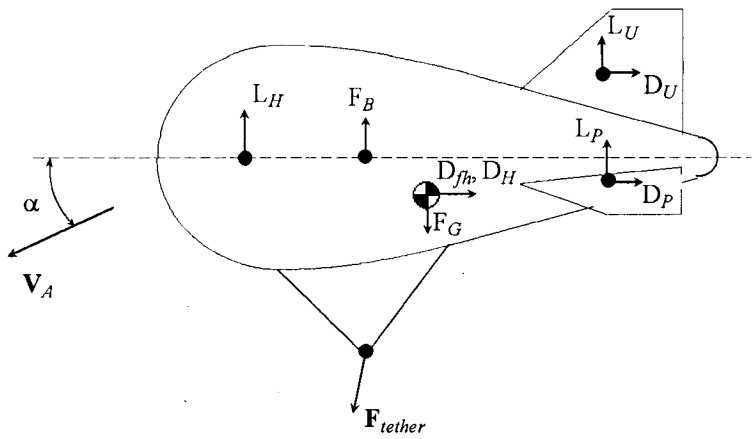

Figure 3.5: Aerodynamics forces acting on aerostat.

The aerodynamic forces from the hull, L_h and D_h are calculated using the method from Jones and DeLaurier [12] for aerostats in a steady flow. They represented the aerodynamics by three quantities, lift L_h, drag D_h, which are applied at the nose, and a pitch moment M_{nose}. The aerodynamics equations are as follows:

$$\begin{aligned}
\text{lift}: \; L_h &= q_0[(k_3 - k_1)\eta_k I_1 \sin(2\alpha)\cos(\frac{\alpha}{2}) + (Cd_c)_h J_1 \sin\alpha \sin|\alpha|] \\
\text{drag}: \; D_h &= q_0[(Cd_c)_0 S_h \cos^2\alpha - (k_3 - k_1)\eta_k I_1 \sin(2\alpha)\sin(\frac{\alpha}{2})] \\
\text{moment}: \; M_{nose} &= -q_0[(k_3 - k_1)\eta_k I_3 \sin(2\alpha)\cos(\frac{\alpha}{2}) + (Cd_c)_h J_2 \sin\alpha \sin|\alpha|]
\end{aligned} \tag{3.13}$$

where $q_0 = \rho V_A^2/2$ is the steady-state dynamic pressure, α is the angle of attack, k_1 and k_3 are respectively the axial and lateral added-mass coefficients, η_k is the hull efficiency factor accounting for the effect of the fins on the hull, $(Cd_c)_h$ is the hull's cross-flow drag coefficient, $(Cd_c)_0$ is the hull's zero-angle axial drag coefficient and S_h is the hull's reference area $S_h = (\text{hull volume})^{2/3}$. Also, the aerostat's geometric properties are reflected in the following four parameters:

$$\begin{aligned}
I_1 &= \int_0^{l_h} \frac{dA}{d\xi} d\xi \qquad & I_3 &= \int_0^{l_h} \xi \frac{dA}{d\xi} d\xi \\
J_1 &= \int_0^{l_h} 2r d\xi \qquad & J_2 &= \int_0^{l_h} 2r\xi d\xi
\end{aligned} \tag{3.14}$$

where A is the local cross-sectional area of the hull, ξ is the axial distance along the hull from the nose and r is the local hull radius. The methods used to estimate the aerodynamic

properties of BOB are presented along with the specific values for the relevant parameters in [25]. A list of the current aerodynamic parameters for BOB is given in Section 3.3.4.

For our model, the pitch moment was calculated but not applied directly to the aerostat; instead the hull's lift L_h was placed at an appropriate distance, x_L from the nose to generate the desired moment ($x_L = M_{nose}/L_h$).

Tail Fins

The aerodynamic forces generated by each tail fin are estimated by the following standard relationships:

$$\begin{aligned} L_i &= \frac{1}{2}\rho A_f V_i^2 C_L \\ D_i &= \frac{1}{2}\rho A_f V_i^2 C_D \end{aligned} \tag{3.15}$$

where A_f is the planform area of the fin, V_i is the local velocity of each fin and C_L and C_D are the lift and drag coefficients. The drag coefficient is the sum of two separate components termed the parasitic drag and the induced drag. Parasitic drag is invariable and the induced drag depends on the lift coefficient C_L as shown in the following equation:

$$C_D = C_{D_0} + \frac{C_L^2}{\pi A e} \tag{3.16}$$

where C_{D_0} is the parasitic drag coefficient, A is the aspect ratio of the fin and $e = 0.86$ is Oswald's efficiency factor [67]. The lift coefficient is proportional to the angle of attack α and the slope of the 3-D lift curve, C_{L_α}.

$$C_L = C_{L_\alpha}\alpha \tag{3.17}$$

The initial values for C_{L_α} and C_{D_0} were estimated using empirical data for the NACA 0018 airfoil [68]. Because the tail fins are not as slender as an airfoil, the parasitic drag coefficient was modified to conform to the semi-empirical relationship for elliptical cross-sections presented by Hoerner [69].

$$C_{D_0} = C_{f_{turb}}\left[4 + 2\frac{c}{t} + 120\left(\frac{t}{c}\right)^2\right] \tag{3.18}$$

	Length (m)	Diameter (mm)	Frontal Area (m^2)
Flying harness	120	6.35	0.76
Tail lines	243	3	0.729
Handling harness	128	8	1.01
Other	117	8	0.93

Table 3.1: Summary of BOB's accessory cables.

where c is the chord length of the tail fin, $c = 3.9$ m, t is the thickness, $t = 1.0$ m, and for the flow region above the critical Reynolds number, $C_{f_{turb}} = 0.005$. The pertinent tail fin parameters are summarized in Table 3.3.

Accessories

For flight operations, BOB is adorned with a significant number of ropes and tether accessories including its flying harness, tail-line supports and handling lines. Initially the aerodynamic effects of these accessories were neglected but after calculating the total frontal area of all BOB's associated cables to be in excess of 3 m, they were added to the model. Table 3.1 gives a breakdown of the various accessory cables. The flying harness is a series of 'U-shaped' cable lengths arranged in a manner that the leash load is distributed to the aerostat's 16 load patches along each side. The tail lines are thin ropes running fin to fin to form a tension structure to keep the fins in their proper place. The handling harness is similar to the flying harness but it is attached to a different series of load patches and it is only used for fixing the aerostat to the winches on the trailer bed. The other various accessory lines include two 50-m handling lines used to manually guide the aerostat during launch and retrieval.

The inclusion of the accessory cables to the aerostat's dynamics model is accomplished by adding two separate drag components. Since the tail lines are located at the tail fins, the extra drag due to the lines is reflected by an appropriate increase to drag coefficient in eq. (3.15). The remainder of the accessory lines are summed into one drag force, D_{fh}, applied at the centre of mass, calculated as:

$$D_{fh} = \frac{1}{2}\rho\mu_{fh}A_{fh}V_A^2C_d \tag{3.19}$$

where $A_{fh} = 2.7$ m^2 is the frontal area of the lines (both harnesses), C_d is the cable drag coefficient used in eq.(3.1) and $\mu_{fh} = 0.55$ is an efficiency factor to reflect that most of the tethers are not oriented normal to the incident flow and the loose handling lines are not rigidly secured in the flow field.

3.3.3 Added Mass and Added Moment of Inertia

Changes in the aerostat's velocity cause fluid particles to accelerate as they move around the exterior of the body. Therefore the fluid acquires kinetic energy through its interaction with the aerostat. The conventional approach to incorporate this effect is to include 'added mass' and 'added moments of inertia' to the equations of motion of the body [70]. This effect is more pronounced in marine applications and it is often ignored in aeronautical applications because the mass of the displaced fluid is much less than the mass of the vehicle. Because of the aerostat's large volume and low mass, added mass and inertia are not negligible in lighter-than-air applications. The aerostat mass matrix and inertia tensor are:

$$\mathbf{m} = \begin{bmatrix} m + m_{ax} & 0 & 0 \\ 0 & m + m_{ay} & 0 \\ 0 & 0 & m + m_{az} \end{bmatrix} \quad \mathbf{I}_{cm} = \begin{bmatrix} I_{xx} + I_{axx} & 0 & -I_{xz} \\ 0 & I_{yy} + I_{ayy} & 0 \\ -I_{zx} & 0 & I_{zz} + I_{azz} \end{bmatrix} \tag{3.20}$$

where the added mass terms m_a and added moment of inertia terms I_a were found using semi-empirical coefficients k_m and k_i for ellipsoids [70]. The added mass as well as the added moment of inertia were dimensionalized using the following equations:

$$m_a = k_m m^* \quad I_a = k_I I^* \tag{3.21}$$

where m^* and I^* are the mass and moment of inertia respectively of an ellipsoid of air with dimensions matching the aerostat BOB. The calculated values for added mass and inertia for BOB are given in Table 3.2. In the x-direction, $k_m = k_1$ of eq. (3.13) and in the y and z-directions, $k_m = k_3$.

m_{ax}	m_{ay}	m_{az}	I_{axx}	I_{ayy}	I_{azz}
89.2 kg	423.7 kg	423.7 kg	0	4672 kgm^2	4672 kgm^2

Table 3.2: Added mass and added moment of inertia for BOB.

3.3.4 Summary of Physical Parameters

Table 3.3 summarizes the physical parameters estimated for the aerostat BOB. The volume and mass of the internal helium and air varied from flight to flight as helium purity fluctuated. The values in Table 3.3 are from one specific flight on May 27, 2005.

Parameter	Value		Parameter	Value
I_{xx}	3184 kg·m^2		Helium volume	467.6 m^3
I_{yy}	10011 kg·m^2		Ballonet volume	43.2 m^3
I_{zz}	9808 kg·m^2		Total buoyant force	6442.6 N
$I_{xz} = I_{zx}$	641 kg·m^2		Helium mass	78.8 kg
k_1	0.16		Air mass	88.9 kg
k_3	0.76		Envelope mass	267.0 kg
η_k	1.27		Total mass	434.7 kg
$(Cd_c)_h$	0.28		Net lift	2178.2 N
$(Cd_h)_0$	0.05			
S_h	59.4 m^2		Tail fins:	
I_1	20.4 m^2		A_f	30 m^2
I_3	-170.5 m^3		A	2.18
J_1	75.8 m^2		C_{L_α}	2.0
J_2	434.4 m^3		C_{D_0}	0.098

Table 3.3: Summary of aerostat model parameters.

3.4 Instrument Platform

For simplicity the instrument platform was modeled as spherical shell that experiences only aerodynamic drag forces. The actual platform and its associated instruments differ from a sphere, but because its aerodynamics forces are expected to be small relative to the aerostat's forces and tether tensions, the spherical approximation is deemed to be adequate. The drag force for the platform, D_p is calculated using:

$$D_p = \frac{1}{2}\rho A_p V_p^2 C_{D_{sph}} \tag{3.22}$$

where A_p is the cross-sectional area of the approximated sphere (based on the actual diameter of the plate $D_p = 0.8$ m) and $C_{D_{sph}}$ is the drag coefficient of a sphere, which varies between 0.4 and 0.15 depending on Reynold's number [67]. The instrument platform's mass is 17.9 kg.

3.5 Control System

The original controller utilized in the dynamics model is based on PID control using feedback of the platform positioning error and was first presented by Nahon in 1999 [2]. The PID controller issues individual winch commands in the form of a desired tether velocity, which is calculated by feeding back the instantaneous estimate of the error of that particular tether length. The error for the i-th tether is approximated using:

$$e_i = \|\mathbf{r}_d - \mathbf{r}_{Wi}\| - \|\mathbf{r} - \mathbf{r}_{Wi}\| \tag{3.23}$$

where $\mathbf{r}$ is the position of the payload, $\mathbf{r}_d$ is the desired position and $\mathbf{r}_{Wi}$ is the position of the i-th winch. A 2-D representation of the geometry is shown in Figure 3.6. The idea behind this approach is that the only payload location at which $e_i = 0$ for $i = 1, 2, 3$ is where $\mathbf{r} = \mathbf{r}_d$. Thus, we can rely on independent control for each tether, acting together, to bring the payload to its desired location. The error e_i does not correspond to the exact error for each tether because it is calculated neglecting the curvature of the tether due to sag, but because the error distances tend to be much smaller that the total tether length, this estimate should suffice.

The PID controller acting on the tether length error is given by:

$$\dot{u}_i = K_D \dot{e}_i + K_P e_i + K_I \int e_i dt \tag{3.24}$$

where $\dot{u}_i$ is the control input and K_D, K_P and K_I are the derivative, proportional and integral control gains. The control input $\dot{u}_i$ was selected as a velocity so that it corresponds to the experimental control system, which operates at the velocity level.

To achieve the desired control input while simulating the dynamics, the unstretched length and the mass of the bottom-most tether element are adjusted at each integration

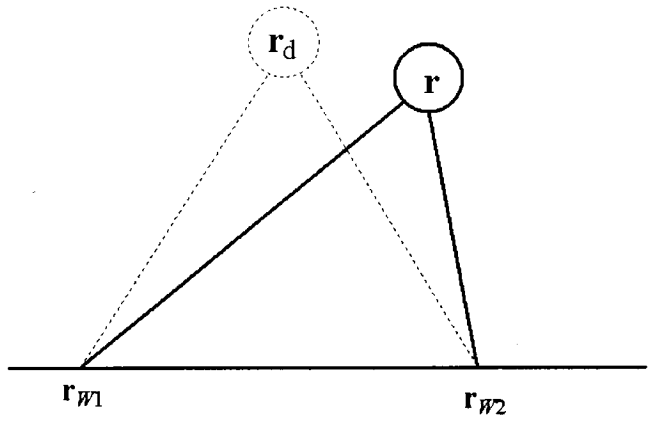

Figure 3.6: 2-D representation of tether geometry the payload's current position and desired position.

time-step. Since the control input, $\dot{u}_i$ is in the form of a velocity, it must be integrated to give u_i. The resulting equation for the unstretched length of the bottom-most element for the ith tether is given by:

$$l_u^i = l_{u_0}^i + u_i \tag{3.25}$$

where $l_{u_0}^i$ is the original length of the element. For the initial dynamics analysis and model validation, the winches are assumed to be perfect actuators, i.e. the desired tethers lengths are accomplished instantly and exactly. Although it is understood that the mechanical components of the winches possess characteristics such as inertia and friction that influence the dynamics of the closed-loop system, this influence is initially assumed to be negligible. The question of whether to include estimated winch dynamics in the model is addressed in Chapters 5 when the complete model is compared with closed-loop test results and again in Chapter 6 when advanced controllers are developed and tested.

The support tethers are typically discretized into 10 elements, each about 40 m in length, thus the method of specifying tether length changes in this manner is only valid up to 10% of the total tether length. This is sufficient for the current study because the regulator-type disturbance rejection control involves tether length changes well below 1 m. When the positioining system is modified to perform tracking maneuvers, further research is required to develop a suitable technique for accomodating large-magnitude parameter

variations of the discretized tether.

3.6 Wind Model

The wind field provides the disturbance to the dynamics model, and therefore the quality of our dynamics model relies heavily on an accurate wind model. The basic wind model as described in [2] contains a boundary-layer mean wind profile with superimposed turbulent gusts. The mean wind, U varies with height, h according to the following power-law profile representing the Earth's boundary layer:

$$U = U_g \left(\frac{h}{h_g}\right)^{\gamma} \tag{3.26}$$

where the power law exponent $\gamma = 0.30$ and the boundary layer height, $h_g = 500$ m were used to reflect the region's hilly terrain [71]. U_g is the full wind speed at the top of the boundary layer.

The stochastic turbulence is generated with desired gust properties including turbulence intensity, scale length and spectra. The turbulence intensities σ_u, σ_v, and σ_w in the three orthogonal directions were estimated from empirical data from Engineering Sciences Data Unit (ESDU) [72] resulting in the following equations:

$$\begin{aligned} \frac{\sigma_u}{U} &= 0.35 - 0.0635(h-10)^{0.25} \\ \frac{\sigma_v}{\sigma_u} &= 0.8 + \frac{h}{100} \\ \frac{\sigma_w}{\sigma_u} &= 0.5 + \frac{h}{250} \end{aligned} \tag{3.27}$$

The turbulent intensity, σ_i/U as a function of height is given in Figure 3.7. The profile for the current turbulent intensity model is compared to the original model developed in [2]. The differences between the models are the result of an increase to the surface roughness to reflect the hilly terrain near the test site, and a change in the extrapolation method for the intensities above 300 m. The ESDU data set has a maximum height of 300 m, and the original model assumed the intensities were equal above this height, whereas the new model assumes that the intensities continue to vary up until the upper limit of the boundary layer.

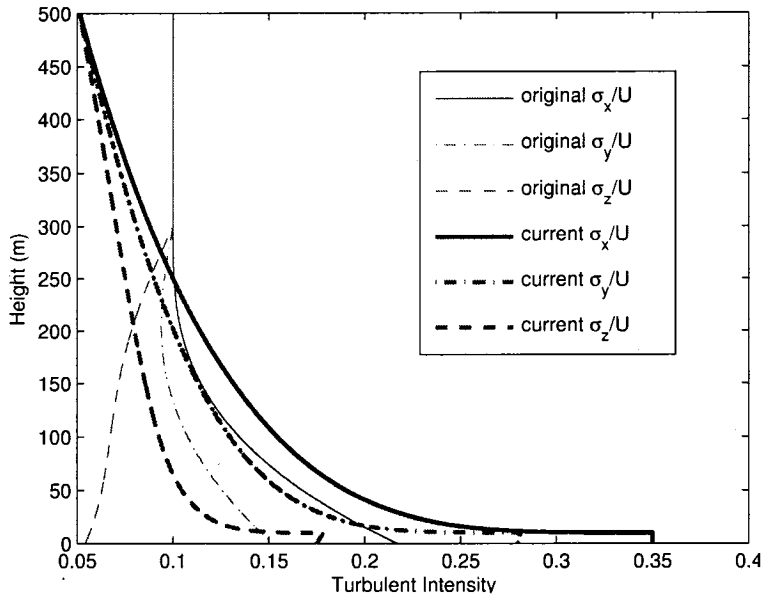

Figure 3.7: Comparison of the turbulent intensity profiles.

The scale lengths L_u, L_v and L_w of the turbulence are estimated using [73]:

$$\begin{aligned} L_u &= 280\left(\frac{h}{h_g}\right)^{0.35} \\ L_v &= 140\left(\frac{h}{h_g}\right)^{0.48} \\ L_w &= \begin{cases} 0.35h & h \leq 400\ m \\ 140 & h > 400\ m \end{cases} \end{aligned} \tag{3.28}$$

Finally, the spectra for the three components of turbulence, Φ_u, Φ_v and Φ_w are taken from a von Karman model [73] with:

$$\begin{aligned} \Phi_u(\Omega) &= \left(\frac{\sigma_u}{U}\right)^2 U^2 \frac{L_u}{\pi} \frac{1}{\left[1+(aL_u\Omega)^2\right]^{5/6}} \\ \Phi_v(\Omega) &= \left(\frac{\sigma_v}{U}\right)^2 U^2 \frac{L_v}{2\pi} \frac{1+\frac{8}{3}(aL_v\Omega)^2}{\left[1+(aL_v\Omega)^2\right]^{11/16}} \\ \Phi_w(\Omega) &= \left(\frac{\sigma_w}{U}\right)^2 U^2 \frac{L_w}{2\pi} \frac{1+\frac{8}{3}(aL_w\Omega)^2}{\left[1+(aL_w\Omega)^2\right]^{11/16}} \end{aligned} \tag{3.29}$$

where Ω is the wave number and $a = 1.339$. The specific procedure for generating the gust velocities based on eqs.(3.27) to (3.29) is provided by Nahon in [2].

During the model validation process in Chapters 4 and 5, certain parameters in the turbulence model, such as the turbulence intensity, were adjusted based on the statistical properties of the measured wind during a particular flight. The details of approximating the measured wind are covered in the next chapter.

3.7 Numerical Solution

The dynamics of each discretized tether node, the payload node and the aerostat node are described by three second-order ordinary differential equations (ODEs) obtained using the translational motion equations. The aerostat's rotations are described by an additional three rotational equations of motion and two kinematic equations. The original ODEs are expanded in state-space form to yield first-order ODEs for the acceleration and velocity of each node. Each support tether is typically discretized into 10 elements, while the leash is split into two elements. Therefore the total number of discretized nodes is 30 (27 for the support tethers, one for the payload, one for the leash, and one for the aerostat) which gives a total of 186 state variable and 186 first-order ODEs (six for each node plus an additional six for the aerostat). The motion of the system is obtained by simultaneously solving the ODE's using a fourth-order Runge-Kutta numerical integration routine.

The initial conditions for the dynamics simulation are provided by a static model of the system [26], which estimates the position of and forces acting on each node for any specified tether geometry and steady-state wind conditions. This ensures that the dynamics simulation starts from a static equilibrium configuration.

3.8 Linear Model

While the nonlinear simulation is central to predicting the dynamic behaviour of the multi-tethered aerostat system, for certain analysis and for controller development, it is often convenient to represent the dynamics with a linear model. Instead of analytically linearizing the numerous nonlinear equations describing the system, a numerical approach exploiting the nonlinear simulation proves to be straightforward and effective.

The nonlinear dynamics of the system can be represented as a set of functional relationships where the derivative of each state variable is dependent on the full set of state variables and input variables. This is demonstrated by the following equation:

$$\dot{\mathbf{x}} = \mathbf{F}(\mathbf{x}, \mathbf{u}) \tag{3.30}$$

where the state vector $\mathbf{x}$ contains the position and velocity of all the discretized nodes in the model (including the angular position and velocity of the aerostat node) with respect to the inertial frame. The input vector $\mathbf{u}$ contains the winch input for each tether, which as mentioned earlier, is the change in length of the lower-most tether element.

Linearizing eq.(3.30) gives the linear time invariant (LTI) system:

$$\dot{\mathbf{x}} = \mathbf{A}\mathbf{x} + \mathbf{B}\mathbf{u} \tag{3.31}$$

where the state matrix $\mathbf{A}$ and the input matrix $\mathbf{B}$ are defined as:

$$\begin{aligned} \mathbf{A} &= \frac{\partial \mathbf{F}}{\partial \mathbf{x}} = \begin{bmatrix} \frac{\partial f_1}{\partial x_1} & \frac{\partial f_1}{\partial x_2} & \cdots & \frac{\partial f_1}{\partial x_n} \\ \frac{\partial f_2}{\partial x_1} & \frac{\partial f_2}{\partial x_2} & \cdots & \frac{\partial f_2}{\partial x_n} \\ \vdots & \vdots & \ddots & \vdots \\ \frac{\partial f_n}{\partial x_1} & \frac{\partial f_n}{\partial x_2} & \cdots & \frac{\partial f_n}{\partial x_n} \end{bmatrix} \\ \mathbf{B} &= \frac{\partial \mathbf{F}}{\partial \mathbf{u}} = \begin{bmatrix} \frac{\partial f_1}{\partial u_1} & \frac{\partial f_1}{\partial u_2} & \cdots & \frac{\partial f_1}{\partial u_m} \\ \frac{\partial f_2}{\partial u_1} & \frac{\partial f_2}{\partial u_2} & \cdots & \frac{\partial f_2}{\partial u_m} \\ \vdots & \vdots & \ddots & \vdots \\ \frac{\partial f_n}{\partial u_1} & \frac{\partial f_n}{\partial u_2} & \cdots & \frac{\partial f_n}{\partial u_m} \end{bmatrix} \end{aligned} \tag{3.32}$$

and $n = 186$ is the total number of state variables and $m = 3$ is the number of tethers or winches. The numerical approach for obtaining $\mathbf{A}$ and $\mathbf{B}$ is to approximate the nonlinear differential equations by performing numerical differentiations using a central difference approach. From a reference equilibrium position, each state variable and each input variable is individually perturbed by $\pm\Delta$ and the ensuing response of every state variable is recorded. The difference between the responses to the positive and negative perturbations are divided by twice the magnitude of the perturbation, 2Δ, to complete the central difference calculation. For example, in the case of the first element in the first row of $\mathbf{A}$ we have:

$$\frac{\partial f_1}{\partial x_1} \approx \frac{f_1(x_{1_0} + \Delta) - f_1(x_{1_0} - \Delta)}{2\Delta} \tag{3.33}$$

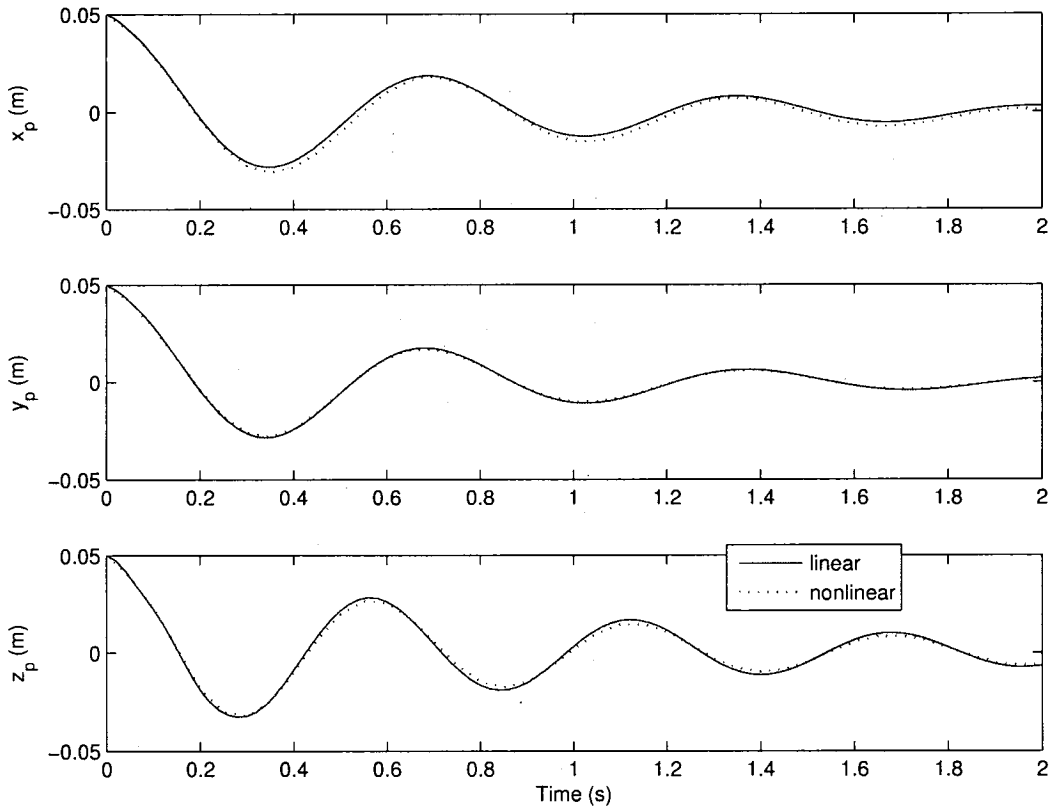

Figure 3.8: Comparison of simulated linear and nonlinear zero-input response of platform position.

where x_{1_0} is the equilibrium value for x_1. The value for the perturbation, Δ, is typically very small (10^{-6} was used). The reference equilibrium condition is one in which the tethered aerostat system is in a steady state wind field in the absence of turbulence.

3.8.1 Linear Results

To determine how well the linear model approximates the nonlinear model, the simulated response of the two models are compared. As a first step, the comparison is based on the zero-input response with $\mathbf{u} = \mathbf{0}$, as the system is subjected to non-zero initial conditions. Figure 3.8 gives the motion of the platform relative to the equilibrium point, which was at the symmetric configuration ($\theta_{ze} = 0°$) with a wind speed of $U = 5$ m/s. The initial conditions, $\mathbf{x_0}$ were all zeros except for the states of the platform position in all three

directions which had a value of 0.05 m ($x_0^{164} = x_0^{166} = x_0^{168} = 0.05$ m). The results show excellent agreement between the zero-input response of the nonlinear and linear models.

The resemblance between the two sets of results is not unexpected as the nonlinear characteristics within the model are related to aerodynamics or geometry and thus only become prominent during strong winds, extreme maneuvers or configurations far from the equilibrium point. The comparison between the linear and nonlinear models is expanded in Chapter 6 to include not only the zero-input response, but also the response with exogenous input and closed-loop control.

Chapter 4

Passive Response of System

Every dynamics model is a mere approximation of the true behaviour of a system, just as any experimental measurement is only an approximation of the actual quantity. Measurements, when performed properly, are expected to offer much better estimation than even the most comprehensive dynamics model. Therefore, to evaluate the quality of a dynamics model, it must be compared to experimental measurements of the dynamic behaviour in question.

The objective of this chapter is to document experimental results from the first set of flight tests, in which tether lengths were fixed, and assess the passive behaviour of the dynamics model for the multi-tethered aerostat system (without tether actuation) [74]. This is accomplished at two different levels; the first focuses on an isolated tether structure, which shows excellent agreement when its input is equal to the measured input, and the second includes the aerostat and the wind model, which shows agreement only at a statistical level because of uncertainty involved with matching the wind input. With the fidelity of the dynamics model of the passive system established, a design application using simulation results to evaluate two types of aerostats is presented.

4.1 Flight Tests

The first round of fully instrumented test flights of the tri-tethered aerostat system performed at DRAO occurred during the spring of 2004. The objective of these flights was

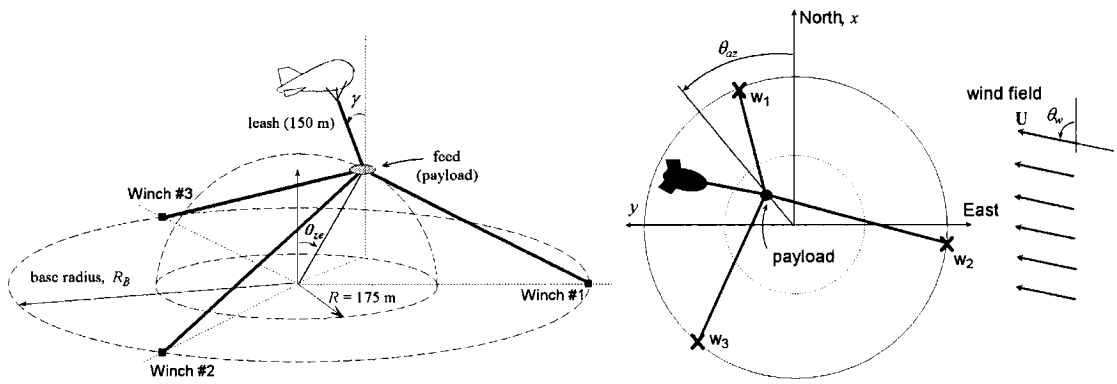

(a) (b)

Figure 4.1: a) Layout of LAR multi-tethered positioning system, b) overhead view.

	#1 March 11	#2 March 23	#3 April 21	#4 June 15
Base radius, R_B(m)	250	250	400	400
Zenith, θ_{ze}(deg)	2	29	29	2
Azimuth θ_{az}(deg)	-101	-40	-40	-101
Platform height, z (m)	175.4	155.7	150.2	172.8
Aerostat net lift (N)	1913	1717	1825	2325

Table 4.1: Summary of Spring 2004 test flights.

to study the passive or uncontrolled performance of the system in response to typical wind conditions. Each test was performed with a different geometric configuration to assess how the geometry affects the behaviour of the system. Two flights were near the central or symmetric configuration, while two others were at a zenith angle near 30°. The radius of the circle at which the tethers are anchored to the ground, termed the base radius or the winch radius, R_B also varied between 250 m and 400 m. The layout of the experimental system with its geometric parameters is given in Figure 4.1, and a summary of the four flight tests is given in Table 4.1. The focal length for the flights was approximately $R = 175$ m which is slightly higher than the intended 167-m focal length for the one-third scale system, but the difference is not expected to affect the results. The net lift of the aerostat is included in Table 4.1 because it has a significant impact on the performance of the system, and because it varies from flight to flight depending on the purity of helium in the envelope and the atmospheric conditions.

	#1 March 11	#2 March 23	#3 April 21	#4 June 15
Wind speed, U(m/s)	4.94	4.49	3.15	3.75
Wind direction, θ_w(deg)	185	203	174	185
Turbulence intensity, σ_U/U	0.14	0.06	0.10	0.16
Horiz. position $\sigma_{aerostat}$(m)	4.26	3.31	2.63	3.32
Horiz. position $\sigma_{platform}$(m)	0.03	0.93	0.06	0.03
% reduction	99.3	71.9	97.7	99.1
Vert. position $\sigma_{aerostat}$(m)	0.41	0.22	0.17	0.13
Vert. position $\sigma_{platform}$(m)	0.09	0.21	0.08	0.10
% reduction	77.4	5.5	54.7	29.1
Leash tension, T_L(N)	2473	1849	1897	2627
Tether 1 tension, T_1(N)	1309	1036	1356	1238
Tether 2 tension, T_2(N)	975	913	1287	1193
Tether 3 tension, T_3(N)	805	173	717	1091

Table 4.2: Test results for mean wind speed, turbulence intensity, aerostat and platform motion (standard deviation) and mean tether tension.

4.1.1 Passive Flight Results

Results for the four passive test flights are presented in Table 4.2. Mean values for the wind speed and tether tension are included, while the standard deviation of the platform and aerostat motion, in both horizontal and vertical directions is provided. The results are based on tests with a duration of approximately 15 minutes. Also included is the percent reduction in motion between the aerostat and the platform, which gives a rough estimate of the stiffness of the particular configuration.

4.1.2 Motion Reduction

The station keeping abilities of the system can be evaluated by considering the standard deviation of the platform position. With the exception of Flight 2, which was at an unfavorable configuration, the system was effective in limiting the standard deviation of the platform motion to within 5 cm horizontally and 10 cm vertically. The efficacy of the system is also made apparent by the significant reduction in horizontal motion between the aerostat and platform. During Flights 1 and 4, which are both at favorable low zenith angles, the standard deviation of the horizontal motion of the platform was two orders

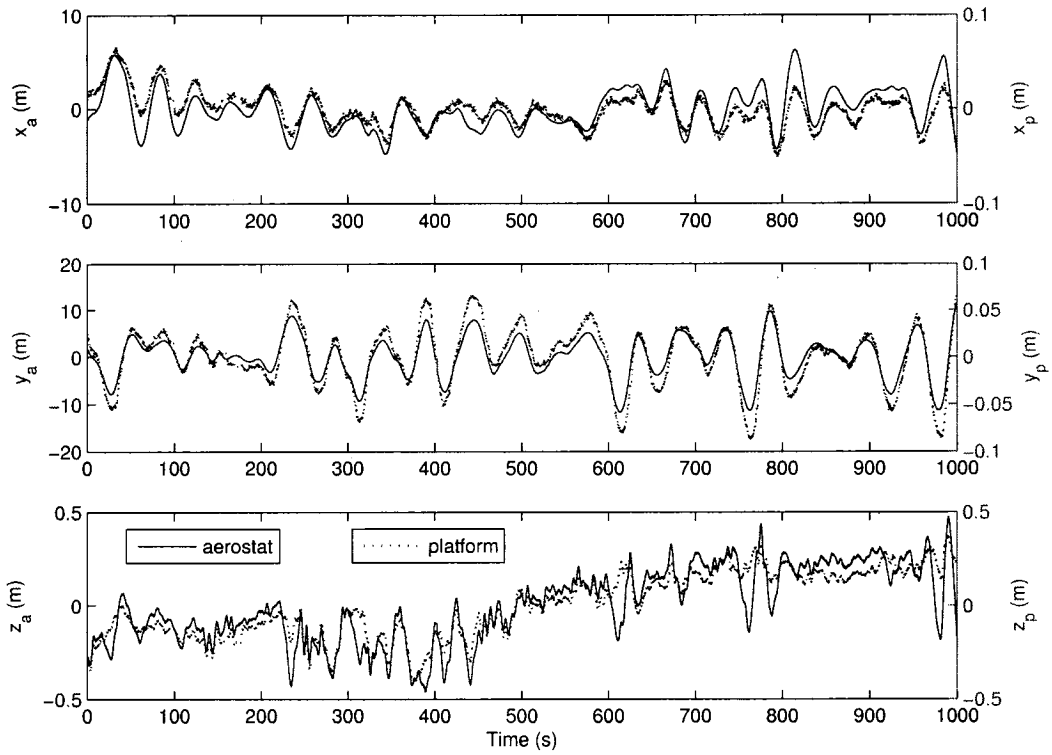

Figure 4.2: Comparison of the motion of the aerostat (left axis) and the instrument platform (right axis) about their mean positions during Flight #4.

of magnitude smaller than the aerostat motion. Vertical motion of the platform was also smaller but the improvement was much less marked. Figure 4.2 presents a plot of the motion of both the platform and aerostat during Flight 4. There is obvious correspondence between the motions of the two bodies in the x and y horizontal directions with the platform lagging the aerostat slightly. Despite the significantly smaller magnitude of motion in the horizontal direction, in the vertical z-direction, the motion of the platform and the aerostat are of the same order of magnitude.

Figure 4.3 displays the statistical coherence between the motion variables of the two bodies in the x, y and z directions. The coherence function, $C_{ab}(f)$, of two real-valued signals, $a(t)$ and $b(t)$, for a specific frequency, f, is given by [75]:

$$C_{ab}^2(f) = \frac{|P_{ab}(f)|^2}{P_{aa}(f)P_{bb}(f)} \tag{4.1}$$

where $P_{ab}(f)$ is the cross-power spectral density of the two signals and $P_{aa}(f)$ and $P_{bb}(f)$

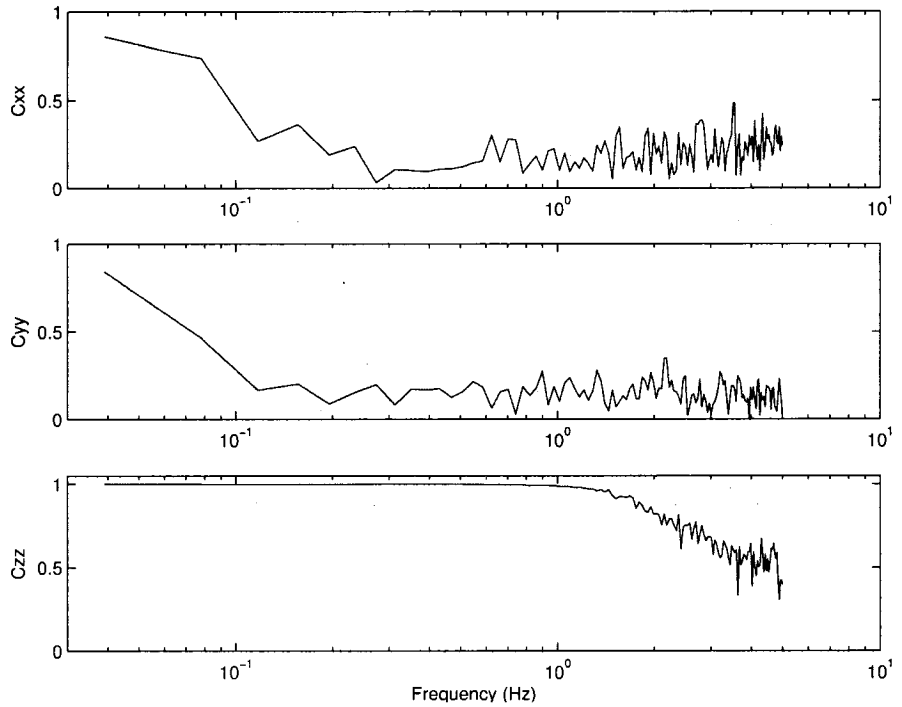

Figure 4.3: Statistical coherence between aerostat position and platform position for Flight #4.

are the power spectral densities of a and b respectively. The coherence function, which ranges from zero to one, quantifies the correlation of two signals over a range of frequencies. A coherence of zero indicates incoherent signals, while a value of one indicates full coherence or correlation. Horizontally, there is coherence at only the lowest frequencies, observed in the time histories in Figure 4.2, and above 0.1 Hz, there is negligible coherence. Vertically, there is strong coherence between the two bodies beyond 1 Hz. The coherence plots clearly demonstrate the tri-tethered system's ability to filter out all but low frequency horizontal motions, while highlighting its inability to filter out any vertical motions below 1 Hz.

4.1.3 Varying Geometry

It is difficult to directly compare the performance of the four different geometric configurations tested since several influential factors were not controlled during the tests such

as wind speed, turbulence intensity, and aerostat lift. However, it is still possible to make qualitative observations regarding the relative performance of these configurations. It is clear that the worst performance was observed during Flight 2, which was tested at a small base radius and high zenith angle. This geometry considerably reduced the stiffness of the system by two different mechanisms. First, the structural stiffness of the tripod is reduced in certain directions due to the asymmetry of the system. Secondly, the tether asymmetry causes tension to drop in one tether, thus increasing its catenary, or sag, and reducing its effective stiffness. During Flight 2, the mean tension in tether 3 was only 173 N and the standard deviation of the horizontal displacement of the platform was almost 1 m, while for all other flights it was less than 6 cm. It is clear that such a significant drop in tension in any of the tethers leads to performance degradation. It should be mentioned that the net lift of the aerostat was lowest during this flight, also contributing to the poor performance.

To ensure adequate performance of the system, a certain tension level must be maintained in all tethers at all times. Increasing the lift of the aerostat is one suitable method to achieve this, although not practical for our experiments, but a second, more practical, solution is to increase the base radius R_B for high zenith configurations. The larger base radius of 400 m significantly improved the performance of the system at a high zenith angle as observed in a comparison of results between Flight 2 and Flight 3. For the tests near the zero zenith, Flights 1 and 4, the wider base radius is observed to reduce the stiffness in the vertical direction while having little effect on the horizontal stiffness.

4.1.4 Summary of Passive Flight Tests

Overall, the test results show that precise station-keeping is possible with a tri-tethered aerostat system as a 18-kg platform was held to within 10 cm RMS error at heights ranging from 150 m to 175 m. The geometry of the tether layout was shown to significantly affect performance of the system, and the importance of maintaining sufficient tension in all tethers was highlighted. Optimizing design parameters such as aerostat lift, tether size and material, geometry, and the number of tethers could likely enhance performance further.

As mentioned in Section 2.1, the preliminary design specifications for the functioning LAR telescope (which would be three times larger than our experimental system) call for maintaining a receiver position within 1.5-cm RMS of the reflector focus. It is expected that this level of precision can be achieved with the use of a secondary mechanism, the CPM, installed at the confluence point to perform fine corrections, if the tethered aerostat system can achieve accuracy of roughly 0.5-m RMS. This translates to 17 cm for our one-third scale experimental system. Our results suggest that even the passive system may deliver the precision required, but the limited number of conditions tested precludes definitive claims about performance of the telescope at this time. It should be mentioned that although the passive system meets the rough design specifications for the required LAR system for these four flights, closed-loop control of the tethers is still considered important as any improvement to the 0.5-m precision will reduce the demands on the CPM, which could lead to a less complicated and leaner design.

4.2 Validation of Passive Response

To simplify the overall model validation process, and gain a better understanding of the possible sources of model discrepancies, an iterative approach is taken. First the model of the tri-tethered support structure is validated, and once the accuracy of the tether model is established, the entire model of the passive system including the aerostat aerodynamics and the wind model is validated.

4.2.1 Tether Model Only

The tether model can be compared to the experimental data in isolation from the aerostat provided that the dynamics input is accurately measured and reproduced faithfully within the model of the tethered system. Prior simulations have suggested that the vast majority of dynamics of the LAR payload or platform are the direct result of perturbations in the force exerted by the aerostat's leash. This is not surprising when the aerostat's size relative to the rest of the system is considered. Since the leash tension is measured during the flights,

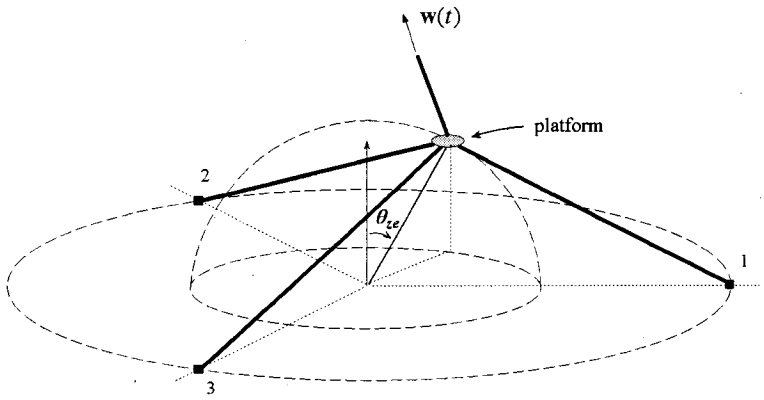

Figure 4.4: LAR system with aerostat removed and replaced by leash force.

it becomes possible to simulate the behaviour of the tethered system using the actual measured disturbance function, $\mathbf{w}(t)$. A schematic of this arrangement is given in Figure 4.4. The load cell measuring leash tension is located at the aerostat/leash attachment point, and therefore, within the dynamics model the measured force is applied at the top leash node. The load cell measures the tension, $T_L(t)$ which is a scalar quantity, but its direction is also required to give the vector $\mathbf{w}(t)$. To estimate the direction of the leash force, a position vector from the platform to the leash/aerostat attachment point was calculated by subtracting the GPS position measurements of the platform, $\mathbf{r}_p$ from the aerostat position, $\mathbf{r}_a$.

$$\mathbf{w} = T_L \frac{\mathbf{r}_a - \mathbf{r}_p}{\|\mathbf{r}_a - \mathbf{r}_p\|} \tag{4.2}$$

A comparison of the flight data from the four Spring 2004 flights and simulated results using measured leash tensions to replace the aerostat is presented in Table 4.3. The percentage difference between the standard deviation of the experimental and simulated platform motion and tether tensions are given. The results for Flight 3 are presented in Figure 4.5 to illustrate how well the tether model predicts the platform motion when the measured leash tension is used as input. In the z-direction, an offset is required in the intitial conditions for the simulation to match the position at the end of the test due to the vertical drift in the measured position. The drift is believed to be caused by creep in the tethers, which is not included in the model. For all calculations of the standard deviation of the experimental

	#1 March 11	#2 March 23	#3 April 21	#4 June 15
Horiz. position	2.4	-1.6	3.8	-5.4
Vert. position	-20.8	0.7	-3.7	-11.4
Tether 1 tension	-2.6	0.4	1.2	-1.9
Tether 2 tension	0.9	0.2	3.0	3.1
Tether 3 tension	3.8	3.4	4.3	2.4

Table 4.3: Percentage difference between the standard deviation of the experimental data and simulated data using the measured leash force.

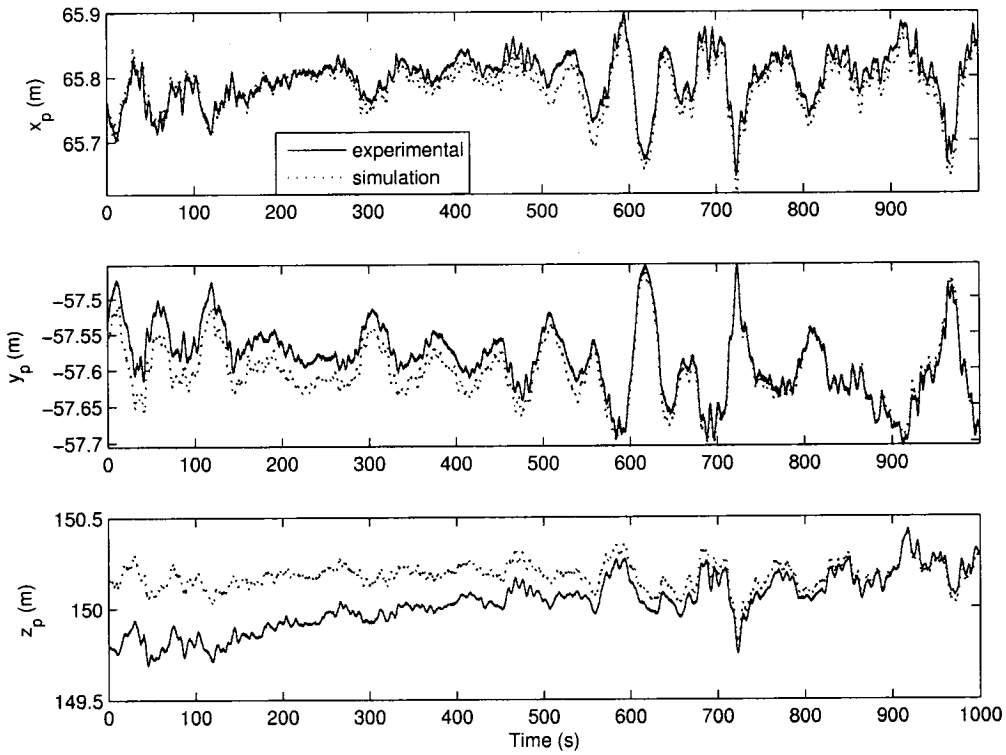

Figure 4.5: Measured and simulated platform position to validate the tether model for Flight #3.

vertical motion, the creep rate was disregarded by removing the linear trend from the data. Creep is not expected to be a problem with functioning winches as the creep rate of approx 0.1 mm/s can be corrected easily.

The values for the tether tension and horizontal motion are all within 6%, which is indicative of a satisfactory tether model. For the vertical motion, the percentage difference is as large as 21%; however, the values for the standard deviation of the measured vertical

motion may be skewed slightly due to the observed creep. Although a linear trend is removed from the motion prior to the calculation, if the creep rate is not constant, the standard deviation of the measured results will be exaggerated.

4.2.2 Complete Model

Results are now presented for the validation of the complete dynamics model of the system. The statistics of the measured wind conditions for each particular flight were provided as input to the model and the motion of the system was simulated and compared to the actual measured data. Because the wind speed was measured 150 m below the aerostat, the wind field in the vicinity of the aerostat is not precisely known. This limits the extent of our validation effort, as a direct temporal comparison to experimental data is not possible. As detailed below, the modeled wind field, for our simulation, is spatially extrapolated from the measurement platform based on statistical approximations of the actual wind conditions. Since the wind speed at the aerostat, which is responsible for the majority of the disturbances in the system, is modeled based on a statistical approximation of the actual wind field, the validation of the dynamics model must be based on statistical results.

Recreating the Measured Wind

The following steps were taken to ensure that the wind field in the simulation was statistically similar to that in the field:

1. The low-frequency characteristics of the wind were approximated by fitting a curve to the general trend of the wind speed at its measurement height.

2. The vertical profile of the basic wind field was generated using a power-law boundary layer profile, as discussed in Section 3.6.

3. The mean wind-direction was estimated by averaging the mean wind-sensor measurement at the platform and the mean yaw angle of the aerostat.

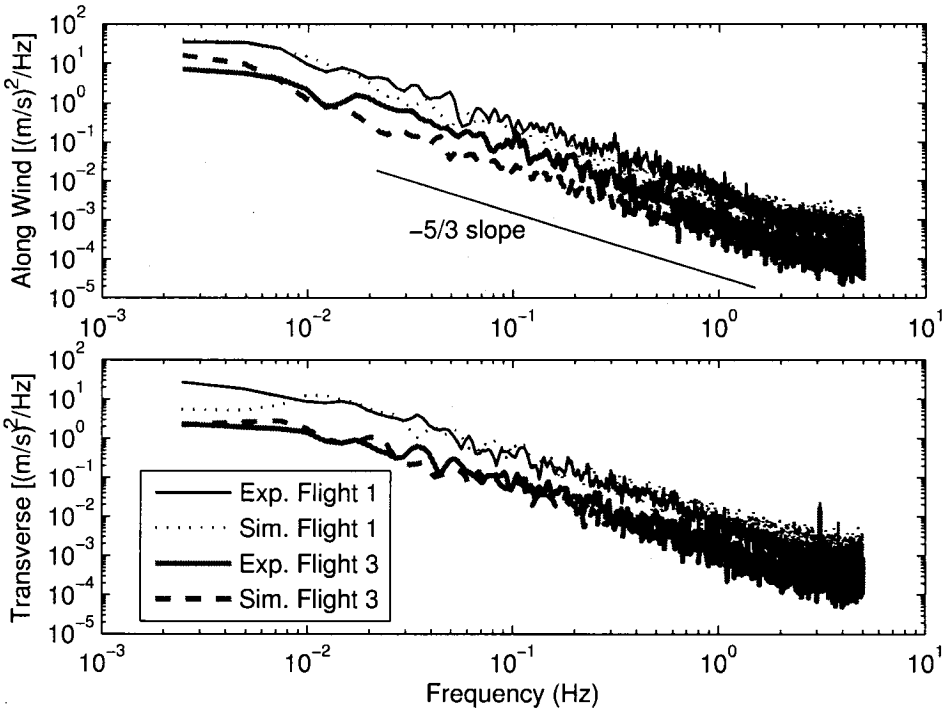

Figure 4.6: The power spectral density for the measured and simulated horizontal turbulence, along and transverse to the wind direction, for Flights #1 and #3.

4. Turbulent gusts were superimposed on the basic wind field, which are approximated using Von Karman spectra [2] based on the measured turbulence intensity for the test period. The vertical profile of the turbulence intensity, which decreases with height, is extrapolated from the measurement location using empirical data [72].

A limitation of this approach arises because only the horizontal component of the wind speed is measured, and thus the vertical turbulence is unknown. Although the vertical component of the wind is not expected to be large, it can have a significant impact on the motion of the aerostat [15]. An estimate of the vertical component of turbulence, relative to the measured horizontal turbulence levels, is included in the model. However, since no vertical wind speed measurements are available, there is considerable uncertainty in our results pertaining to possible updrafts or downdrafts.

The frequency content of the measured and simulated turbulence is compared in Figure 4.6, which gives the power spectral density (PSD) in directions along and perpendicular

Parameter		Flight #1 March 11			Flight #3 April 21		
		Exp.	Sim.	% diff.	Exp.	Sim.	% diff.
Platform Position (m)	σ_x	0.021	0.020	-6.7	0.039	0.047	19.8
	σ_y	0.030	0.048	60.7	0.042	0.044	3.18
	σ_z	0.093	0.085	-8.4	0.077	0.105	37.2
Aerostat Position(m)	x_a	-19.94	-15.67	21.4	62.26	57.43	-7.8
	y_a	-9.85	-7.17	27.2	-58.82	-56.48	-4.0
	z_a	337.36	337.73	0.1	312.66	312.57	0.03
	σ_x	3.13	2.86	-8.6	2.33	1.28	-45.1
	σ_y	5.09	7.68	51.0	4.76	3.15	-33.8
	σ_z	0.411	0.388	-5.6	0.170	0.150	-11.4
Leash angle (deg)	γ	6.9	5.7	-17.6	1.9	3.1	61.6
Aerostat Rotation (deg)	σ_ϕ	2.11	2.35	11.0	1.70	0.95	-44.2
	σ_θ	1.10	0.96	-13.0	0.59	0.40	-31.6
	σ_ψ	5.24	4.77	-9.1	11.78	2.41	-79.5
Tether Tension (N)	T_L	2473	2220	-10.2	1897	1882	-0.87
	σ_{T_L}	182	190	4.28	35	50	42.7
	σ_{T_1}	124	130	5.4	45	55	20.7
	σ_{T_2}	126	136	7.7	51	61	19.5
	σ_{T_3}	89	113	26.5	30	33	8.8

Table 4.4: Comparison of experimental and simulated results for Flights 1 and 3.

to the mean wind direction. For brevity, only results for Flights 1 and 3 are presented. The simulated turbulence appears to have the approximate characteristics of the measured turbulence throughout the bandwidth of our sensor, but it is clear that the turbulence model does not always recreate the actual wind spectrum, which varies significantly day to day. The dropoff at high frequencies in the spectra for both experimental and simulated wind data adhere to the expected -5/3 slope for isotropic turbulence [76]. The spike in the experimental data of the lower plot is the result of a cooling fan onboard the platform that causes small amplitude vibrations.

Statistical Comparison of Simulation and Experimental Results

For brevity, only two of the four passive test flights are included in this comparison. Table 4.4 presents a comparison of the measured and simulated data for platform position, aerostat position and rotation, and tether tension for Flights #1 and #3. These two flights

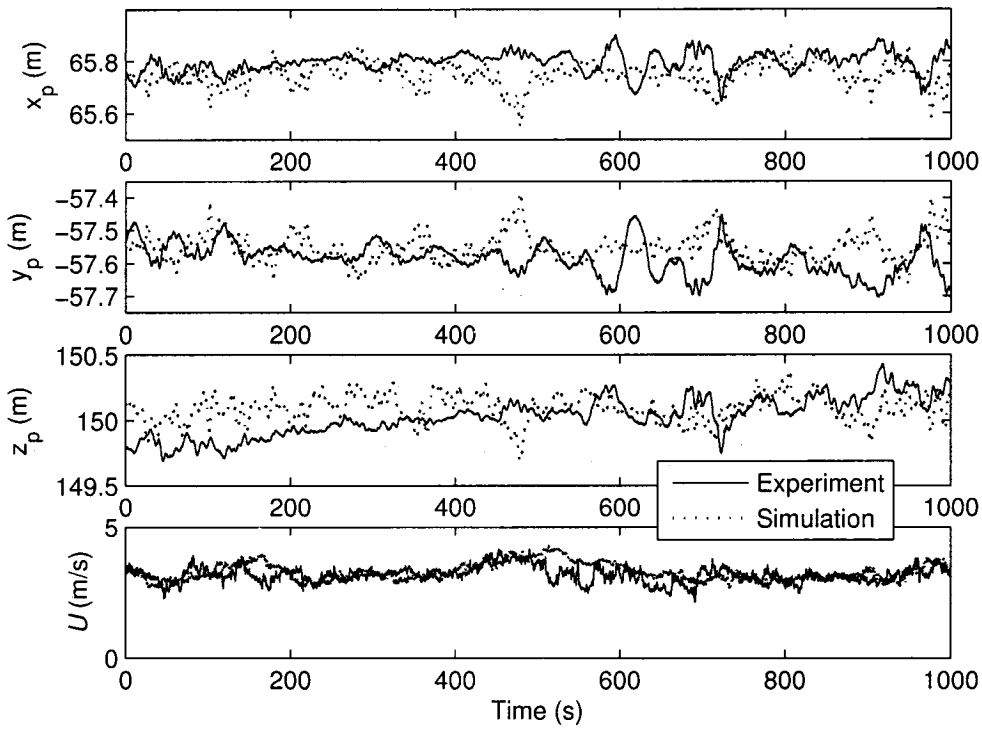

Figure 4.7: Comparison of experimental and simulated results of platform position and wind speed for Flight #3.

were selected because they represent the extremes of the observed range of the validation results. For all parameters except the aerostat position, leash angle and tension, the mean values are omitted and only a comparison of the standard deviation is presented. During both test flights, the predominant wind direction was North, which is aligned with the x-axis of our inertial frame. Thus, the lateral motion of the aerostat is represented by motion in the y-direction along with the aerostat roll, ϕ, and yaw, ψ, while the longitudinal motion is described by motion in the x and z directions as well as aerostat pitch, θ.

Figures 4.7 through 4.9 compare time histories of measured and simulated results for Flight 3. It is emphasized that the simulated results are not expected to directly follow the measured results because the simulated wind turbulence was based only on the statistical properties of the measured wind, not on the wind's precise time history. The goal of comparing time histories is to provide a general assessment of the simulation's accuracy.

For Flight 3, the simulation results for the horizontal platform motion are within 20%

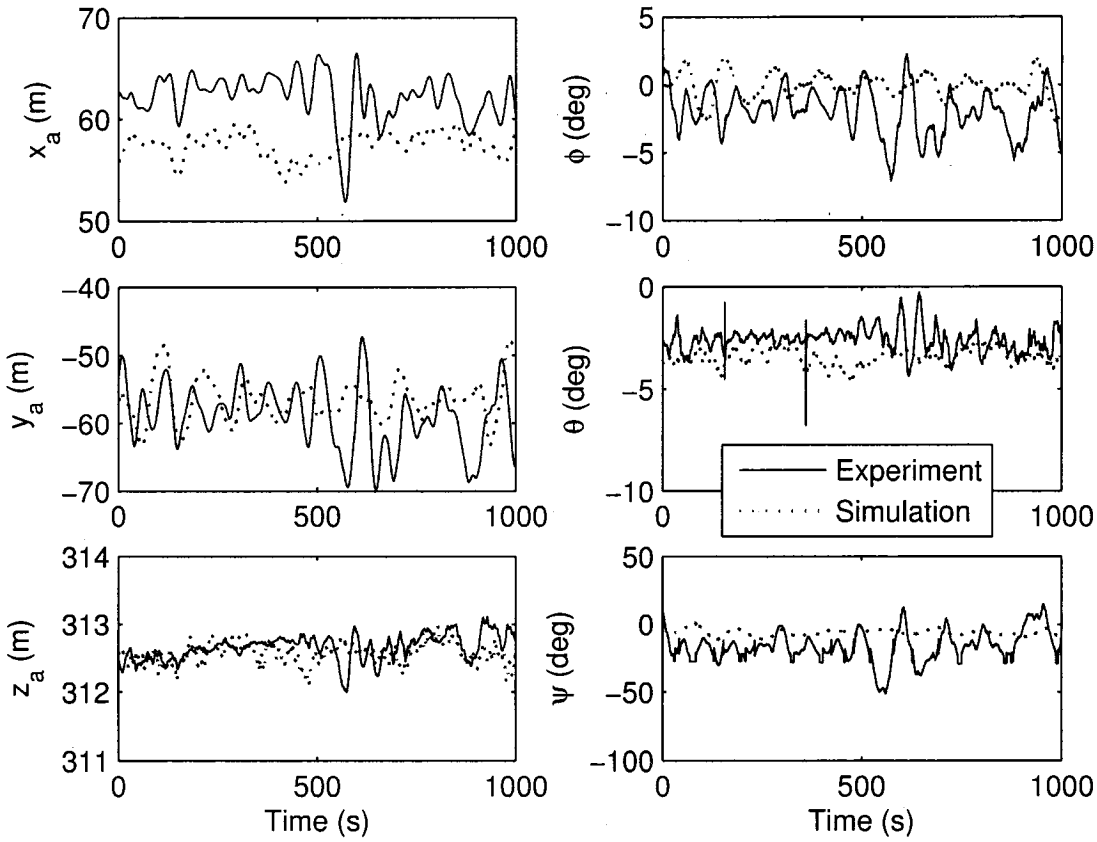

Figure 4.8: Comparison of experimental and simulated results for aerostat position and orientation for Flight #3.

of the actual results, which is encouraging considering this corresponds to accuracy of less than a centimeter. For Flight 1, the predicted platform motion differs by as much as 60% in the lateral or y-direction, which seems large, however, this corresponds to a difference in motion of less than 2 cm. Considering the size of the positioning system: the platform is 175 m high, anchored by tethers hundreds of meters long; a 2-cm discrepancy is more than satisfactory for this analysis. There are several instances where our simulated results diverge from the measurements, but these differences are not consistent across all the test cases. During Flight 1, the simulation over-predicted the lateral position of the platform by 60% while the variation in yaw was within 10%. The reverse is observed during Flight 3, as the standard deviation of the aerostat yaw angle differs by 80% while the lateral position is predicted to within 5%.

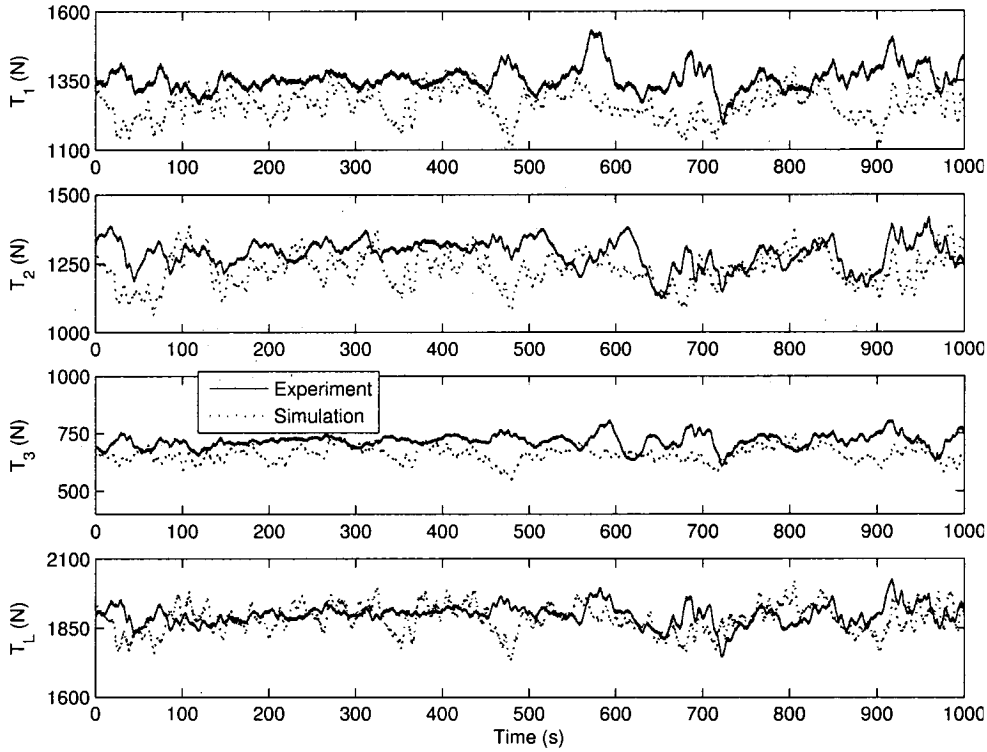

Figure 4.9: Comparison of experimental and simulated results of tether tension for Flight #3.

In terms of the longitudinal motion of the aerostat, it is observed in Figure 4.8 that during Flight 3, the simulated aerostat position in the x-direction is 4 m less than measured corresponding to a larger blow-down angle, or leash angle, γ (shown in Figure 4.1) in the simulation. This suggests that either the wind speed or the drag coefficient or both are overestimated. Conversely, during Flight 1, the leash angle of the simulated results is less than the measured values suggesting that the wind speed or drag coefficient are underestimated. Despite the discrepancies observed with the aerostat's motion in Figure 4.8, the resulting forces in the leash and the support tethers are similar for the simulation and experiment as seen in Figure 4.9.

Comparison of Simulated and Experimental Results in the Frequency Domain

The power spectra of the experimental and simulation results for leash tension, horizontal and vertical platform motion for Flight 3 are shown in Figure 4.10. For the two motion

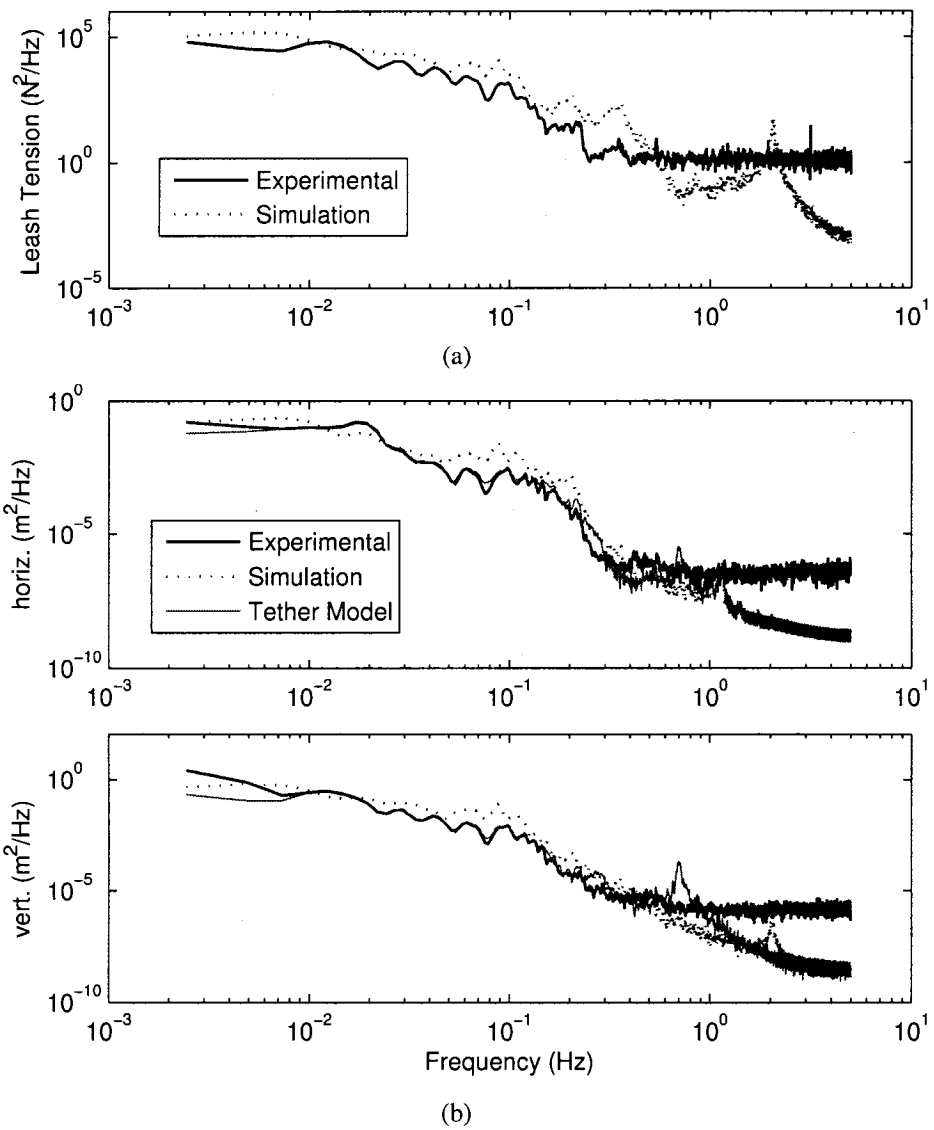

Figure 4.10: Power spectral density of simulation and experimental results; a) leash tension b) horizontal and vertical position (results are also included from Section 4.2.1 for the tether model).

plots, a third spectral density is given for the simulation results of the previous section using the measured leash force in place of the aerostat model. The simulated leash tension has a slightly larger magnitude over most of the bandwidth, but the similarity of the peaks through the midrange of frequencies indicates that the model captures most of the important modes affecting the leash tension. There is a noise floor for each of the measured quantities

that prevents comparison at high frequencies. However, the simulation appears to have some high frequency peaks that were not measured during the flight. The peak in the simulated leash tension at 2 Hz suggests that a particular oscillation is overemphasized in the model, but the magnitude is small enough that it is not expected to have much impact on the statistical validation in Table 4.4.

The results for the vertical motion of the tether model show excellent agreement with the experimental results, except at the lowest frequency and at a spike at about 0.7 Hz. The low frequency discrepancy is due to tether creep, observed in Figure 4.5, but the source of the spike at 0.7 Hz is not clear. The magnitude of the peak is small enough to not significantly affect the results as good statistical agreement between the tether model and the flight data can be seen in Figure 4.5 and Table 4.3.

In general, the discrepancies between the model predictions and experimental measurements observed in both the time and frequency domain are likely due to the imprecision involved with estimating the actual wind input. Because the wind model is based on measurements taken 150 m below the aerostat in only the horizontal direction, it is improbable that the extrapolated 3-D wind disturbance applied to the aerostat accurately matches the actual wind conditions. Lacking confidence in the wind model, it is difficult to reach definitive conclusions as to the quality of the aerostat model. Overall, the dynamics model for the passive system has been shown to agree satisfactorily with the experimental system at a statistical level. To further validate the aerostat model, more precise knowledge of the actual wind conditions near the aerostat is necessary.

4.3 Design Application

With a basic level of confidence established in the dynamics model for the tethered aerostat system, it becomes a powerful design and analysis tool. An analysis of one of the most crucial design parameters, the aerostat shape, is presented as an example of the model's proficiency as a design tool. Since nearly all the disturbances to the platform are due to the aerostat's aerodynamics, it is clear that its shape is an important design parameter.

	Streamlined	Spherical
Diameter (m)	7.7	10.15
Length (m)	18.4	10.15
Surface area (m^2)	495	324
Volume (m^2)	530	548
Mass (kg)	181	120
Net lift (kg)	299	375

Table 4.5: Physical properties of a streamlined and spherical aerostat.

Intuitively, a streamlined aerostat with minimal drag is the most attractive shape since its aerodynamic forces will have a smaller magnitude compared to bluff bodies such as a spherical aerostat. However, earlier simulation work of the LAR system has suggested that a spherical aerostat may have important advantages over a streamlined aerostat [3]. A thorough comparison of simulation results using the two types of aerostats was conducted with the goal of evaluating which class of aerostat is expected to lead to smaller platform motion of the LAR system.

4.3.1 Aerostat Comparison

The potential advantage of a spherical aerostat arises from its uniform frontal area in all directions. This means that its aerodynamic force consists strictly of drag, whereas an aerodynamic streamlined aerostat has the potential to generate lift as as well as drag at any non-zero pitch angle. This difference is significant with the LAR system because the response of the leash tension to turbulent wind gusts is what provides the input disturbance. The spherical aerostat will have a larger mean tension but its variance about that mean should be less, which could possibly lead to smaller deflections of the platform depending on the geometric configuration of the tethers.

Aerostat Specifications

The two aerostats that will be compared are fictitious and based on the estimated properties of aerostats produced by Aerostar International. The streamlined aerostat has the same dimensions as our aerostat, BOB, but it is lighter as Aerostat's proposed envelope material

is significantly lighter than BOB's envelope material. The physical properties of the two aerostats are presented in Table 4.5. The volume of the aerostats is similar (the spherical aerostat has 3% more volume because its dimensions were optimized for the aerostat hangar at DRAO), but the net lift of the spherical aerostat is 25% higher because of its lower mass. The aerodynamics for the streamlined aerostat are identical to what has been presented presented for BOB, but with a lower mass. The aerodynamics for the spherical aerostat are much simpler as its rotational degrees of freedom are neglected and only a single drag force is required, however, complexities arise when incorporating vortex shedding behaviour and estimating the drag coefficient for a tethered sphere.

4.3.2 Spherical Aerostat Aerodynamics

The original dynamics analysis of the LAR multi-tethered aerostat system performed by Nahon [2] included a spherical aerostat, but this model was incomplete as it did not consider known vortex shedding effects. Vortex shedding is a well-documented phenomenon affecting bodies with circular cross-sections such as cylinders and spheres. As vortices form downstream of the body, a transverse oscillatory motion is produced.

A direct method for incorporating vortex shedding behaviour into the dynamics model of a spherical aerostat is to add a transverse sinusoidal force to its motion equations [24]. The magnitude of the superimposed vortex shedding forcing function was determined by trial and error, i.e. for a specified oscillation amplitude and frequency, the magnitude of a sinusoidal force applied to the aerostat was adjusted until the desired amplitude was reached.

The magnitude of the expected vortex shedding oscillations are estimated based on experimental work by Govardham and Williamson [77] and Coulombe-Pontbriand [78] [79]. The study of Govardham and Williamson tested the vortex shedding motion of a tethered sphere over a range of controlled-flow conditions at relatively low Reynolds number $Re < 1.4 \times 10^4$. Coulombe-Pontbriand tested a spherical aerostat in open-air over a smaller range of conditions, but nearer to the Re of the flow conditions of our experimental system,

	1	2	3	4
Zenith angle, θ_{ze}(deg)	0	0	60	60
Azimuth angle, θ_{az}(deg)	-	-	60	60
Mean wind, U(m/s)	5	7	5	7

Table 4.6: Conditions for aerostat comparison simulations.

which is approximately $Re = 10^6$ at moderate wind conditions.

The approach for this analysis is to use both sets of results to obtain conservative estimates of vortex shedding behaviour. For instance, the amplitude of the vortex shedding oscillation of our spherical aerostat is based on data from Govardham and Williamson at low wind speeds, but at high wind speeds the proportional relationship between amplitude and wind speed observed by Coulombe-Pontbriand was applied (Govardham and Williamson observed a saturation of amplitude with wind speed). Coulombe-Pontbriand also found that the vortex shedding frequency did not increase with wind speed and instead remained near the natural pendulum frequency of the system. However in this analysis, the vortex shedding frequency increases slightly with wind wind speed as observed by Govardham and Williamson, since this should lead to more conservative modeling of the vortex shedding effects (higher frequency oscillations are a higher energy disturbance to the tethered system).

Both of these vortex shedding analysis also documented that the drag coefficient for a tethered sphere is significantly higher than for an ordinary fixed sphere due to the transverse oscillations observed only with the tethered sphere. Coulombe-Pontbriand presents an estimate of $C_{Dsph} = 0.55$ for supercritical flow, $Re > 3.5 \times 10^5$ while Govardham and Williamson estimate $C_{Dsph} = 0.65$ for the subcritical region $Re < 2 \times 10^5$. These results contrast the results found by Wieselsberger for a fixed sphere of approximately $C_{Dsph} = 0.4$ for subcritical Re and $C_{Dsph} = 0.15$ for supercritical Re [80]. The original spherical aerostat model for the LAR system used Wieselsberger's drag coefficient [2], but the current analysis uses the higher values determined for tethered spheres which experience vortex shedding.

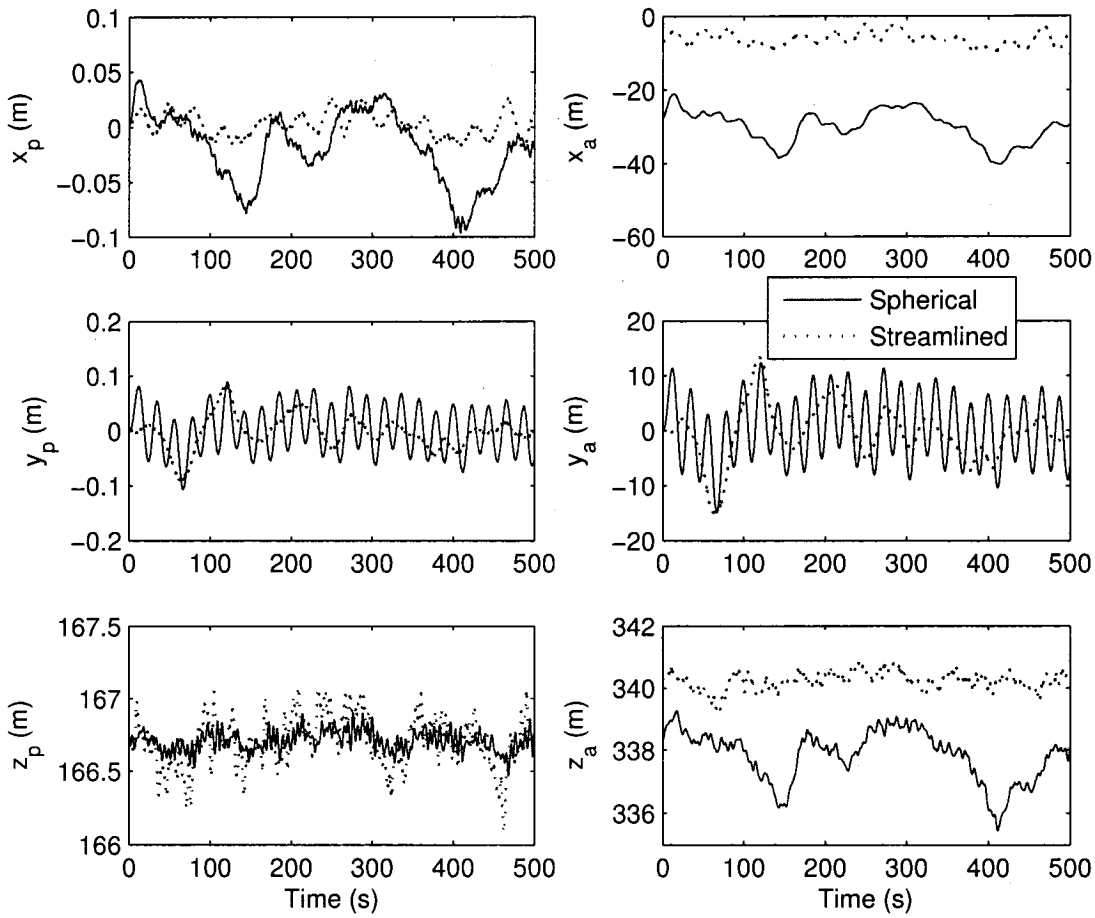

Figure 4.11: Simulation results for platform (left) and aerostat (right) for a spherical and streamlined aerostat for test case #1.

4.3.3 Results

Simulation results for four different test cases are used to compare the relative performance of the aerostats. The cases include two different geometrical configurations at two different wind speeds as summarized in Table 4.6. The two geometries represent the best case, $\theta_{ze} = 0°$ and the worst case at the maximum zenith angle, $\theta_{ze} = 60°$ and an azimuth angle $\theta_{az} = 60°$ (worst case geometry found by trial and error). The two wind speeds, $U = 5$ m/s and 7 m/s represent respectively typical and maximum operating conditions.

Results of the comparison for test case #1 are presented in Figure 4.11 for the position of the platform and aerostat and Figure 4.12 for the tether tension. The vortex shedding

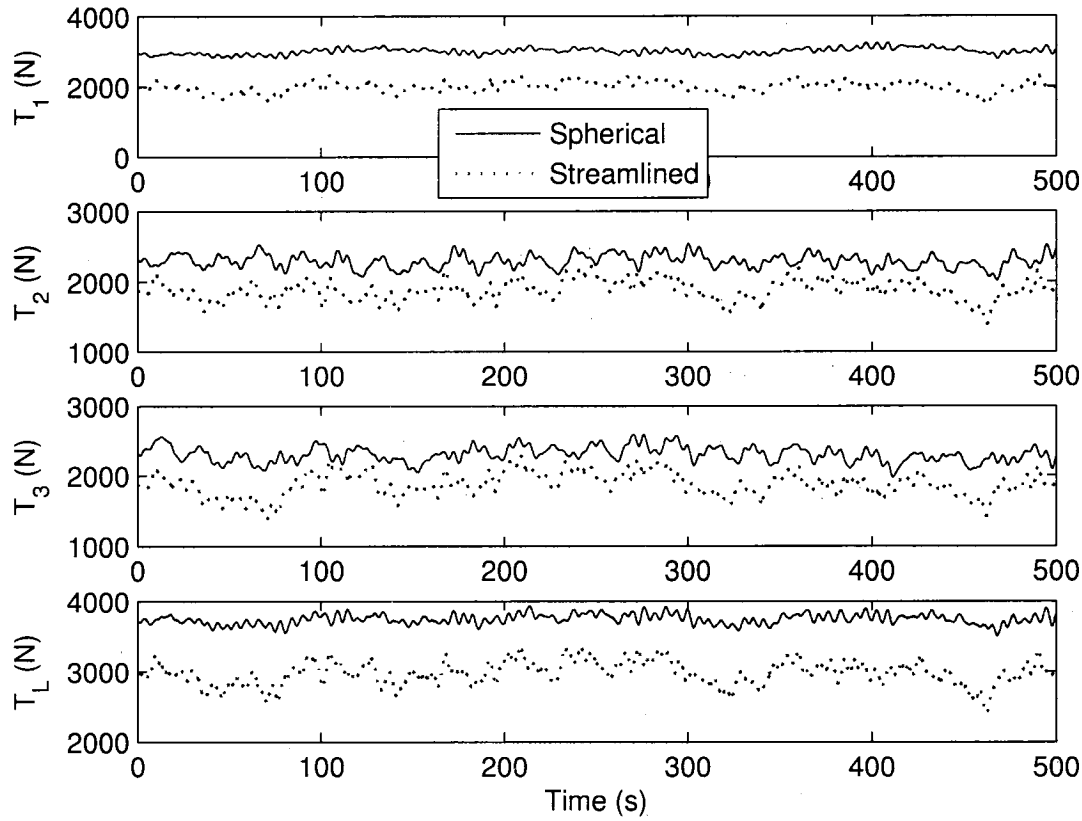

Figure 4.12: Simulation results for tether tension for a spherical and streamlined aerostat for test case #1.

oscillation is clearly observed in the y-direction of the spherical aerostat. The high drag of the spherical aerostat is apparent by its position in the x-direction (wind angle was 180° or in the negative x-direction) as well as in larger tether tensions. However, the fluctuations about the mean tether-tensions appear to be smaller with the spherical aerostat. The overall performance of the system is quantified by the magnitude of the resulting platform motion; for the streamlined aerostat the motion is smaller in the two horizontal directions but larger in the vertical direction.

A summary of the results for the four test cases is provided in Table 4.7. The general trends observed for case #1 in Figures 4.11 and 4.12 are consistent with the three other cases as the horizontal deviations of the platform are less with the streamlined aerostat while the vertical deviation is less with the spherical aerostat. However, the magnitude of

Parameter		#1		#2		#3		#4	
		Sph.	Str.	Sph.	Str.	Sph.	Str.	Sph.	Str
Platform	σ_x	0.032	0.011	0.052	0.023	0.039	0.031	0.051	0.044
Position	σ_y	0.042	0.030	0.054	0.038	0.061	0.055	0.078	0.079
(m)	σ_z	0.07	0.18	0.12	0.33	0.15	0.38	0.31	0.66
	T_L	3742	2974	3880	3068	3730	2964	3846	3032
	T_1	3006	1991	3389	2220	6008	4336	6281	4511
Tether	T_2	2292	1879	2089	1858	5395	4239	5097	4317
Tension	T_3	2301	1873	2103	1992	1794	1343	1793	1388
(N)	σ_{T_L}	71	127	141	313	56	134	120	233
	σ_{T_1}	93	160	164	274	115	146	232	433
	σ_{T_2}	97	139	153	266	116	243	219	425
	σ_{T_3}	113	167	176	298	113	115	154	175

Table 4.7: Comparison of simulated results for a spherical and streamlined aerostat.

the vertical motion is much greater than the horizontal motion, and thus, the corresponding advantage of the spherical aerostat vertically is much greater than the horizontal advantage with the streamlined aerostat (tens of cm opposed to tens of mm). Also favourable for the spherical aerostat is that its larger magnitude horizontal deflections are relatively low frequency and thus, should be manageable with a control system.

The distinct response to turbulent wind gusts is the cause for the divergent performance between the two aerostats. The spherical aerostat, as already mentioned, is characterized by a single drag force and therefore it only generates aerodynamic force in the direction of a wind gust. In contrast, the streamlined aerostat generates lift as well as drag when its angle of attack is non-zero. This causes the standard deviation of the leash tension to potentially be greater for the streamlined aerostat when it has non-zero pitch or is exposed to multi-directional gusts. Furthermore, because the leash is near vertical and the tether structure has lower stiffness in the vertical direction, the system is more sensitive to the streamlined aerostat's mostly vertical perturbations than the spherical aerostat's perturbations which have a smaller vertical component.

At high wind speeds (cases 2 and 4), it is interesting to note that the tension in certain tethers increases while in others it decreases. For example, with case #2 at $U = 7$ m/s the tension in tether 1 is higher than in case #1 with $U = 5$ m/s, while the tension in both

tether 2 and 3 is lower. The wind direction is along tether 1 and hence it becomes tighter with more wind, and the other two tethers, which are angled into the wind, see a reduced tension. This effect is more pronounced with the spherical aerostat as it has a larger drag force, and the effect would be much more profound at even higher wind speeds when the spherical aerostat's blowdown angle increases. The performance of the system degrades significantly when the tension in any tether drops below a certain threshold and becomes somewhat slack. Poor performance was observed with the experimental system on March 23 when the mean tension in tether 3 was only 173 N (Table 4.2), but the actual threshold for a slack tether is expected to be near 600 N or 700 N depending on the specific tether geometry. The aerostats compared in this section were selected to have enough excess lift so that none of the tethers experiences slack tether conditions during normal operations, but it is understood that at wind speeds beyond the operational limit of the LAR system, the system would be much more susceptible to a slack tether with a spherical aerostat.

The minimum tether load is important when considering performance related to slack tethers, while the maximum tether load is important when considering the system design and safety. The maximum tether loading during the four test cases occurred during case #4, which is expected since the tether geometry is asymmetric and it is a high wind case. For the spherical aerostat the maximum tension was 6940 N and for the streamlined aerostat it was 5480 N. The ultimate load for the 6-mm *Plasma* tethers used with the experimental system is 35.6 kN [59], which results in a safety factor of 5.1 for the sphere and 6.5 for the streamlined aerostat. The experimental system was designed with a safety factor of 5, thus, either aerostat would meet the design criteria. However, the wind speed $U = 7$ m/s is only the operational limit of the proposed LAR telescope, and the telescope must be prepared to encounter more excessive winds. Therefore, for the detailed design of the actual telescope, the effects of higher wind speeds on tether loading must be considered in greater detail.

Apart from the tether loads and the confluence platform motion, there are several logistical factors to consider when evaluating an aerostat for the LAR system, including details related to launching, retrieving and storing the aerostat. However, within the context of the

current work, the purpose of the comparison was to investigate and contrast the dynamics behaviour of the tri-tethered system with a spherical aerostat and a streamlined aerostat. Through simulation results it was demonstrated that the spherical aerostat, despite its high drag and vortex shedding behaviour, outperforms a streamlined aerostat in terms of minimizing platform motion.

Chapter 5

Controlled Response of System

During the spring of 2005, the second phase of testing of the tri-tethered aerostat system at DRAO was conducted. This phase involved tether actuation with active winches. Like the previous chapter, this chapter is divided into three distinct themes: first the experimental results are presented to demonstrate the performance of the positioning system, now operating with control system input, next the model results will be compared to the measurements to ascertain and validate the model's accuracy, and finally a design application will be presented where design parameters such as the the number of tethers and the base radius are examined.

5.1 Controlled Flight Tests

Several challenges related to winch communication and power were encountered while transitioning the test facility from a passive to active system. Because of the large distances of the SERCOS loop that connects the winches in series (Figure 2.9), long runs (> 500 m) of fiber-optic cables were required. Initially the cables were placed above ground inside conduit piping but after several line failures, more robust fiber-optic cables were purchased and buried below ground. The winches also required connection to high voltage power lines which were also buried. The initial layout for the winches called for placement on a circle with a radius, $R_B = 400$ m, but the location of the power lines limited the actual radius to $R_B = 364$ m. This difference should not have a significant effect on the experi-

mental results. Strict dynamic similarity to the full-scale LAR system is compromised and thus any results are not directly scalable, but the validation of the dynamics model is not affected as the geometry of the model is adjusted to match the experiment. The workspace of the positioning system is reduced by the smaller base radius, and therefore the maximum zenith angle tested is $\theta_{ze} = 50°$ instead of $\theta_{ze} = 60°$.

With the passive elements of the dynamics model validated in the previous chapter, the incremental validation of the model continues with first a comparison to the open-loop response of the experimental system, followed by a comparison of the total model with measurements obtained during closed-loop control. The initial tests conducted at DRAO with functioning winches were with open-loop control; a specific command was sent to a winch and the system's response was measured. For the second round of flights, feedback control was implemented to regulate the platform position about a fixed point using the PID algorithm described in Section 3.5. The closed-loop experimental results will initially be presented on their own to demonstrate the effectiveness of the positioning system. This will be followed by comparisons to the closed-loop behaviour predicted by the simulation.

5.2 Controlled Results and Model Validation

The first stage of validating the complete dynamics model of the multi-tethered aerostat system, based on passive tethers with fixed lengths, gave encouraging results, however, there was a certain level of imprecision due to uncertainty in recreating the precise wind input. To validate the dynamic actuation of the tethered system, it was decided to remove as much of the wind model uncertainty as possible. This was achieved first by analyzing the open-loop performance of the complete system in calm conditions, thus minimizing the influence of the wind, and second by simulating the closed-loop response of the model with the aerostat aerodynamics replaced by the actual measured leash force.

5.2.1 Open-loop

A convenient approach to assessing the model of the tether actuators is to compare its open-loop response to that of the experimental system. The platform position in response to open-loop sinusoidal winch inputs was measured on four separate flights. Each flight was conducted in the early morning to ensure wind disturbances would be minimal (the measured wind speed at the platform was less than 1 m/s).

To facilitate the open-loop comparison, the dynamics model was linearized using the numerical techniques of Section 3.8 to generate the magnitude and phase relationship between winch inputs and platform position outputs over a range of frequencies, known as a Bode diagram. The resulting Bode diagram from the linear model can be directly compared to approximate Bode plot for the experimental results obtained using open-loop flight data. Figure 5.1 gives separate Bode plots for each of the three Cartesian coordinates of the inertial frame. The input to the system is a sinusoidal length change in tether #1 and the system is in the symmetric configuration, $\theta_{ze} = 0°$. Due to acceleration limits of the winch motors, the highest frequency tested was 2.5 Hz. For the high frequency tests, particularly in the z-direction, it was not possible to estimate the phase angle satisfactorily as the motion was of small magnitude and corrupted by noise.

The results in Figure 5.1 show a good match between the linear model and the measured frequency response. The general shape and the main features of the Bode plot are present in both sets of results. The main peak of the linear model for the magnitude of the x and y horizontal directions may be shifted slightly toward lower frequencies, but they appear to have the appropriate magnitude.

In the vertical direction, there is good agreement at low frequencies but the results diverge at higher frequencies. For most of the divergence region, the magnitudes are quite low, so the discrepancy could be attributed to insufficient measurement resolution. However, even if it is a real discrepancy in the model, the magnitude is low enough that it will not degrade the results. The exception is the peak at 2 Hz, which crosses the 0-dB line. The response at this frequency appears to be overstated in the model and as a result, the vertical

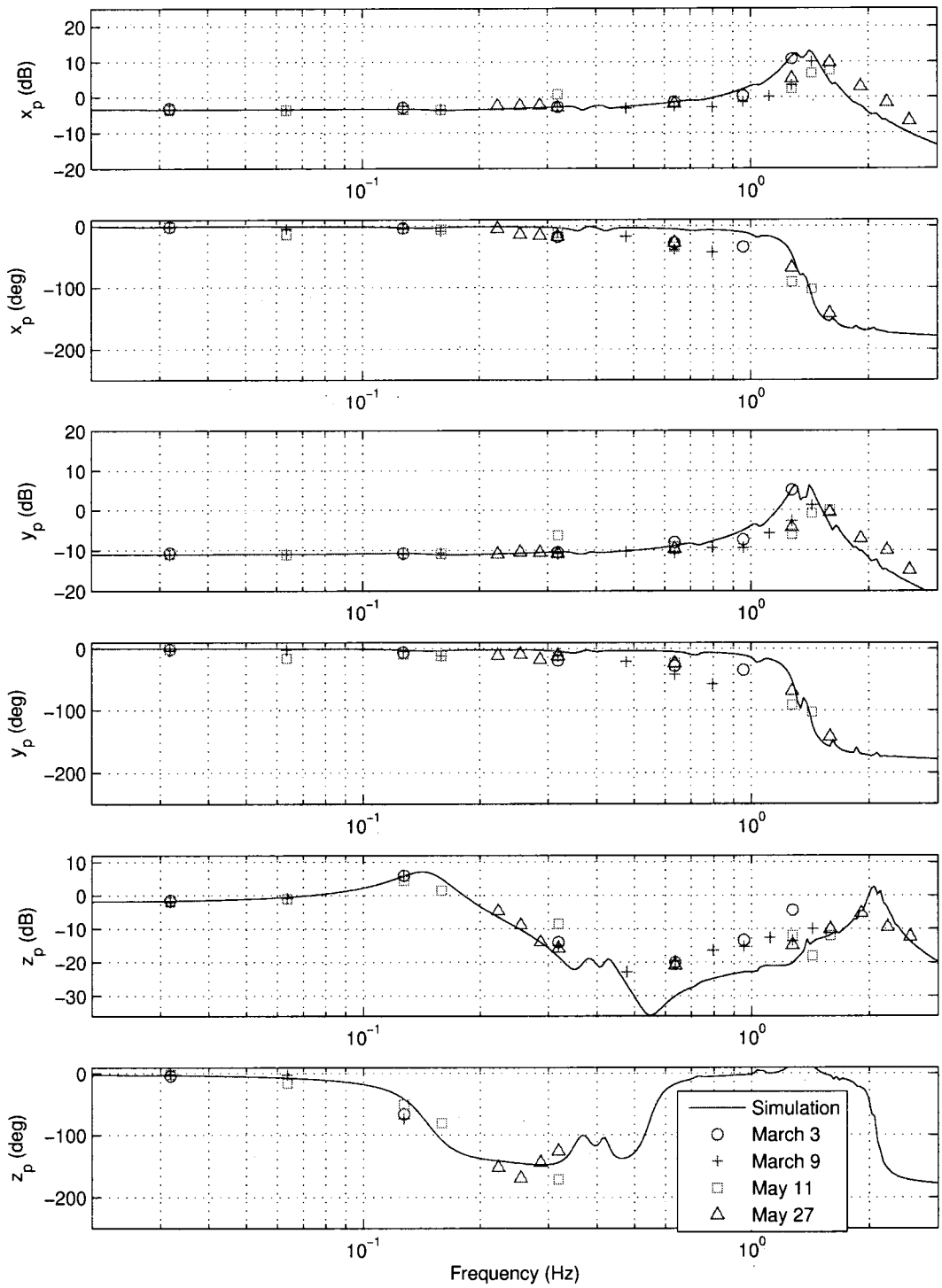

Figure 5.1: Bode plot comparison of simulated and experimental payload position in response to input at winch #1 with $\theta_{ze} = 0°$.

		zenith, $\theta_{ze} = 0°$		zenith, $\theta_{ze} = 30°$		zenith, $\theta_{ze} = 50°$	
Control		No	Yes	No	Yes	No	Yes
# of trials		5	5	2	2	3	3
Wind (m/s)	U	3.37	2.35	2.43	2.34	3.51	2.44
Turb. intensity	σ_U/U	0.16	0.21	0.42	0.32	0.24	0.23
Aerostat	σ_x	2.41	1.97	2.54	3.06	3.36	2.88
Position	σ_y	4.97	5.62	4.88	4.17	5.24	4.75
(m)	σ_z	0.23	0.26	0.29	0.19	0.31	0.18
Platform	σ_x	0.016	0.004	0.042	0.013	0.074	0.038
Position	σ_y	0.030	0.010	0.035	0.012	0.063	0.031
(m)	σ_z	0.113	0.062	0.138	0.076	0.24	0.084
Reduction(%)	σ_x	-	63	-	69	-	49
Reduction(%)	σ_y	-	68	-	54	-	51
Reduction(%)	σ_z	-	45	-	45	-	65

Table 5.1: Summary of experimental results with and without control at three different configurations.

motion in the simulation may have a larger amplitude at this frequency (as observed in Figure 4.10). The lower frequency region of the Bode plots is far more critical when assessing the quality of the simulation as the bulk of the input forces are low frequency due to the substantial size of the system. During the closed-loop test flights, the peak in the vertical magnitude near 0.15 Hz has been observed to dominate the overall motion of the platform and was shown to become unstable with high gains (Figure 5.4). Based on open-loop test data near this frequency, which shows a peak near 0.13 Hz in the vertical Bode plot of the magnitude, it appears that a vertical bounce at a similar frequency is prominent during both closed-loop and open-loop operation. Figure 5.1 shows that both the amplitude and phase of this open-loop bounce mode is characterized well by the linear model relative to the experiments.

5.2.2 Closed-Loop Test Results

A summary of the results during 10 controlled and uncontrolled trials is presented in Table 5.1. Three different zenith angles were tested: $\theta_{ze} = 0°$ (symmetric configuration), $\theta_{ze} = 30°$, and $\theta_{ze} = 50°$ (edge of the workspace for the experimental system with $R_B = 364$ m). The results in Table 5.1 are averaged values over the several trials at

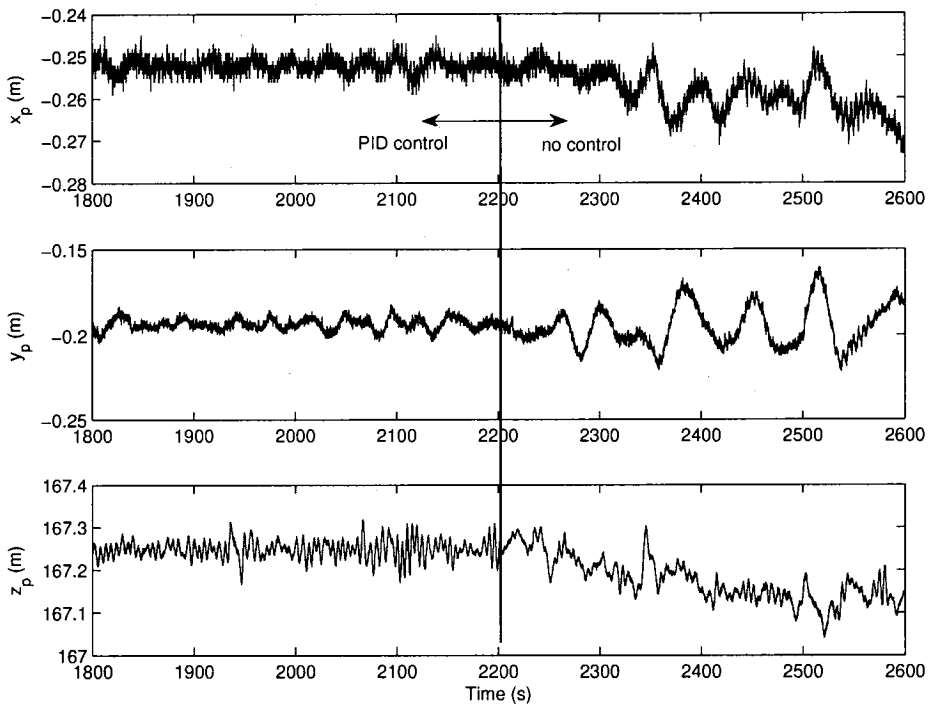

Figure 5.2: Experimental results for platform position during May 6 test with and without PID control at $\theta_{ze} = 0°$.

each zenith angle. The effectiveness of the closed-loop winch control is clearly demonstrated as the platform deviation for each case is smaller with the control active than with no control. This result may seem intuitive as feedback control is routinely used to improve performance of mechanical systems, however, the large dimensions of the system, which employs tether actuators half-a-kilometer long controlled by winches located hundreds of meters away from the position sensor, and the low control-bandwidth (10 Hz) introduces considerable challenges to the controller's overall effectiveness.

The percentage reduction between the controlled and uncontrolled standard deviation of the platform motion, also included in Table 5.1, ranges from 45% to 69%. The reduction at each of the three zenith angles tested are comparable in terms of percent, but the magnitude of the motion clearly increases with zenith angle.

Figure 5.2 shows the platform positioning during a flight on May 6, 2005, which visually demonstrates the effectiveness of the controller. A PID controller with gains

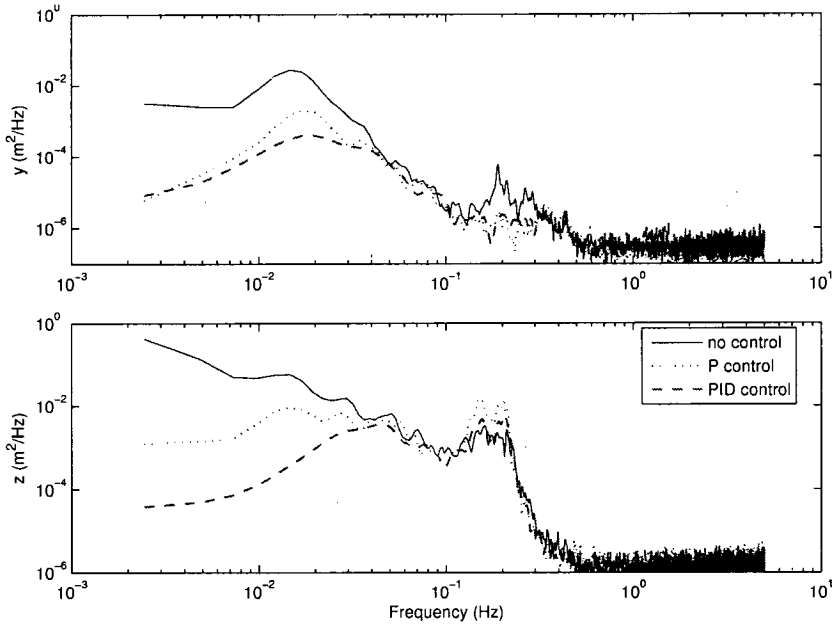

Figure 5.3: Power spectral density of platform position during May 6 test at $\theta_{ze} = 0°$.

$K_P = 0.3$ s^{-1}, $K_I = 0.05$ s^{-2}, and $K_D = 0.05$, was used for the first portion of the tests and at $t = 2200$ s, the winch control was turned off and the tether lengths were fixed. The gains were manually tuned at the start of the testing period. The low frequency motion is clearly reduced while the controller is active, but in the vertical direction, high frequency vibrations appear to have a slightly higher amplitude with control. This is confirmed by examining the performance of the controller across the frequency spectrum. The PSD of the May 6 results are given in Figure 5.3; results are presented for a third proportional-only ($K_P = 0.3$ s^{-1}) controller as well as the PID control and no control cases from Figure 5.2. The PSD in the x-direction was omitted since it was similar to the plot in the y-direction. The proficiency of the controller at reducing platform motion at low frequencies is confirmed in the PSD plots, but the bandwidth of effectiveness varies between the horizontal and vertical directions. Horizontally, the controller is effective up to 0.3 Hz, while vertically it appears to only be effective up to 0.05 Hz.

The high frequency vertical oscillations observed in Figure 5.2, which appear to be larger with the feedback controller, correspond to the peaks near 0.2 Hz in the PSD plot.

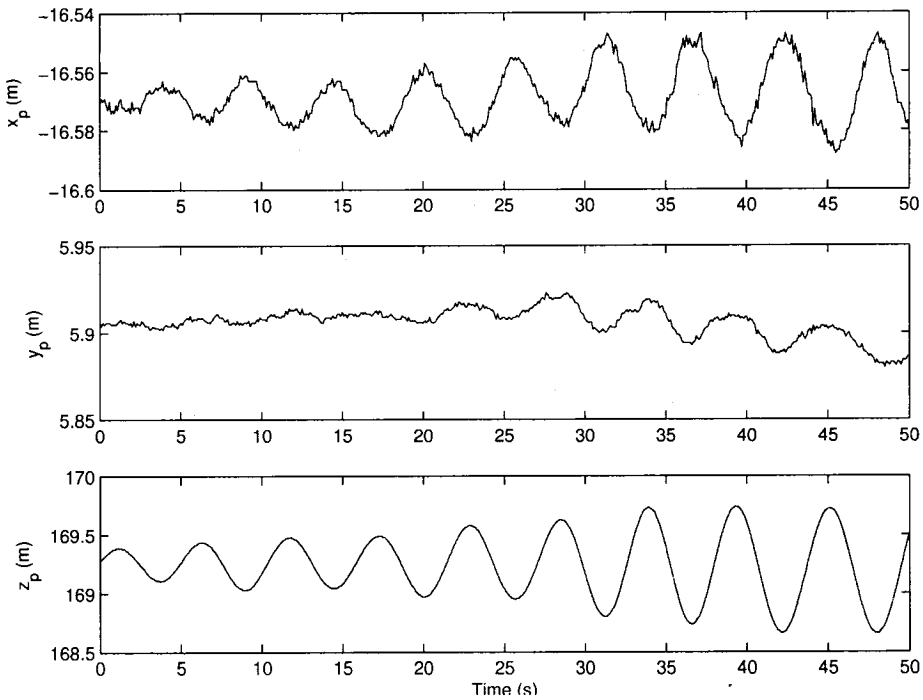

Figure 5.4: Platform position during instability on March 22 with $K_P = 0.75$ s^{-1}.

Indeed, the controller appears to amplify the response near this frequency, which suggests that one or more vertical modes of the closed-loop system are susceptible to excitations. This vertical *bounce* mode near 0.2 Hz was observed to lead to instabilities if the feedback gains were too high. For example, the proportional gain for the test shown in Figure 5.4 was turned up to $K_P = 0.75$ s^{-1}, and the vertical bounce mode was observed to grow until it exceeded 1 m and the controller was powered down.

Results for the PSD of a high zenith case $\theta_{ze} = 50°$, are provided in Figure 5.5. For this test, the controller had only a proportional gain, $K_P = 0.4$ s^{-1}. At the high zenith angle the controller is also effective at low frequencies ($< 0.05\ Hz$) while exciting the system and adding energy near 0.1 Hz. A notable difference in Figure 5.5 compared to its low zenith counterpart in Figure 5.3 is in the midrange frequencies (0.04 Hz to 0.1 Hz) of the y-direction, where the amplitudes in Figure 5.5 do not drop off until 0.1 Hz. Because the large amplitude motion extends past the effective controller bandwidth, the horizontal motion at $\theta_{ze} = 50°$ is much greater than at $\theta_{ze} = 0°$. This was also observed in Table 5.1

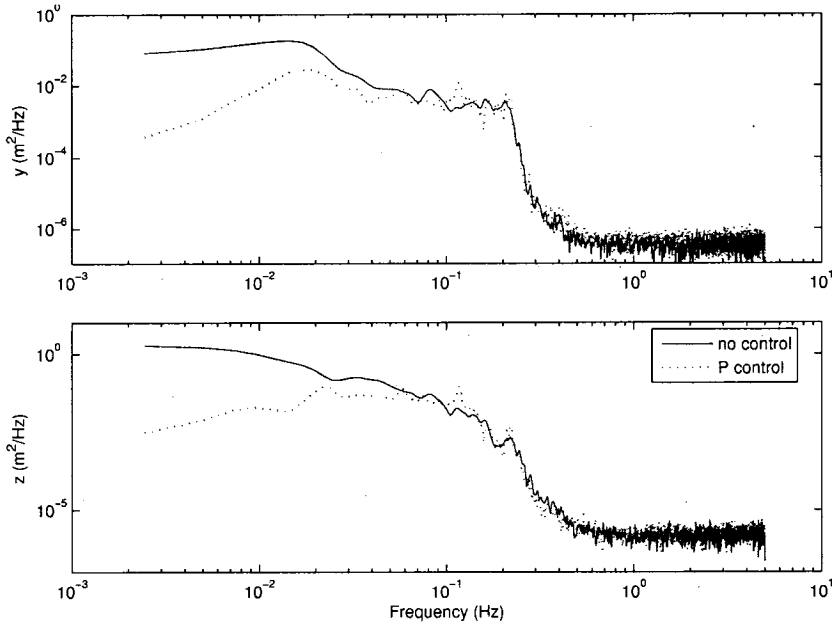

Figure 5.5: Power spectral density of platform position during May 27 test at $\theta_{ze} = 50°$.

where the horizontal deviation at $\theta_{ze} = 50°$ was several times greater than the deviation at $\theta_{ze} = 0°$, while the vertical deviations were of comparable magnitudes.

Overall, the closed-loop results are encouraging from the perspective of the LAR telescope as the approximate design goal of 17 cm RMS platform error for the scaled system is exceeded during the experimental trials, which produced RMS errors of less than 10 cm. It is possible that a PID controller with optimally tuned integral and derivative gains could improve on the test results performed thus far; however, the inability of the PID controller to improve the response past 0.05 Hz and its contributions to the problematic vertical bounce mode suggest that a more sophisticated controller is necessary to further improve the performance of the positioning system. Once the dynamics model for the entire closed-loop system is validated in the remaining sections of this chapter, the model will be used in Chapter 6 to develop and evaluate advanced controllers that outperform the basic PID controller.

5.2.3 Closed-loop Validation

The model of the feedback control system can be validated by comparing simulation and experimental output with matching input disturbances. This procedure assumes that the majority of the disturbances are generated by the aerodynamic forces on the aerostat and transmitted to the platform through the leash, which was confirmed in Section 4.2.1.

The results from two specific flights will be used to validate the dynamics model and clearly demonstrate the effectiveness of the actual control system. The flights correspond to the two configurations examined in Figures 5.3 and 5.5 at zenith angles $\theta_{ze} = 0°$ and $\theta_{ze} = 50°$ respectively. During the tests flights at each configuration, two separate trials were performed; the first is with the feedback control activated and the second is with no control. The two trials for the first flight at $\theta_{ze} = 0°$ are labeled as A (with control) and B (without control) and the two trials for the second flight $\theta_{ze} = 50°$ are labeled as C (with control) and D (without control).

The experimental results for each trial are presented along with two sets of simulation results, one with the same control scheme tested during that trial and one with the opposite control scheme (if a controller was tested, the opposite scheme is with no controller and vice versa). With matching control, a comparison of the simulated and experimental results appraises the accuracy of the model predictions, while the results with the opposite control scheme provide an estimation of the effectiveness of the actual control system. For the experiments with control, the simulated results without control provide a benchmark to quantify how much improvement can be attributed to the controller. For the experiments without control, the simulated results with control provide a prediction of how much the controller might have changed the results had it been active. This approach to controller evaluation assumes that the aerostat's response to control inputs is relatively small compared to its response to the wind input (an assumption that is qualified in Section 6.2).

The results for the four trials are summarized in Tables 5.2 and 5.3 and plotted in Figures 5.6 to 5.9. The tables include the standard deviation of the platform position and the mean and standard deviation of the tether tension. Only tensions in tethers #1 and #3 are

		Trial A, $U = 1.2$ m/s			Trial B, $U = 0.9$ m/s		
Control		Yes	Yes	No	No	No	Yes
Type		Exp.	Sim.	Sim.	Exp.	Sim.	Sim.
Platform	σ_x	0.002	0.001	0.003	0.005	0.005	0.002
Position	σ_y	0.003	0.004	0.011	0.012	0.014	0.004
(m)	σ_z	0.022	0.027	0.054	0.053	0.067	0.026
	T_1	1495	1415	1415	1489	1424	1424
Tether	σ_{T_1}	36	37	37	47	48	48
Tension (N)	T_3	1312	1328	1328	1296	1300	1299
	σ_{T_3}	36	37	36	49	52	52

Table 5.2: Comparison of experimental and simulated results at $\theta_{ze} = 0°$ with control (A) and without (B) for tests on May 6, 2005. The PID gains used were $K_P = 0.3$ s^{-1}, $K_I = 0.05$ s^{-2}, and $K_D = 0.05$.

		Trial C, $U = 4.0$ m/s			Trial D, $U = 3.8$ m/s		
Control		Yes	Yes	No	No	No	Yes
Type		Exp.	Sim.	Sim.	Exp.	Sim.	Sim.
Platform	σ_x	0.056	0.043	0.082	0.073	0.072	0.036
Position	σ_y	0.046	0.036	0.077	0.064	0.065	0.030
(m)	σ_z	0.092	0.107	0.215	0.156	0.184	0.084
	T_1	2160	2170	2171	2241	2264	2262
Tether	σ_{T_1}	136	141	138	112	117	119
Tension (N)	T_3	492	529	531	516	538	536
	σ_{T_3}	55	54	52	42	44	46

Table 5.3: Comparison of experimental and simulated results at $\theta_{ze} = 50°$ with control (C) and without (D) for tests on May 27, 2005. The PID gains used were $K_P = 0.4$ s^{-1}, $K_I = K_D = 0$.

reported as the load cell for tether #2 malfunctioned during the tests. The x, y, z-position of the platform is plotted against time and the power spectral density of the position in the x and z directions are included in the figures (the PSD of y was omitted as it strongly resembles the PSD of x).

The simulation results with the matching control schemes correspond well to the experiments for all four trials, but the agreement is clearly better for the trials A and B with the system in the symmetric configuration. There is substantial noise with the GPS measurements, which is most noticeable in the x-direction of Figure 5.6 for trial A, where the motion was small. The presence of noise is also apparent in the experimental PSD plots as

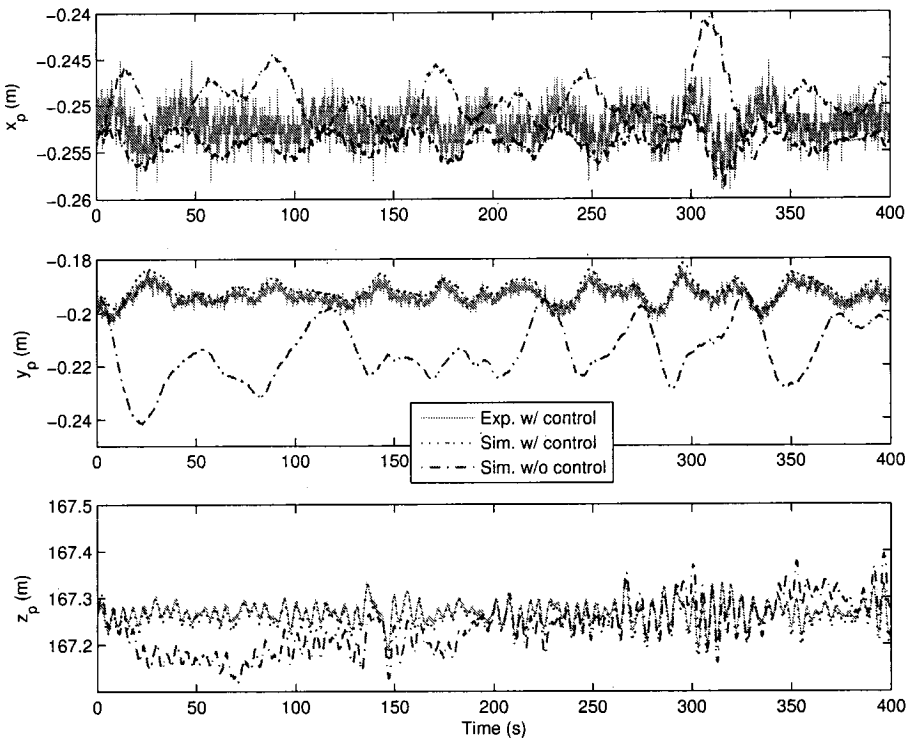

(a)

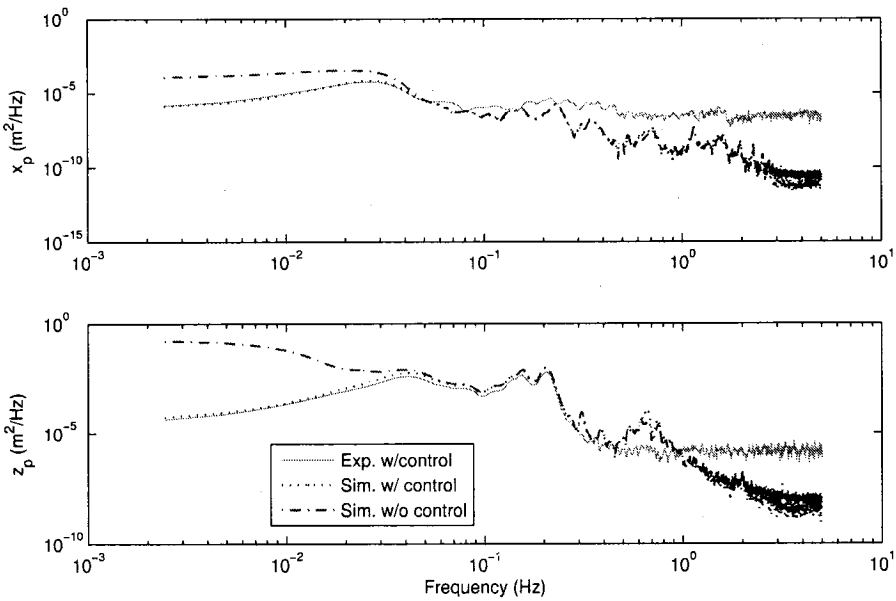

(b)

Figure 5.6: Comparison of experimental and simulated results for platform position for trial A, a) time history, b) PSD.

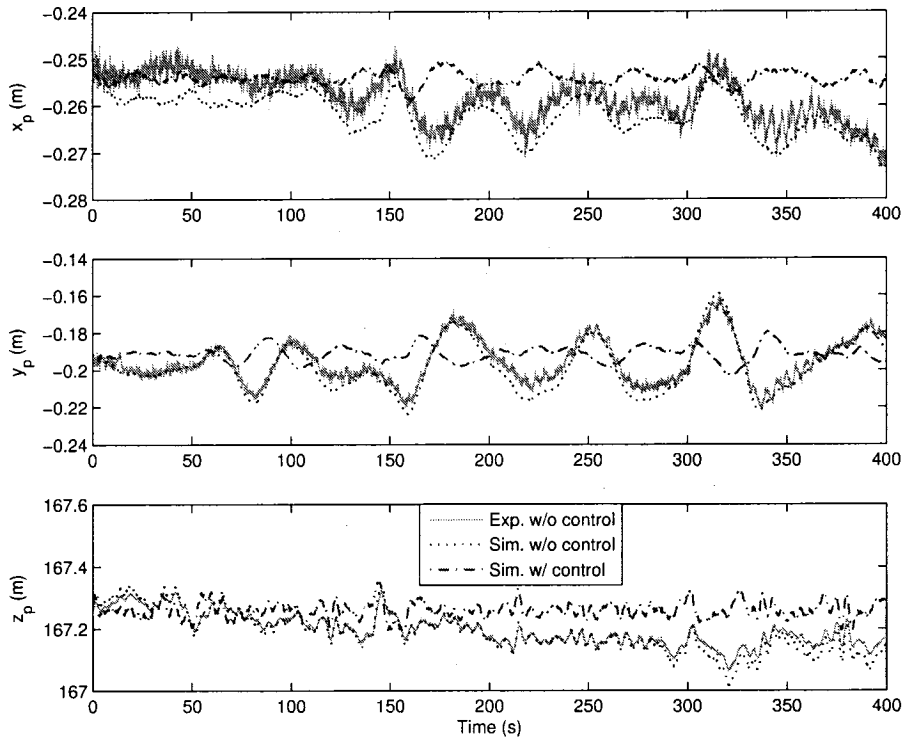

(a)

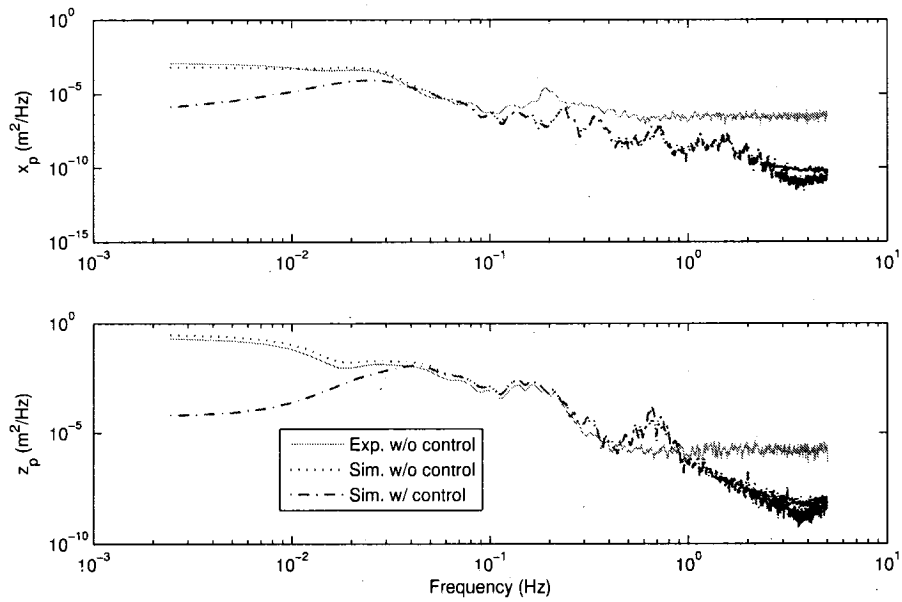

(b)

Figure 5.7: Comparison of experimental and simulated results for platform position for trial B, a) time history, b) PSD.

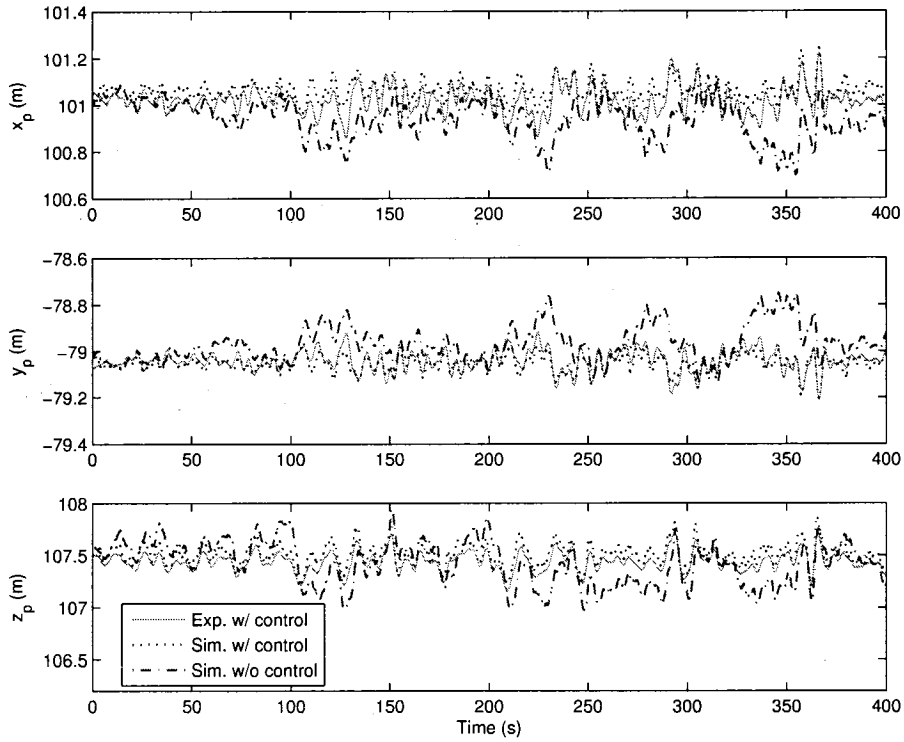

(a)

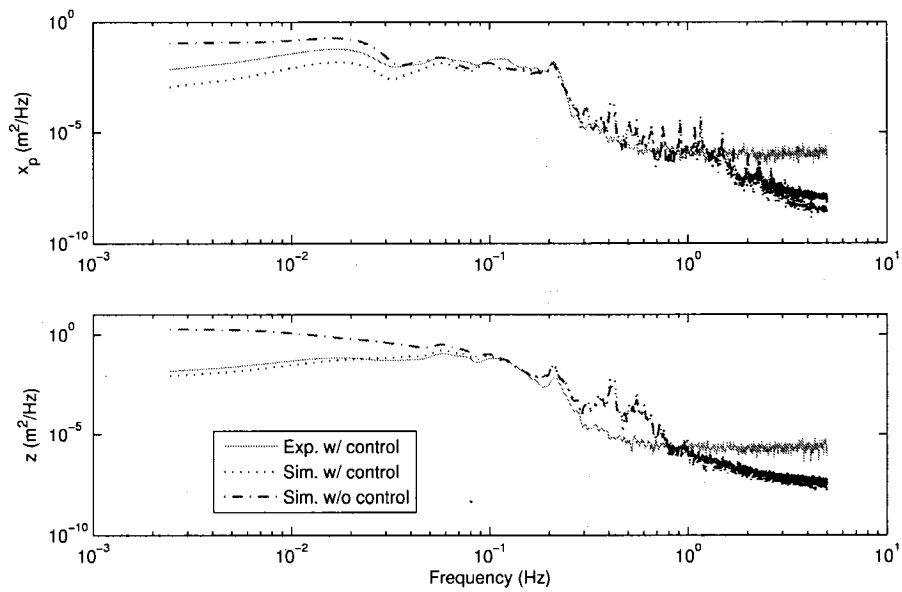

(b)

Figure 5.8: Comparison of experimental and simulated results for platform position for trial C, a) time history, b) PSD.

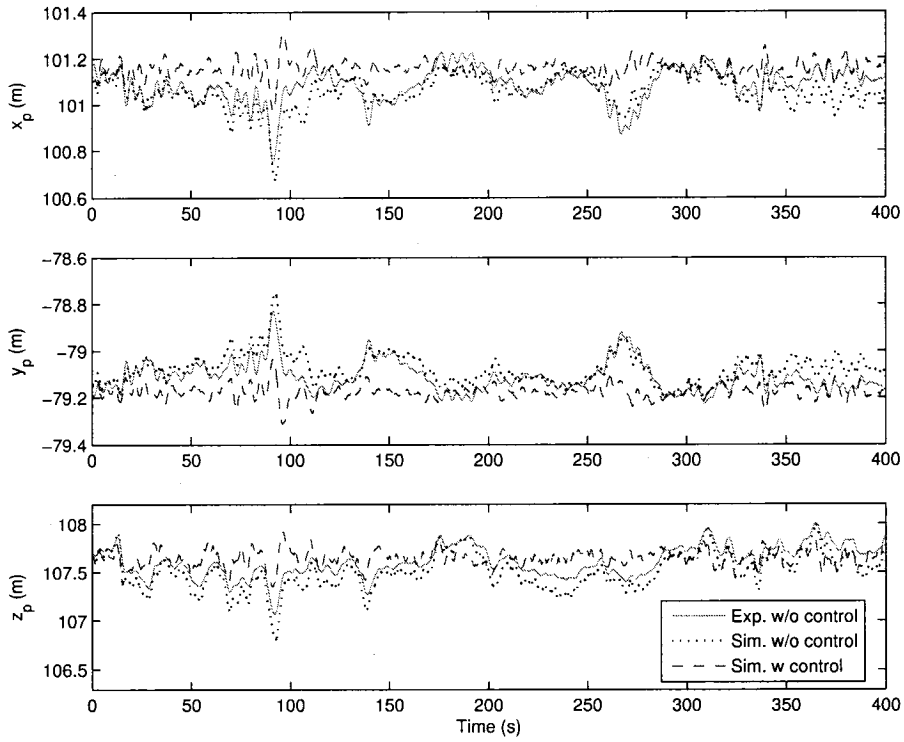

(a)

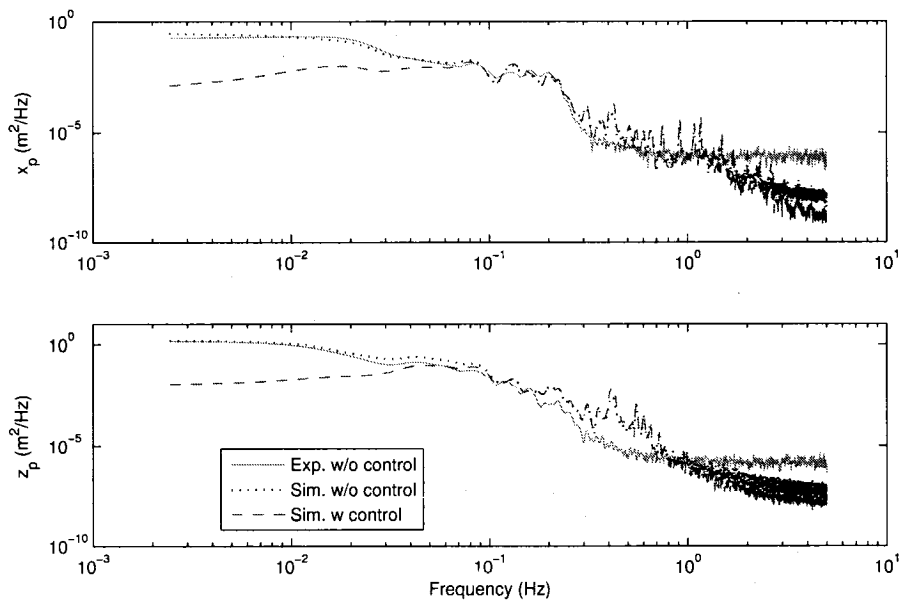

(b)

Figure 5.9: Comparison of experimental and simulated results for platform position for trial D, a) time history, b) PSD.

a flattening of the curves is observed at high frequencies. Despite the measurement noise, it is observed that the simulation clearly predicts the low frequency motion accurately which can be seen in both the time histories and the PSD plots. It should be noted that any difference in the mean value of the positions is not significant as it is due to inexact initial conditions. The simulation starts from a static equilibrium position whereas at $t = 0$ of the measurements, the actual system has dynamic motion.

For trial A, the standard deviation of the simulated vertical motion is within 5 mm of the measured motion and the difference between the horizontal deviations is less than 1 mm. For trial B, the system is uncontrolled and the difference between the simulation and experiment is 14 mm vertically and less than 5 mm horizontally. Considering the scale of the system, the accuracy of simulation strongly validates the tether model. The passive or unactuated lumped-mass tether model was previously validated in Chapter 4 and in prior studies [43] [44], but this work represents the first experimental validation of the actuated or length-varying lumped-mass tether described by Kamman [39] and Nahon [2]. The good agreement with the experimental results suggests that the parameter-varying discretization method is suitable for long actuated tethers.

During trial B, a horizontal oscillation at 0.2 Hz was measured that cannot be attributed to sensor noise. The oscillation does not show up in the simulation results, which can be seen toward the end of the time histories and in the PSD with the missing peak at 0.2 Hz. It is difficult to ascertain what is causing the oscillation, but it does not appear to originate from the disturbance force transmitted through the leash. The slack central tether used during deployment and retrieval, which is attached to the tether confluence point, is not included in our dynamics model and it is possible that it can have a small impact on the platform motion. Because the magnitude of the oscillation is relatively small (about 1 cm) and the simulation accurately predicts the higher-amplitude low-frequency motion, the results are deemed satisfactory.

The simulation results for the high zenith case, trials C and D in Figures 5.8 and 5.9, do not match the measurements as well as at the previous trials at the zenith. The general

characteristics of the motion are predicted well, as observed by the similarity in the PSD plots, but the amplitude of the oscillations are not always accurate, which is observed in the time histories and the statistics in Table 5.3. One explanation for the reduced accuracy of the simulation at high zenith angles is that in this configuration the system is less stiff and therefore more sensitive to estimation errors. The system loses stiffness as the three tethers become asymmetric because the tension in at least one tether inevitably drops. For the configuration tested in trials C and D, the tension in tether 3 drops substantially below the other two. The stiffness of an individual tether can depend greatly on its tensile load as the amount of sag in the tether profile drastically affects its stiffness. Therefore, at the high zenith configuration, any errors in the tension distribution among the tethers in the model will result in greater discrepancies than for the symmetric case at the zenith. This is confirmed by the results of trials A and B, as the simulated mean tether tensions differed from the measured tensions by larger amounts than in trials C and D, while still producing excellent agreement in the motion (discrepancy in the standard deviation $\leq$ 15 mm in each direction for the platform position). Although the mean tensions have a DC error, the standard deviation of the tensions are similar indicating the disturbing functions were similar.

The imprecision in the model's distribution of forces to the three support tethers could be caused by assuming that all three tethers and the leash meet at a single point-mass or node at the confluence point. The entire platform weight and the associated weight of the slack central tether are applied to this node whereas in the real system the weight of the platform and the central leash are likely to be distributed unequally to the three tethers. Despite the discrepancy in mean tether loading and its implications at the high zenith angle, the simulation has proven effective at predicting the response of the system with and without a controller.

With the first set of simulation results verifying the reliability of the model, the second set of simulation results can be utilized to confirm further the effectiveness of the controller. This approach is more direct than comparing the two separate time histories of the motion

that were exposed inevitably to different wind disturbances as in Section 5.2.2. The dash-dot lines in Figures 5.6 to 5.9 show the predicted response of the system if the opposite control scheme would have been used. It is clear that the controller is very effective at limiting low frequency motion in all three directions and in terms of its standard deviation, in all four trials, the controller reduces the motion in all three directions by roughly 50%.

Improved performance can be achieved in the simulation by using higher gains, namely proportional and derivative. However, during the test flights, instabilities occurred if the gains were increased beyond the values given in Tables 5.2 and 5.3. The experimental limit of the gains is likely imposed by the GPS measurement noise, which is not included in the model. From the PSD plots, it is observed that the controller is most effective at the lowest frequencies, and has little impact beyond about 0.05 Hz. Efforts in Chapter 6 will focus on expanding its effective bandwidth with the use of more advanced controllers than the simple PID. The complete and validated dynamics model becomes a useful tool for evaluating and testing controllers before implementation on the experimental system.

5.3 Modal Analysis

A dominant vertical mode has been observed during both open (Figure 5.1) and closed-loop (Figure 5.4) results. Characteristics of this vertical bounce mode observed at 0.13 - 0.2 Hz can be identified by performing a modal analysis on the linearized system described in Section 3.8. The modal analysis consists of studying the eigenvalues and eigenvectors of the system matrix, $\mathbf{A}$. The unruly size (186×186) of $\mathbf{A}$ makes a comprehensive analysis of all the modes difficult; however, since the motion during flights and in simulation can be dominated by a single vertical oscillatory mode, this mode is the exclusive focus of this analysis. The results of this analysis are strictly only applicable to the uncontrolled behaviour of the system, but it may be possible to determine some of the mode's general characteristics from the modal analysis of the uncontrolled system.

A summary of the modal information for this mode is provided in Table 5.4 for the system at $\theta_{ze} = 0°$. The damped natural frequency, $\omega_d = 0.137$ Hz is similar to the frequency

Eigenvalues	$\gamma_{1,2}$	$-0.145 \pm 0.850i$
Frequency (Hz)	ω_d	0.137
Damping ratio	ζ	0.17
Eigenvector Elements (platform)	$\dot{x}_p$	$0.001 \pm 0.0001i$
	x_p	$0.011 \pm 0.0003i$
	$\dot{y}_p$	$-0.001 \pm 0.0004i$
	y_p	0.005
	$\dot{z}_p$	$0.012 \pm 0.070i$
	z_p	$-0.0829 \pm 0.0002i$
Eigenvector Elements (aerostat)	$\dot{x}_A$	$0.0034 \pm 0.0005i$
	x_A	$-0.0001 \pm 0.0040i$
	$\dot{y}_A$	0
	y_A	0
	$\dot{z}_A$	$0.010 \pm 0.094i$
	z_A	$-0.11 \pm 0.0068i$

Table 5.4: Characteristics of vertical bounce mode.

of the vertical mode observed during controlled tests. The modal damping is appreciable at $\zeta = 0.17$, but when the input disturbance is near the mode's natural frequency, resonance amplifies the mostly vertical motion as seen in the Bode plot of Figure 5.1. The elements of the eigenvectors indicate the relative amplitude and phase of the state variables. The magnitude of a complex eigenvector is a measure of the relative amplitude of its oscillatory behaviour, while the angle between eigenvectors in the real-imaginary plane indicates their phase angle difference. For brevity only the eigenvector values for the aerostat and platform's motion variables are included in Table 5.4. It is clear that this mode consists of mostly vertical motion as the horizontal eigenvectors are much smaller than their vertical counterparts. It is also interesting to note that the vertical motion of the aerostat and the platform are essentially in phase, which is what was observed during flight tests (see Figure 4.2). The amplitude ratio between the vertical position of the platform and the aerostat z_p/z_A = 0.0829/0.1093 = 0.76 is similar to the amplitude ratio observed in Figure 4.2 and Table 4.2 for the open-loop system during flight 4.

The overall performance of the system could be improved if certain characteristics of this mode such as the damping ratio and the amplitude ratio between the platform and aerostat could be altered. However, adding damping to the system is not trivial and would

likely involve adding some type of passive damping system, as the damping characteristics of the tethers are not easily manipulated. Perhaps the most direct and practical means to improving the behaviour of this mode is to reduce the stiffness of the leash. This does not alter the overall stiffness of the tension structure, but it does benefit the modal characteristics. The leash has relatively high stiffness as its strength member is comprised of Spectra, which has a modulus of elasticity of $E = 23.8$ GPa. If the elasticity of the leash is reduced to $E = 5$ GPa, the modal damping ratio increases to $\zeta = 0.19$ from 0.17. Although this seems like a modest gain, the amplitude ratio between the platform and the aerostat position decreased to $z_p/z_A = 0.49$ from 0.76. The benefits of using a low-stiffness leash and other leash damping strategies were investigated in greater detail by Deschenes and Nahon [81]. This brief study of the vertical bounce mode provides insight into the features of the mode and suggests a simple approach to reducing the problematic motion observed during tests.

5.4 Design Application

As demonstrated in the previous chapter, once the dependability of the dynamics model is established, it becomes a valuable design tool to evaluate and compare modifications to the positioning system. To illustrate the proficiency of the dynamics model complete with closed-loop tether actuation, the system is evaluated while changing two important design parameters; the number of support tethers and the size of the winch perimeter or base radius, R_B. Increasing the number of tethers beyond three potentially improves the positioning system as the additional tethers have the ability to stiffen the structure by maintaining tension during highly asymmetric configurations at extreme zenith angles. On the other hand, adding tethers also adds weight to the system, which reduces the amount of aerostat buoyancy that serves to tension the system. To analyze the precise implications of using more tethers, simulations were performed using 3, 4, 5 and 6 tethers.

Simulation results are presented for two configurations: the symmetric case ($\theta_{ze} = 0°$) and at the worst case ($\theta_{ze} = \theta_{az} = 60°$). The leash disturbance force implemented in the

Zenith angle, θ_{ze}	0°				60°			
# of tethers	3	4	5	6	3	4	5	6
Error in f.p. (m)	0.002	0.002	0.002	0.002	0.070	0.045	0.038	0.036
Error out of f.p. (m)	0.028	0.027	0.028	0.033	0.041	0.034	0.031	0.032

Table 5.5: Summary of simulated results with different numbers of tethers for configurations with a base radius, $R_B = 400$ m

Zenith angle, θ_{ze}	0°			60°		
Base radius (m), R_B	240	320	400	240	320	400
RMS error in f.p. (m)	0.002	0.003	0.002	0.007	0.018	0.036
RMS error out of f.p. (m)	0.009	0.017	0.033	0.018	0.021	0.032

Table 5.6: Summary of simulated results with different numbers of tethers for configurations with 6 tethers and base radii of $R_B = 240, 320$, and 400 m

simulation was taken from trial #3 on May 27 because of high winds during that test. A base radius, $R_B = 400$ m was used, which is greater than the experimental base radius of 364 m (at 364 m it was not possible to reach a zenith angle of 60°). A proportional controller with a gain of $K_P = 0.4$ s^{-1} was used for all simulations in this section. The results are summarized in Table 5.5, which gives the standard deviation of the position error. The error presented is separated into the error in the focal plane and out of the focal plane of the proposed radio telescope. The focal plane is tangent to the hemisphere of desired platform locations and the error in this plane is of primary importance for telescope operation.

At the zenith, there is a not significant difference between the results although the six-tether case has the largest errors. This suggests that at the zenith the additional weight from the three extra tethers impedes performance more than their added stiffness improves it. For the 60° zenith cases, the opposite is true as the position error is clearly reduced as the number of tethers increases, with the best performance in the focal plane achieved with six tethers. A plot of the results for the high zenith cases is given in Figure 5.10.

To fully take advantage of using more than three tethers, it is helpful to reduce the base radius, which reduces tether weight and hence increases tension. It is only possible to reduce the base radius if extra tethers are added as they provide the geometric configuration

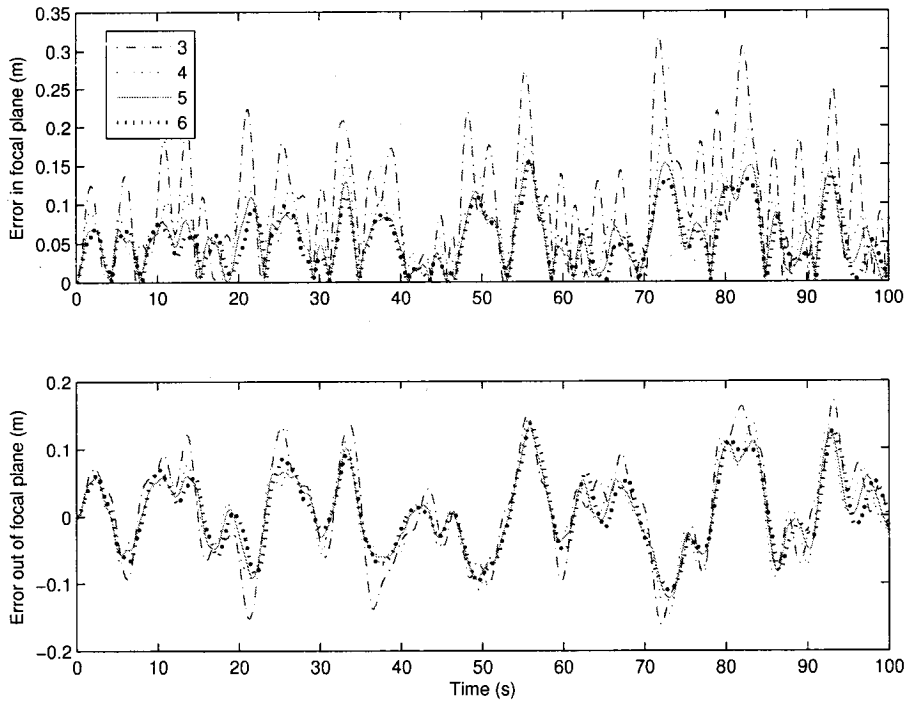

Figure 5.10: Comparison of simulated position error for system at $\theta_{ze} = 60°$ with 3, 4, 5, and 6 tethers.

necessary at high zenith angles. To study the effect of reducing the base radius, further simulations were performed with six tethers at base radii of 320 m and 240 m. The results for both zenith angles are summarized in Table 5.6 and the 60° zenith case is plotted in Figure 5.11. At $\theta_{ze} = 0°$, reducing the base radius has little effect in the focal plane but out of the focal plane the error decreases. This is not surprising as at the zenith, out of the focal plane corresponds to the vertical direction and as the base radius shrinks, the tethers become more vertical and hence stiffer in the vertical direction. At $\theta_{ze} = 60°$, the improvement in the focal plane is significant as the mean error is reduced to from 5 cm to 1 cm.

Coupling both the improvement from increasing to six tethers and reducing the base radius to 240 m, the RMS error in the focal plane with a zenith angle of 60° improved by an order of magnitude from 70 mm to 7 mm. Based on these results, six tethers with a base radius of 240 m appears to be the most logical choice for the design of the telescope. The

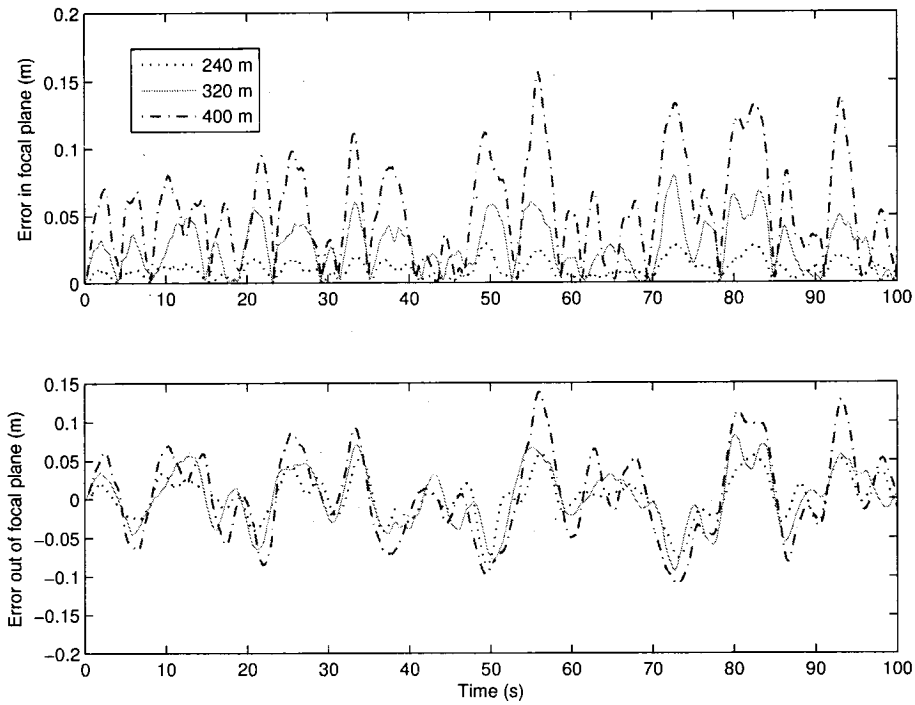

Figure 5.11: Comparison of simulated position error for case at $\theta_{ze} = 60°$ with 6 tethers and a base radius, $R_B = 240, 320$, and 400 m.

actual telescope will have a substantial feed or antenna structure located at the platform and using six tethers also enables the system to achieve some level of orientation control of the feed.

Chapter 6

Advanced Control

6.1 Introduction

Thus far the control of the multi-tethered aerostat system, both in experiments and in simulations, has been achieved using position feedback with a rudimentary PID algorithm. The selection of the PID controller for the initial investigation was based on the algorithm's simplicity with respect to both implementation and tuning. Although satisfactory closed-loop performance was observed with basic PID control, its performance is limited by the following three factors: 1) the tuned PID gains are sub-optimal, 2) it does not exploit the dynamics model of the system, 3) it uses only position measurements for feedback and does not take advantage of other measured parameters. Therefore, to advance the analysis of the positioning performance of the aerostat system, it is essential to study the potential enhancements of utilizing more advanced control techniques that overcome the major limitations of the PID controller.

The existence of a comprehensive dynamics model that has been thoroughly validated against experimental results, steers the controller development toward strategies that effectively exploit that model. Furthermore, because linear approximations of the full nonlinear model appear to adequately characterize the system, this study will be limited to linear control strategies. Optimal control techniques solve the sub-optimality problem as the linear model of the system can be used to algebraically solve for optimal gains. Earlier results for the aerostat positioning system indicated that the vast majority of undesired motion

was caused directly by fluctuations in the leash tension, which is a measured quantity. Therefore, to extend the controller beyond simple position feedback, control strategies that capitalize on the knowledge of the measured leash force are investigated.

This chapter begins with the development of the linear model accompanied by results confirming its similarity to the nonlinear model. An optimal controller employing full state feedback is presented first, showing impressive results compared to the original PID controller. For more practical implementation, this controller is combined with a state estimator or observer, which requires characterization of the stochastic properties of the disturbance and sensor noise. A feedforward component of the controller using the leash tension was added to the control system and this significantly enhanced the performance of the system. Practical issues concerning instrumentation such as measurement noise and bandwidth are shown to impact heavily on the performance of a combined feedforward and LQG optimal feedback controller. Finally, the applicability of this type of controller over a range of geometric operating conditions is evaluated.

Unfortunately the testing life of our aerostat BOB has lapsed and currently DRAO's LAR testing program is suspended. Therefore, the controller evaluation presented here will be based only on simulated results, however due to strength of the model validation in the previous chapter, confidence in the simulation results is justified.

6.2 Linear Model

As presented in Section 3.8, the linear approximation of the nonlinear system was obtained numerically using a finite difference technique. Expanding the linear model of eq.(3.31) to include an exogenous input, **w**, which is the disturbance acting on the platform from the aerostat's leash, gives the following LTI system:

$$\begin{aligned} \dot{\mathbf{x}} &= \mathbf{A}\mathbf{x} + \mathbf{B}\mathbf{u} + \mathbf{G}\mathbf{w} \\ \mathbf{y} &= \mathbf{C}\mathbf{x} \end{aligned} \tag{6.1}$$

where **x** is the state vector, **u** is the control input vector. The disturbance input, **w**, is the leash force divided by the mass of the platform. The output $\mathbf{y} = [x\ y\ z]^T$ is the position of

the platform. Because the aerostat is replaced by the leash force acting on the platform, the linear system has three less nodes and 18 less state variables than the nonlinear simulation (168 instead of 186).

The state and input matrices, $\mathbf{A}$ and $\mathbf{B}$, are computed numerically from the nonlinear simulation, whereas $\mathbf{G}$ is defined according to the node that the disturbance force is applied to. For our system, the disturbance, $\mathbf{w}$ is applied to the platform's node or point mass. This is a convenient method to characterize the disturbance since the leash force is a measured quantity during flight tests that can be converted to a vector in the inertial frame using position measurements as described in Section 4.2.1. To directly apply the disturbance, $\mathbf{w}$, to the platform's equations of motion, $\mathbf{G}$ is defined as:

$$\mathbf{G} = \begin{bmatrix} & \mathbf{0}_{162\times 3} & \\ 1/m_p & 0 & 0 \\ 0 & 0 & 0 \\ 0 & 1/m_p & 0 \\ 0 & 0 & 0 \\ 0 & 0 & 1/m_p \\ 0 & 0 & 0 \end{bmatrix} \tag{6.2}$$

where the non-zero rows correspond to the platform's velocity state variables, i.e. $x_{163} = \dot{x}_p$, $x_{165} = \dot{y}_p$, and $x_{167} = \dot{z}_p$. Dividing by the platform mass, m_p gives the disturbance input in units of acceleration.

The control input, $\mathbf{u}$, required by the linear model is the commanded tether length change (deviation from its equilibrium length) for each of three base tethers. However, to match the experimental controller and to attain greater control over the winch speeds, it is desirable to use the tether velocity, $\dot{\mathbf{u}}$, as the control variable instead of tether length, $\mathbf{u}$. The modifications to the linear model to use $\dot{\mathbf{u}}$ as the control variable while incorporating winch dynamics are presented in the next section.

The approach for analyzing the response of the system, with the aerostat replaced in the model by the measured leash force, neglects the effect of the control input on the aerostat. To quantify the neglected aerostat dynamics, two sets of simulation results were compared: one with control and one without control. The difference between the resulting leash tension and aerostat motion indicate the impact of the dynamics introduced by the control

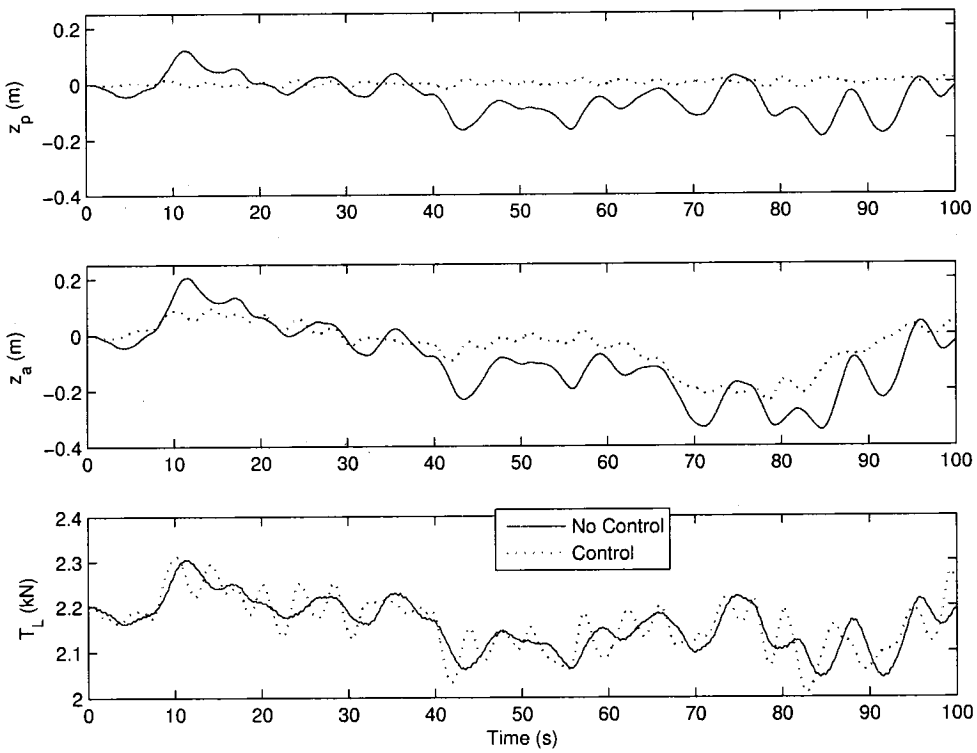

Figure 6.1: Comparison of simulation results with and without control to show the controller effects on the aerostat dynamics. Plots are given for the vertical platform and aerostat position as well as leash tension.

input. Figure 6.1 presents a comparison of results for the vertical platform and aerostat positions as well as the leash tension obtained using the complete nonlinear model (with aerostat and turbulent wind). A PID controller was used during the simulation that effectively limits the platform's vertical motion (this PID performs better than the experimental PID because the feedback frequency was 1000 Hz instead of 10 Hz), and at the same time reduces the aerostat's vertical motion. However, the controlled response comes at the expense of larger fluctuations in the leash tension. This confirms that the control input does have an impact on the aerostat's dynamics, and neglecting it from the controller evaluation analysis reduces the reliability of the simulation and likely leads to nonconservative results. This is considered acceptable for this work as the primary aim is to develop and test controllers that have the potential to improve on our PID control, and thus, the controllers simulated throughout this chapter will be assessed based on their performance relative to

the field-tested PID.

6.2.1 Incorporating Winch Dynamics

The dynamics model used up to this point has assumed that the winches were perfect actuators, i.e. the desired tethers lengths are accomplished instantly and exactly. Although it was understood that the mechanical components of the winches possessed characteristics such as inertia and friction that influence the dynamics of the closed-loop system, this influence was assumed to be negligible. The results presented in Chapter 5 showing good agreement between the closed-loop response of the experimental system and the model, confirm that the winch dynamics are not a significant factor in the closed-loop response with the 10-Hz PID controller.

However, the first efforts at studying an optimal controller produced feedback with much higher demands on the winches. To ensure that any controller developed would not involve an unrealistic response from the winches, the model was modified to incorporate the dynamics of the winch system. For simplicity, the winch response for each winch was modeled by a second-order system with the following transfer function:

$$\frac{\Delta \dot{u}(s)}{\Delta \dot{u}_c(s)} = \frac{\omega_n^2}{s^2 + 2\zeta\omega_n s + \omega_n^2} \tag{6.3}$$

where $\Delta \dot{u}_c$ is the change in commanded velocity, $\Delta \dot{u}$ is the actual change in velocity, and ζ and ω_n are the damping ratio and natural frequency of the winch dynamics. A series of tests were conducted with an isolated winch in attempt to estimate its second-order response. The experimental set-up for the winch tests is similar to the configuration of the winch damping experiment with a pulley and suspended load as shown previously in Figure 3.3. Several velocity step-response tests were performed and Figure 6.2 gives the results of one such step test. Both the measured step-response and the the second-order approximation are shown in Figure 6.2. The parameters for the model are $\zeta = 0.44$ and $\omega_n = 200$ rad/s. Both the rise time and the settling time for the second-order model are similar to the measured system, but it is clear that the exact dynamics are not matched with the second-order approximation as the measured response oscillates quicker and with

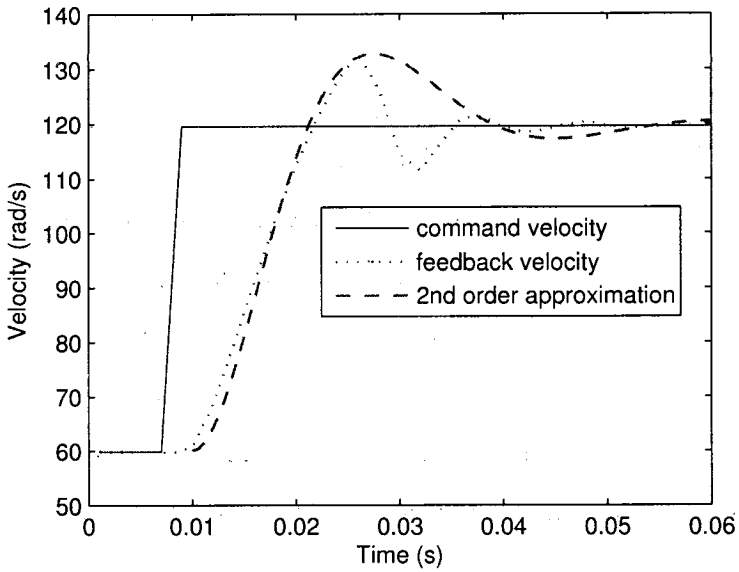

Figure 6.2: Winch velocity step response–input, measured response and second-order approximation.

more undershoot after the initial overshoot. The measured response is not exclusively due to the winch as the dynamics of the tether and the support boom inevitably contribute to the response as well. In fact the natural frequency for the vertical portion of the tether in the test is similar to oscillation measured during the step response. Therefore, it is acknowledged that the second-order approximation for the winch dynamics is based on results not exclusively due to the winches, but for the purpose of controller development, this second-order winch model should represent a conservative estimate of the actual winch dynamics.

To incorporate the winch model into the overall linear model of the system, it must be cascaded with an integrator to provide the tether actuation in units of length. The scalar form for one particular winch input in shown in Figure 6.3. The overall transfer function from $\dot{u}_c$ to u is:

$$\frac{u(s)}{\dot{u}_c(s)} = \frac{\omega_n^2}{s^3 + 2\zeta\omega_n s^2 + \omega_n^2 s} \tag{6.4}$$

To amalgamate the combined third-order transfer function with the plant of the original state-space system, it must first be converted to state-space form. There is not a unique

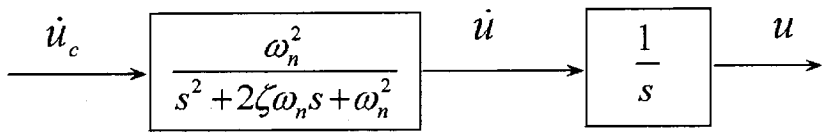

Figure 6.3: Transfer functions from desired velocity input to position input.

state-space representation for the winch dynamics, but one possible form is as follows:

$$\begin{aligned}\begin{bmatrix}\dddot{u}\\ \ddot{u}\\ \dot{u}\end{bmatrix} &= \begin{bmatrix}-2\zeta\omega_n & -\omega_n^2 & 0\\ 1 & 0 & 0\\ 0 & 1 & 0\end{bmatrix}\begin{bmatrix}\ddot{u}\\ \dot{u}\\ u\end{bmatrix} + \begin{bmatrix}\omega_n^2\\ 0\\ 0\end{bmatrix}\dot{u}_c\\ y &= \begin{bmatrix}0 & 0 & 1\end{bmatrix}\begin{bmatrix}\ddot{u}\\ \dot{u}\\ u\end{bmatrix}\end{aligned} \tag{6.5}$$

The dynamics of each of the three winches are described by this SISO system, which is readily expanded to a MIMO system that includes all three winch actuators.

$$\begin{aligned}\dot{\mathbf{u}}_w &= \mathbf{A}_w\mathbf{u}_w + \mathbf{B}_w\dot{\mathbf{u}}_c\\ \mathbf{y}_w &= \mathbf{C}_w\mathbf{u}_w\end{aligned} \tag{6.6}$$

where $\mathbf{u}_w$ is the total state vector for the winch system, $\mathbf{u}_w = [\ddot{u}_1\ \dot{u}_1\ u_1\ \ddot{u}_2\ \dot{u}_2\ u_2\ \ddot{u}_3\ \dot{u}_3\ u_3]^T$ and the output vector, $\mathbf{y}_w = [u_1\ u_2\ u_3]^T$. The 9×9 winch state matrix, $\mathbf{A}_w$, 9×3 input matrix, $\mathbf{B}_w$, and 3×9 output matrix, $\mathbf{C}_w$, are simple concatenations of the state space description of a single winch in eq. (6.5).

Figure 6.4 shows a simplification of two state-space systems in series by appending the intermediate output/input variable, $\mathbf{u}_w$, to the original state vector, $\mathbf{x}$, to create the augmented 177×1 state vector, $\tilde{\mathbf{x}} = [\mathbf{x}^T\ \mathbf{u}_w^T]$. The resulting state space system is given by:

$$\begin{aligned}\dot{\tilde{\mathbf{x}}} &= \tilde{\mathbf{A}}\tilde{\mathbf{x}} + \tilde{\mathbf{B}}\dot{\mathbf{u}}_\mathbf{c} + \tilde{\mathbf{G}}\mathbf{w}\\ \mathbf{y} &= \tilde{\mathbf{C}}\tilde{\mathbf{x}}\end{aligned} \tag{6.7}$$

where the matrices $\tilde{\mathbf{A}}$, $\tilde{\mathbf{B}}$, $\tilde{\mathbf{C}}$, and $\tilde{\mathbf{G}}$ are related to previously defined matrices given by:

$$\begin{aligned}\begin{bmatrix}\dot{\mathbf{x}}\\ \dot{\mathbf{u}}_w\end{bmatrix} &= \begin{bmatrix}\mathbf{A} & \mathbf{B}^*\\ \mathbf{0}_{9\times168} & \mathbf{A}_w\end{bmatrix}\begin{bmatrix}\mathbf{x}\\ \mathbf{u}_w\end{bmatrix} + \begin{bmatrix}\mathbf{0}_{168\times3}\\ \mathbf{B}_w\end{bmatrix}\dot{\mathbf{u}}_{c_{3\times1}} + \begin{bmatrix}\mathbf{G}\\ \mathbf{0}_{9\times3}\end{bmatrix}\dot{\mathbf{w}}\\ \mathbf{y} &= \begin{bmatrix}\mathbf{C} & \mathbf{0}_{3\times9}\end{bmatrix}\begin{bmatrix}\mathbf{x}\\ \mathbf{u}_w\end{bmatrix}\end{aligned} \tag{6.8}$$

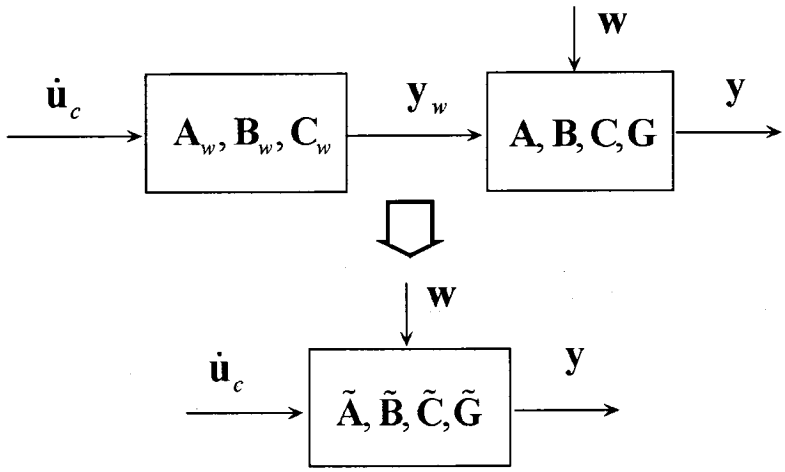

Figure 6.4: Concatenation of two state-space plants, one for the winch dynamics and one for the tethered system.

where $0_{i\times j}$ represents a null matrix of dimensions $i \times j$. All the matrices are as previously defined with the exception of B*, which is the original B matrix with 6 null columns added (the original 3 columns of B are 3rd 6th and 9th columns of B*).

Linear Simulation

Matlab's Simulink is used to simulate the response of the LTI system. The sole disturbance to the system is the input, $\mathbf{w}(t)$, which was obtained from the time history of the measured leash force from a flight on May 27, 2005. The vector components of the leash force in units of acceleration (measured force divided by the payload mass) are shown in Figure 6.5. This case was chosen because of its high wind speed ($\approx$ 4 m/s) relative to the other closed-loop flights. A comparison of linear and nonlinear simulations for an uncontrolled case in the symmetric configuration, ($\theta_{ze} = 0°$), is provided in Figure 6.6. The results show that the linear model slightly underestimates the motion in the horizontal directions while slightly overestimating the motion vertically. The discrepancies in the linear results can be attributed to the omission of certain nonlinear effects such as aerodynamic drag. However, the difference between the two sets of results is not significant enough to discourage usage of this linear model to develop and test controllers. Because linear controllers are easier

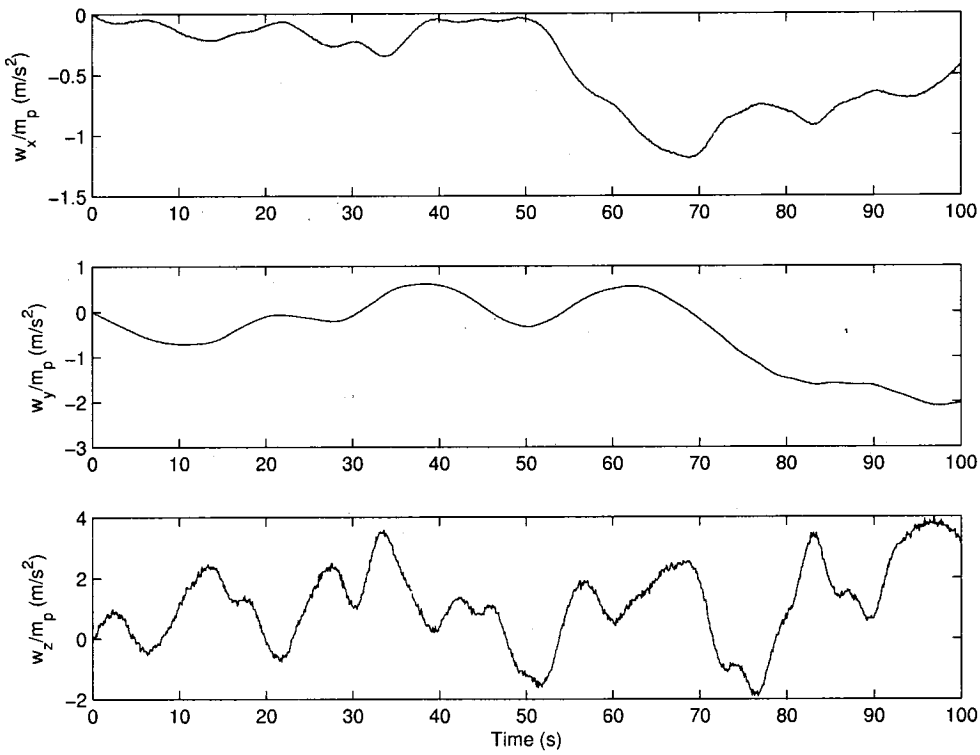

Figure 6.5: Leash disturbance measured during May 27, 2005 flight.

to implement and evaluate with the linear simulation, it is used during this first stage of the controller development process. Only promising controllers will make it through to the second stage which involves more complex implementation with the nonlinear simulation (beyond the scope of this work). The final stage is field testing, which is the most resource intensive, so only thoroughly analyzed controllers that perform well with the nonlinear simulation should make it to this stage.

6.3 Optimal Control

As discussed in Chapters 3 and 5, PID was the first control algorithm to be tested in both simulation and experiments due to its ease of implementation. To improve on the limited performance observed, an optimal controller is developed and tested. A linear quadratic regulator (LQR) is a suitable feedback mechanism for our application which requires effective disturbance rejection about an equilibrium state. A quadratic objective function is

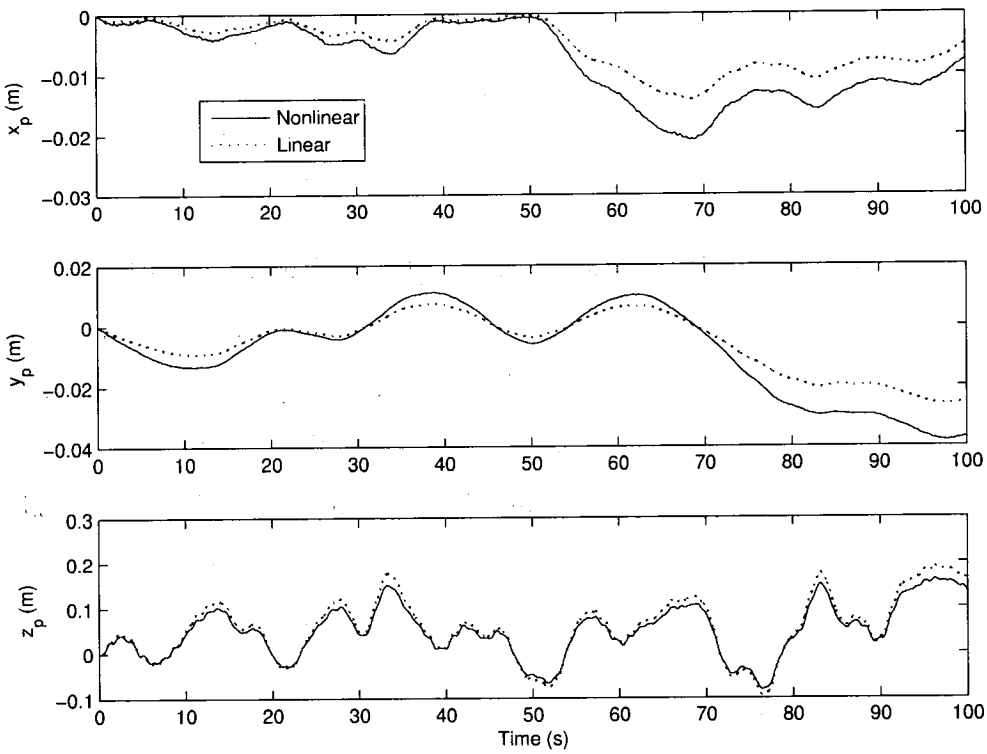

Figure 6.6: Comparison of nonlinear and linear simulation results for platform position with no control.

defined based on the output, $\mathbf{y}$, of the system (the platform position error) and the control input, $\dot{\mathbf{u}}$, as follows:

$$J = \int (\mathbf{y}^T \mathbf{Q} \mathbf{y} + \dot{\mathbf{u}}_c^T \mathbf{R} \dot{\mathbf{u}}_c) dt \tag{6.9}$$

where $\mathbf{Q}$ and $\mathbf{R}$ are 3×3 weighting matrices corresponding to the output and input respectively. In general, we are concerned more with minimizing the platform error, so the elements of $\mathbf{Q}$ will be greater than those of $\mathbf{R}$.

A common approach to finding the controller that minimizes the LQR objective function is based on solving the algebraic Riccati equation (ARE) to obtain the gain matrix, $\mathbf{K}$, used in feedback with the full state as $\dot{\mathbf{u}}_c = -\mathbf{K}\tilde{\mathbf{x}}$. Matlab's *lqry* function was utilized to solve the ARE and determine $\mathbf{K}$ for our state-space system defined by $\tilde{\mathbf{A}}$, $\tilde{\mathbf{B}}$, and $\tilde{\mathbf{C}}$. A block diagram of the LQR feedback control system is given in Figure 6.7.

This method of calculating optimal control gains neglects any exogenous input that

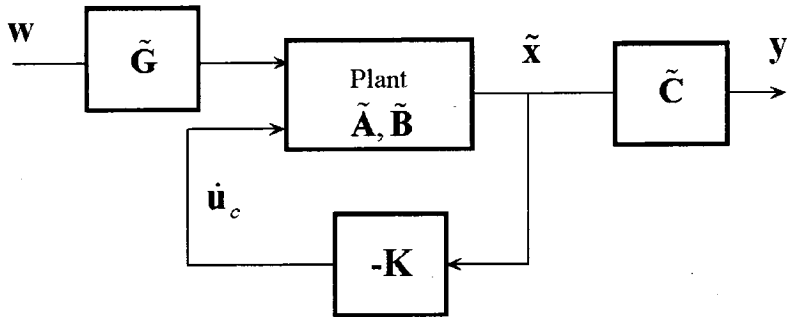

Figure 6.7: Block diagram of full-state feedback control system.

may be acting on the system, and therefore the controller is only optimal for the zero-input response where any perturbation is the result of nonzero initial conditions. This deterministic controller will not be optimal for this application as perturbations are caused by the disturbance, $\mathbf{w}(t)$. An alternative stochastic approach to the LQR regulator can recuperate optimality for a specific class of stochastic inputs [82]. The study in the present work represents a first step toward the development of an optimal controller and therefore only the deterministic LQR controller is considered. It is understood that the LQR results are not optimal in the strict sense, but perhaps optimal without assuming *a priori* knowledge of the disturbance.

6.3.1 LQR Stability

It is known that an LQR closed-loop system is asymptotically stable provided the following three conditions are satisfied [83]:

- the system is controllable,
- $\mathbf{R}$ is positive definite,
- $\mathbf{Q}$ can be factored as $\mathbf{Q} = \mathbf{C}_q^T \mathbf{C}_q$, where $\mathbf{C}_q$ is any matrix such that $(\mathbf{C}_q, \tilde{\mathbf{A}})$ is observable.

The stability can also be determined by studying the poles of the system, which are the eigenvalues of the matrix $(\tilde{\mathbf{A}} - \tilde{\mathbf{B}}\mathbf{K})$. The poles for the optimal controller presented in the

following sections were found to lie exclusively in the left hand plane, confirming stability.

6.3.2 LQR Results

To test the performance of the LQR controller, simulations of the closed-loop system were performed first with the linear system via Simulink to assess its relative performance, and secondly with the full nonlinear model to confirm its behaviour. Figure 6.8 shows both nonlinear and linear simulation results using the same LQR feedback matrix $\mathbf{K}$ and the same disturbance forcing function (from May 27 flight) for the system at the symmetric configuration, $\theta_{ze} = 0^o$. The output weighting matrix, $\mathbf{Q}$, was a diagonal matrix with identical entries 10^6 while $\mathbf{R}$ was a 3×3 identity matrix. The results show that the LQR controller is quite effective as the platform motion is roughly one order of magnitude smaller than the uncontrolled case in Figure 6.6. The differences between the linear and nonlinear results are consistent with the uncontrolled case and are deemed similar enough to proceed with the linear controller development.

Although the cost function weighting greatly favours the output ($\mathbf{Q} >> \mathbf{R}$), the resulting control inputs are not excessive. For the results in Figure 6.8, the winch velocities were below 12 cm/s (all but occasional spikes were below 10 cm/s), which is less than the 23 cm/s capability of our winch system. A portion of the winch velocities for the linear results are given in Figure 6.9 (the case with equal weighting in $\mathbf{Q}$ matrix).

During our prior experimental and simulation work, it was revealed that the system was more susceptible to disturbances in the vertical direction. This problem can be directly approached with LQR feedback by adjusting the output weighting matrix, $\mathbf{Q}$, to place a greater penalty on vertical deflections as:

$$\mathbf{Q} = \begin{bmatrix} 10^6 & 0 & 0 \\ 0 & 10^6 & 0 \\ 0 & 0 & 10^9 \end{bmatrix}$$

Linear simulation results in Figure 6.9 show improved performance in the vertical direction with this $\mathbf{Q}$, while the horizontal motion remains the same. From the input tether velocities, $\dot{u}_1$, $\dot{u}_2$ and $\dot{u}_3$ in the lower plot, it is observed that the improved performance comes at the

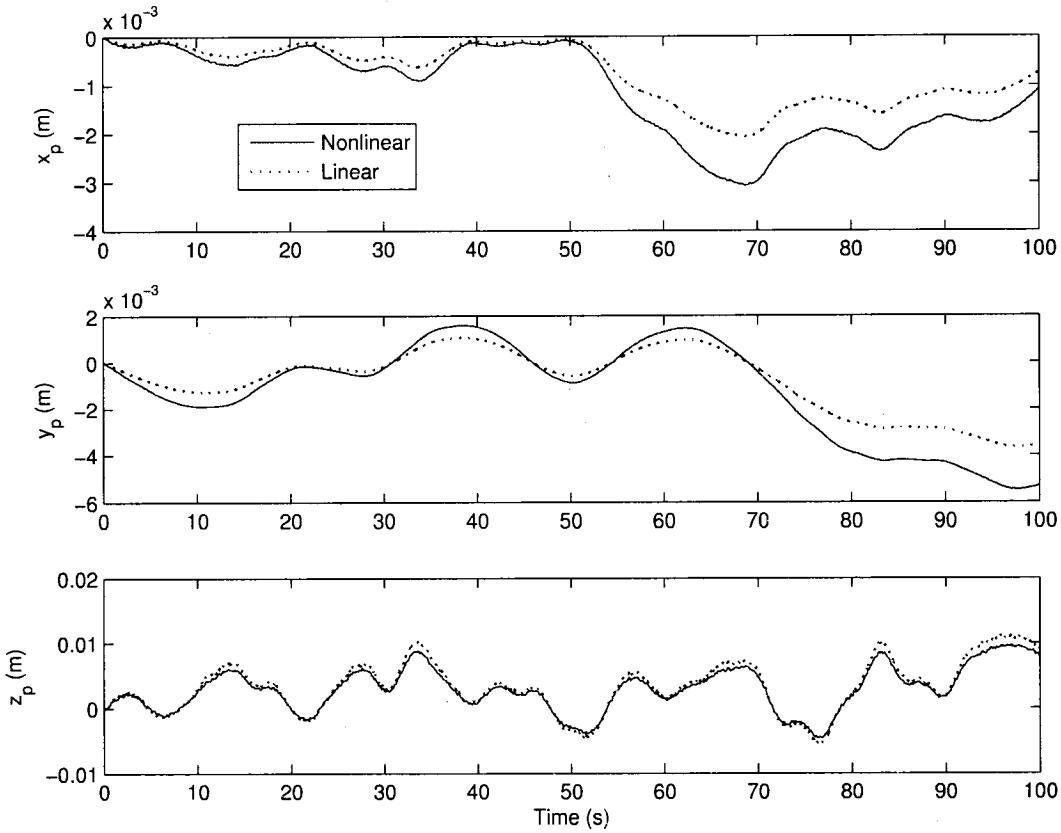

Figure 6.8: Comparison of nonlinear and linear simulation results for platform position with an LQR controller.

expense of higher velocities and accelerations. Although the maximum velocity is still within the permissible range, the acceleration (from a maximum of 3 m/s^2 to 10 m/s^2) exceeds the approximate winch acceleration limit of 5 m/s^2.

Although the LQR controller results presented are encouraging in terms of precision of the positioning system, the demands on the sensor and actuator hardware in terms of full-state measurement, high bandwidth and large accelerations are unrealistic. Controller development that respects the practical limitations of our system will be presented in the subsequent sections.

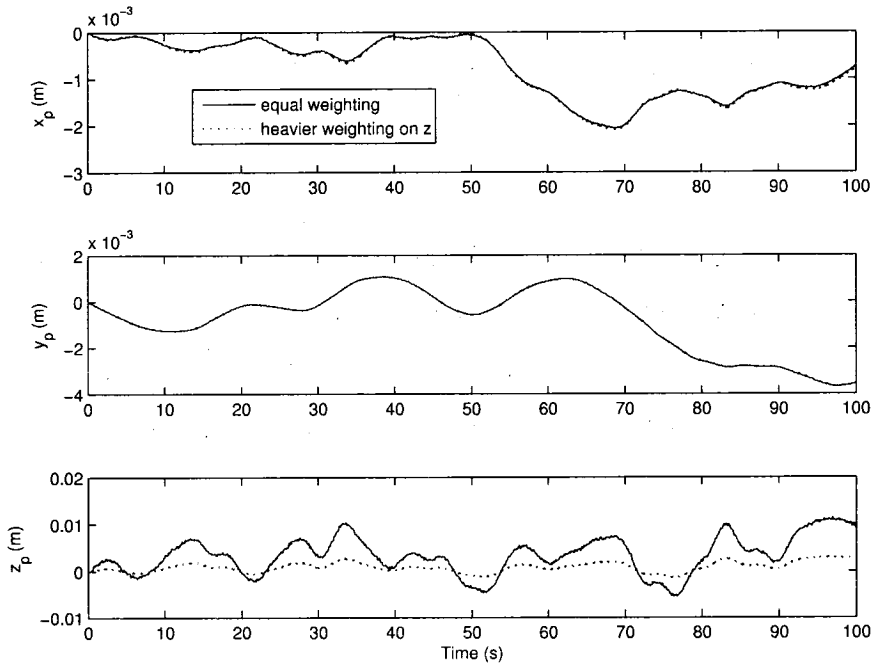

(a)

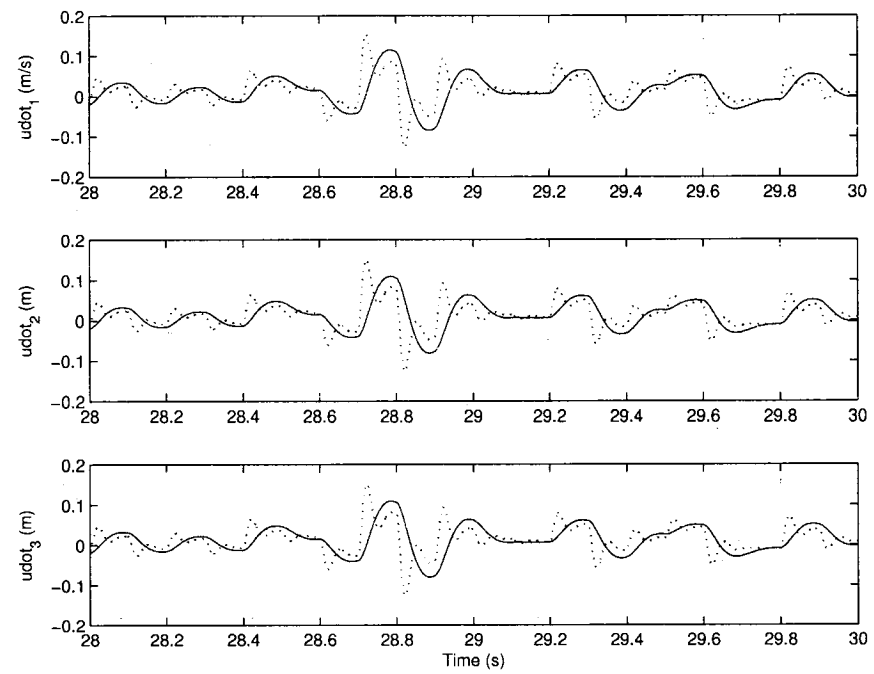

(b)

Figure 6.9: Comparison of linear simulation results with an LQR controller based on different weighting matrices: a) platform position, b) winch velocity during 2-second interval.

6.3.3 State Estimation

Because it is not reasonable to measure the entire state vector, implementing an optimal LQR controller must involve state estimation. In the experimental system, the platform positions are is the only state variables measured, and therefore the remaining state variables must be estimated based on those measurements. An optimal approach to state estimation commonly known as a Kalman filter, was first introduced by Kalman and Bucy in 1960. Using the separation principle of splitting the optimal feedback into two distinct steps, optimal state estimation and multiplication with the LQR feedback gain, is known as the linear quadratic Gaussian (LQG) problem. The term Gaussian refers to the statistical distribution of the plant noise, $\mathbf{n}$ and measurement noise, $\mathbf{v}$ represented in the following description for a generic state-space system:

$$\begin{aligned} \dot{\mathbf{x}} &= \mathbf{A}\mathbf{x} + \mathbf{B}\mathbf{u} + \mathbf{G}\mathbf{n} \\ \mathbf{z} &= \mathbf{C}\mathbf{x} + \mathbf{v} \end{aligned} \tag{6.10}$$

the main differences between our LTI system of eq. (6.7) and eq. (6.10) are the introduction of the measurement noise, $\mathbf{v}$, and the replacements of the disturbance, $\mathbf{w}$, by the Gaussian plant noise, $\mathbf{n}$, and output, $\mathbf{y}$, by the measurement output, $\mathbf{z}$. The structure of the Kalman filter presented is based on the generic description of eq. (6.10); however it will be applied to the system of eq. (6.7), which will be modified in the following sections to accommodate the filter's requirements. Specifically, the plant model within the filter must be adapted so that it is driven by a zero-mean white-Gaussian (ZMWG) process, $\mathbf{n}$, instead of the actual disturbance, $\mathbf{w}$.

The state estimator for the Kalman filter is given by the following differential relationship:

$$\dot{\hat{\mathbf{x}}} = \mathbf{A}\hat{\mathbf{x}} + \mathbf{B}\mathbf{u} + \mathbf{L}(\mathbf{z} - \mathbf{C}\hat{\mathbf{x}}) \tag{6.11}$$

where $\hat{\mathbf{x}}$ is the estimated state and $\mathbf{L}$ is the Kalman gain. The Kalman gain is calculated by solving an algebraic Riccati equation that uses an estimate of the state covariance matrix, $\mathbf{P}$. The state covariance, $\mathbf{P}$, is central to the operation of a Kalman filter and it is estimated along with the gain, $\mathbf{L}$, at each iteration of the algorithm. Embedded in the algorithms

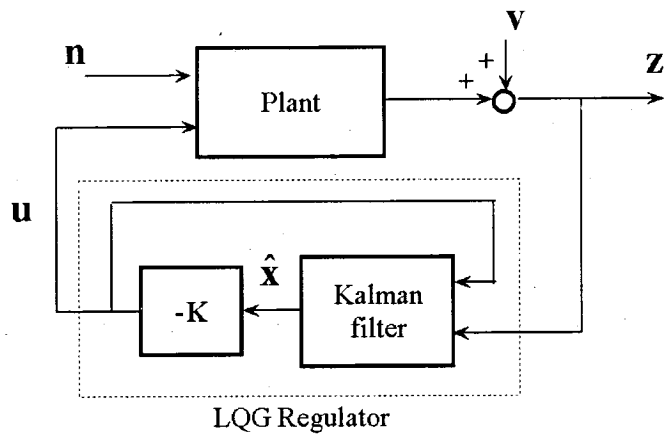

Figure 6.10: LQG regulator with Kalman filter state estimation and LQR feedback.

solving for the gain, $\mathbf{L}$ and state covariance matrix, $\mathbf{P}$, are the dynamics model parameters, $\mathbf{A}$, $\mathbf{B}$, $\mathbf{C}$, and $\mathbf{G}$, as well as the covariance matrices, $\mathbf{Q}_k$ and $\mathbf{R}_k$, of the the plant noise, $\mathbf{n}$, and measurement noise, $\mathbf{v}$, respectively.

$$\mathbf{Q}_k = E(\mathbf{n}\mathbf{n}^T) \quad \mathbf{R}_k = E(\mathbf{v}\mathbf{v}^T) \tag{6.12}$$

where $\mathbf{n}$ and $\mathbf{v}$ are both assumed to be ZMWG processes. A block diagram of the general operation of the LQG regulator is shown in Figure 6.10.

LQG Implementation

For simulations with the linear Simulink model, Matlab's *kalman* function is used to calculate the Kalman gain, $\mathbf{L}$, and *lqgreg* is used to combine the Kalman filter with the LQR gain, $\mathbf{K}$, of Section 6.3 into a single LTI system. The state-space description of the generic system is presented in continuous time in eq. (6.10), but the Kalman filter implemented in Simulink is discrete. Therefore Matlab performs an implicit conversion of the system from continuous to discrete state-space forms.

The measurement vector, $\mathbf{z}$, for the tethered aerostat system contains the platform position and the length change for each tether, i.e. $\mathbf{z} = [\tilde{x}_{164}\ \tilde{x}_{166}\ \tilde{x}_{168}\ \tilde{x}_{171}\ \tilde{x}_{174}\ \tilde{x}_{177}]^T$ or $\mathbf{z} = [x_p\, y_p\, z_p\, u_1\, u_2\, u_3]^T$. The tether length was not measured during our experimental tests, but it becomes a necessary feedback variable when estimating the extra states introduced

with the winch dynamics. It is feasible to measure the tether length using existing sensors like motor encoders, but for high accuracy, it may be necessary to add sensors. For the initial implementation of the LQG regulator, sensor noise is assumed to be zero, $\mathbf{v} = \mathbf{0}$, and the estimated covariance matrices, $\mathbf{Q}_k$ and $\mathbf{R}_k$, are chosen such that the variance of the measurement noise is much smaller than the variance of the plant noise.

$$\mathbf{Q}_k = \mathbf{I}_{3\times 3} \qquad \mathbf{R}_k = 10^{-10}\mathbf{I}_{6\times 6} \tag{6.13}$$

By choosing the covariance of $\mathbf{Q}_k$ to be significantly higher than $\mathbf{R}_k$, the filter will assume that the dynamics observed in the measured output, $\mathbf{z}$, are wholly due to the plant noise, which in the simulation is represented by the leash disturbance, $\mathbf{w}$.

Figure 6.11 presents simulated results of the LQR and LQG control schemes. The results are similar with slightly higher position error with the LQG controller, which is expected since it involves state estimation prior to feedback. These results demonstrate the observability of the system and the disturbance rejection capabilities of the LQG regulator, provided its state estimation is based on noise free measurements.

The results also assume that the plant model used in both the filer estimation algorithm and the optimal gain calculation is identical to the actual plant whose dynamics are driving the simulation. This will clearly never be a valid assumption in practice as no model can perfectly describe a real system. This preliminary investigation is based on ideal conditions and depending on the results of this 'best case' performance, decisions can be made as to how to proceed with developing a practical controller. Practical concerns will be addressed in subsequent sections related to controller bandwidth, measurement noise and robustness to plant uncertainty.

6.3.4 Feedback Frequency and Discrete-Time Control

The linear system studied thus far is based on continuous-time equations such as eq. (6.7). Solving this system of equations requires some form of numerical discretization, but if the integration time-step, t_{step}, is small enough, then the controller based on continuous-time equations provides the desired results with a discrete implementation. When simulating the

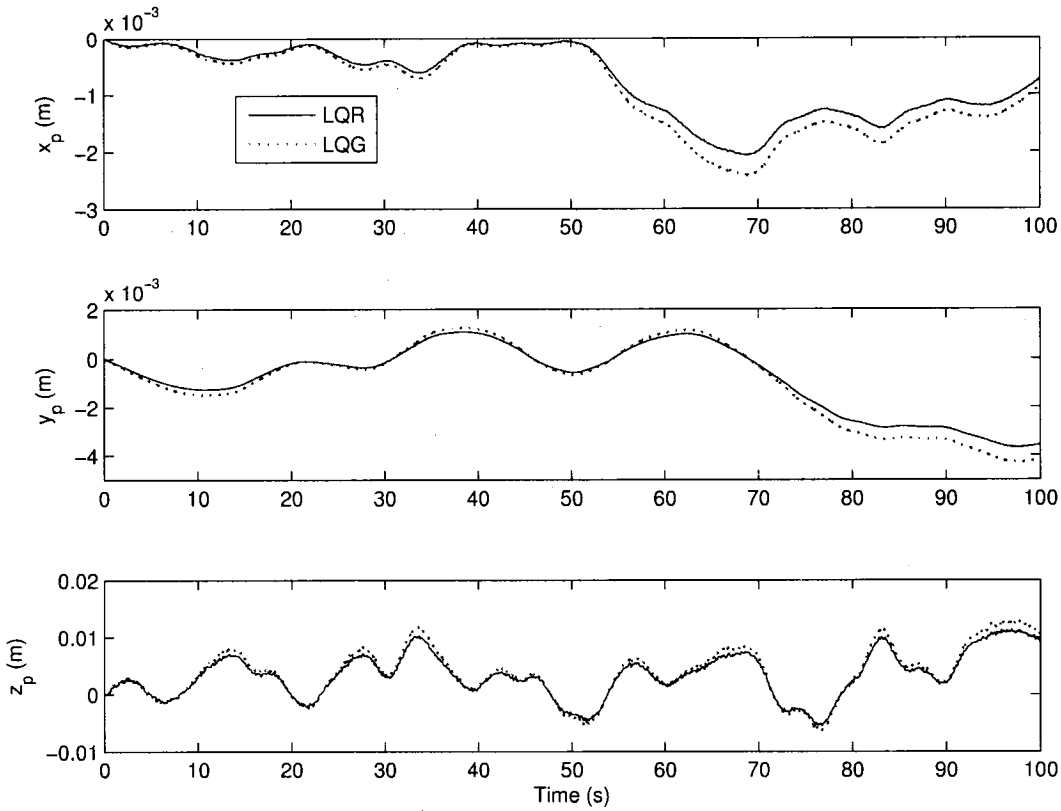

Figure 6.11: Comparison of simulation results with an LQR controller with full state feedback and an LQG controller with estimated states.

closed-loop linear system, it is assumed that measurements are available at each integration time step (i.e. the sampling time, $T_s = t_{step}$), but in practice measurement bandwidth is limited by sensor hardware.

The remote nature of our instrumentation system, deployed at a height of 170 m, severely constrained the bandwidth of its position measurement system. Relying on GPS sensors, with a maximum frequency of 10 Hz or a sample time of $T_s = 0.1$ s, our measurement frequency is not sufficiently fast relative to the dynamics of the system. Therefore, the LQR controller development must be based on a discrete-time model of the system that is dependent on the feedback or sampling time-step, T_s. The equivalent discrete-time model of the system of eq. (6.7), neglecting the exogenous input, w, since it is not included

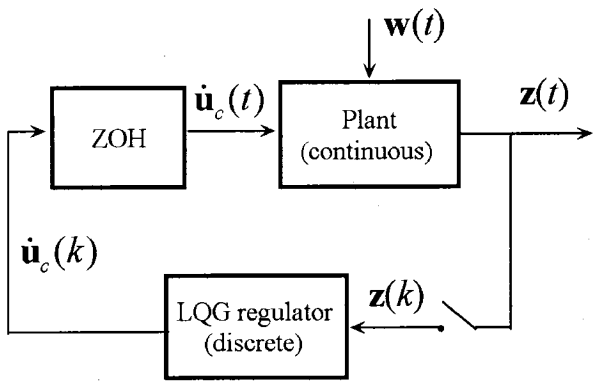

Figure 6.12: Block diagram of discrete-time LQG controller and continuous plant.

in the controller development, can be written as:

$$\begin{aligned} \mathbf{x}(k+1) &= \mathbf{A}_D\mathbf{x}(k) + \mathbf{B}_D\mathbf{u}(k) \\ \mathbf{y}(k) &= \mathbf{C}\mathbf{x}(k) \end{aligned} \tag{6.14}$$

The discrete state and input matrices, $\mathbf{A}_D$ and $\mathbf{B}_D$, can be solved for using the continuous matrices $\tilde{\mathbf{A}}$ and $\tilde{\mathbf{B}}$ as follows [84]:

$$\begin{aligned} \mathbf{A}_D &= e^{\tilde{\mathbf{A}}T_s} \\ \mathbf{B}_D &= \left(e^{\tilde{\mathbf{A}}T_s} - \mathbf{I}\right)\tilde{\mathbf{A}}^{-1}\tilde{\mathbf{B}} \end{aligned} \tag{6.15}$$

For convenience Matlab's *c2d* function was used to convert the LTI system from continuous-time to discrete-time based on the specified sampling time, T_s. The discrete-time state-space system is used to calculate a suitable gain matrix, $\mathbf{K}$, and discrete-time Kalman filter within the LQG regulator. Both Matlab functions *lqry* and *kalman* accept continuous or discrete state-space systems as input. To obtain simulation results using the controllers based on discrete time, the actual plant remains a continuous LTI system, and the discrete control input, $\dot{\mathbf{u}}_c$, passes through a zero-order hold (ZOH) before entering the plant. Figure 6.12 depicts the schematic arrangement of a continuous plant receiving feedback from a discrete controller.

Discrete-Time Results

Results were obtained for LQG regulators (state feedback gain $\mathbf{K}$) designed and operated at three frequencies, 10 Hz, 100 Hz and 2000 Hz. The lowest frequency, 10 Hz corresponds

Controller	σ_x	σ_y	σ_z	x_{max}	y_{max}	z_{max}
None	4.2	9.7	66.1	14.3	26.3	189.1
10 Hz	3.6	8.1	19.1	11.9	21.5	55.9
100 Hz	0.8	1.9	5.0	2.8	5.0	14.7
2000 Hz	0.7	1.6	4.4	2.4	4.3	13.0

Table 6.1: Summary of standard deviation and maximum displacements (in mm) for discrete LQG regulator.

to our experimental system, while the upper frequency, 2000 Hz, approaches the behaviour of the continuous time LQG, and the 100-Hz intermediate frequency provides an example of the performance at a bandwidth that is not altogether impractical. Figure 6.13 displays the position output for the three different control frequencies, and Table 6.1 shows the RMS and maxima of the results for platform position. The uncontrolled response is also included for comparison. The performance of the 100-Hz regulator is comparable to the 2000-Hz results, but when the sampling rate is reduced to 10 Hz, the effectiveness of the controller degrades significantly. In the horizontal x and y-directions the 10-Hz controller barely improves on the uncontrolled case. It performs better in the vertical z-direction as the standard deviation and maximum displacement at 10 Hz are a factor of three less than with no control.

The power spectra of both the platform motion and the winch input are given in Figure 6.14. Results are given for winch 1 only as its spectrum is similar to the other two winches, and the motion in the y-direction is omitted as its spectrum closely resembles the plot for the x-direction. It is interesting to observe the peak near 2 Hz for the 10-Hz LQG regulator in the PSD of both the winch input and the z-direction. Although the control frequency at 10 Hz is five times greater than the frequency of this mode, the regulator is not able to control the system without exciting it. At the higher frequencies of 100 Hz and 2000 Hz, this mode does not appear.

The relatively large amplitude perturbations in the platform position during the uncontrolled test are below 0.5 Hz horizontally and below 1 Hz vertically. The 10-Hz LQG controller is not effective at reducing this relatively low frequency motion in the horizon-

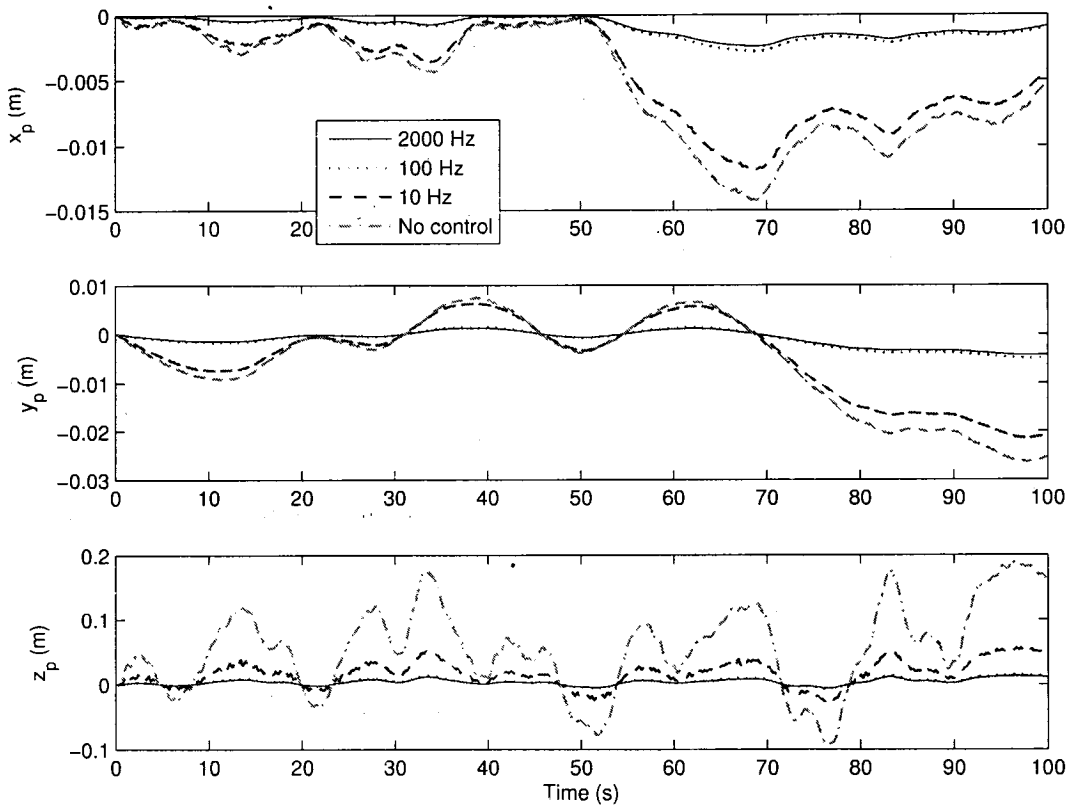

Figure 6.13: Comparison of simulation results with discrete-time LQG control at three different sampling frequencies.

tal direction. Although it is more successful in the vertical direction, the improvement is offset by the excitation of the vertical bounce mode. The 100-Hz controller is much more successful at reducing this low frequency motion both horizontally and vertically. This outcome is somewhat surprising as a 10-Hz controller was expected to be more effective controlling motion with frequencies one or two orders of magnitude lower than its own.

Comparison of LQG and PID

Table 6.2, Figure 6.15 and Figure 6.16 present results comparing the 10-Hz LQG regulator to the 10 Hz PID controller tested and tuned with the experimental system. Table 6.2 presents the standard deviation and maximum platform position error during the simulations, Figure 6.15 plots the time history of the platform motion and winch inputs in the form of tether lengths, and Figure 6.16 gives the PSD for the winch input and position in

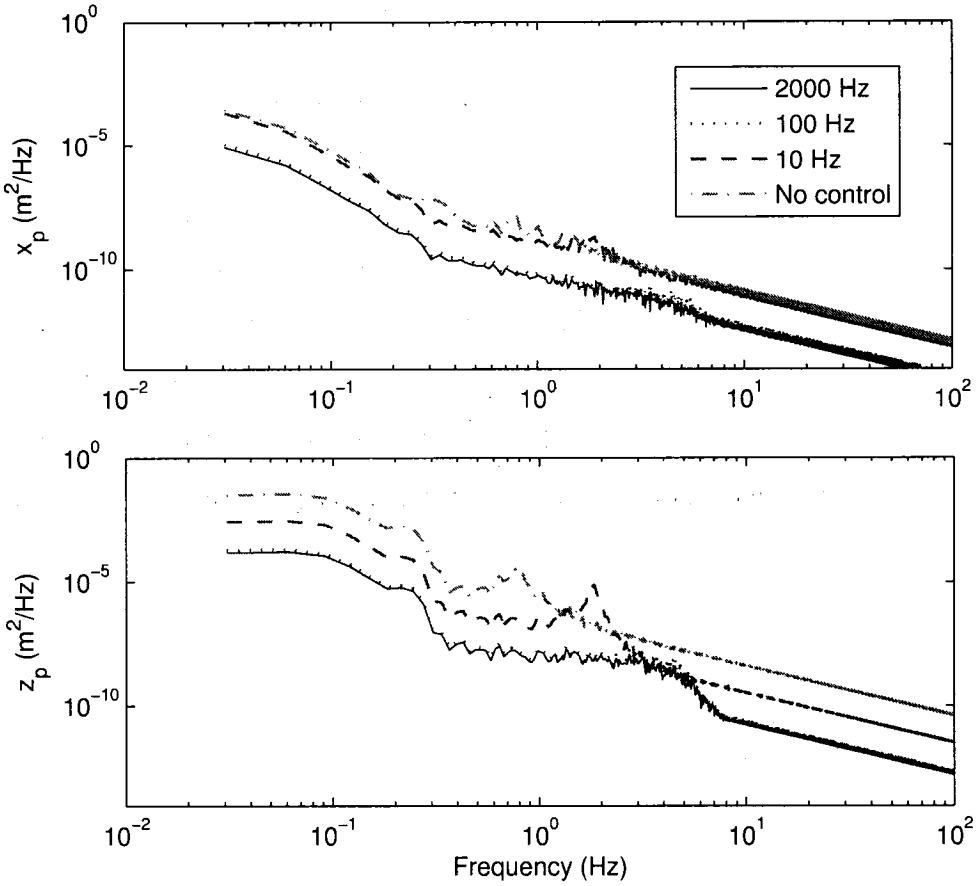

(a)

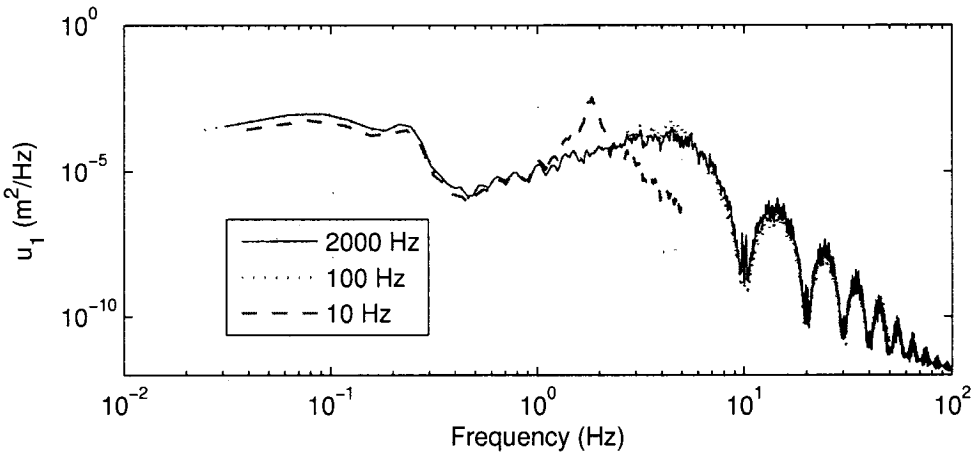

(b)

Figure 6.14: PSD of (a) platform motion in the x and z directions and (b) winch input at various discrete-time LQG control frequencies.

Controller	σ_x	σ_y	σ_z	x_{max}	y_{max}	z_{max}
LQG 10 Hz	3.6	8.1	19.1	11.9	21.5	55.9
PID 10 Hz	1.5	3.1	37.3	4.7	5.9	93.5

Table 6.2: Summary of standard deviation and maximum displacements (in mm) for 10 Hz discrete LQG and PID controllers.

the x and z directions. The PID controller results are from the nonlinear simulation using the algorithm presented in the previous chapter with gains, $K_P = 0.4\text{s}^{-1}$, $K_I = 0.05\text{s}^{-2}$, $K_D = 0.05$.

The results show that the PID controller is more effective than LQG in the horizontal plane as its standard deviation in x and y is roughly half that of the LQG, while in the vertical direction, the situation is reversed as the standard deviation for the LQG is half as high as with the PID. In terms of overall position error magnitude, the LQG controller is considerably better as the vertical perturbations of the platform position are much larger than the horizontal. The winch commands produced by the PID controller lag those of the LQG controller and have a smoother profile indicating less high-frequency content, which is confirmed in the PSD plot of Figure 6.16. The LQG controller is certainly more active at high frequencies, but both controllers have a peak in their command inputs near 1 Hz. The LQG peak has a larger amplitude and occurs at a higher frequency, approx. 2 Hz versus 0.8 Hz for the PID. The spectrum of the vertical position of the platform shows peaks at the same respective frequencies for each case, however, the amplitudes of the peaks are inversed with respect to the winch input. In summary, the smaller magnitude PID winch commands create greater vertical platform motion than the larger amplitude LQG commands, which suggests that the PID commands are closer to the open-loop bounce mode's natural frequency.

Overall, the optimal LQG regulator outperforms the basic PID controller, but at the low 10-Hz sampling frequency of our experimental system, both feedback controllers excite a vertical mode that effects their overall performance. At a feedback rate of 100 Hz, the LQG controller approaches the behaviour of a continuous-time optimal controller.

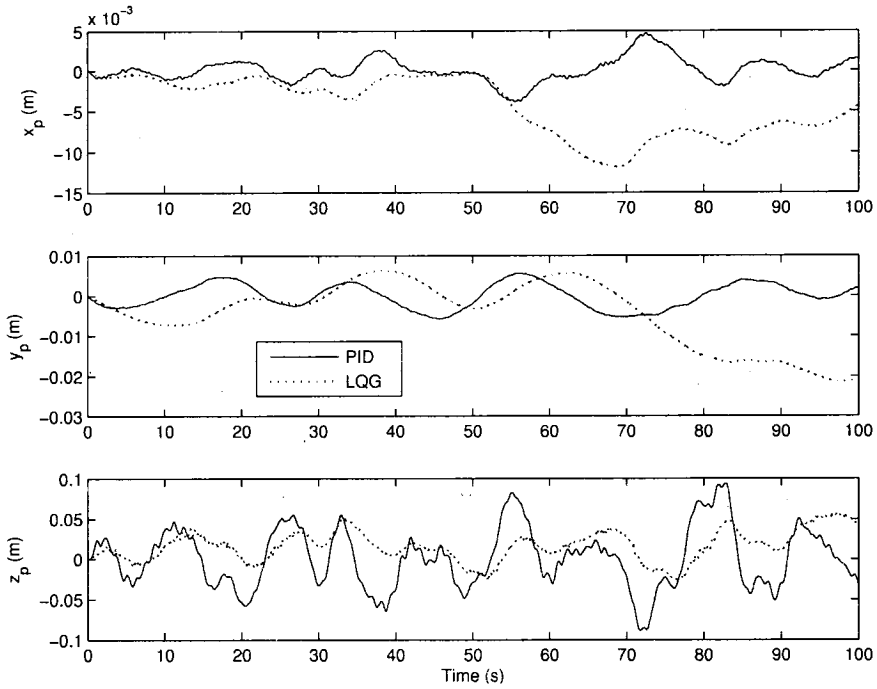

(a)

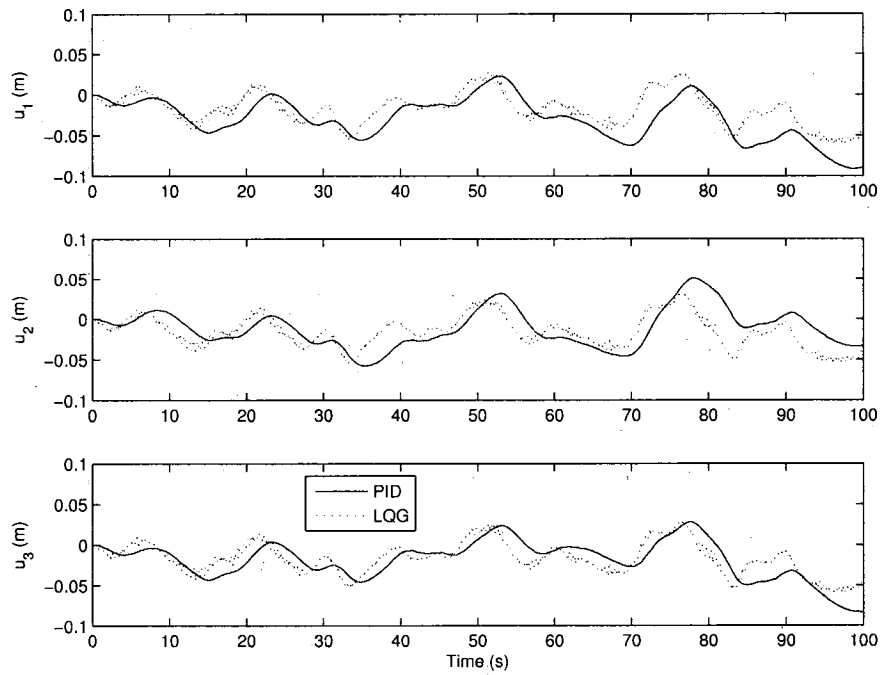

(b)

Figure 6.15: Comparison of 10-Hz PID and LQG simulation results: (a) platform position (b) tether length change from winches.

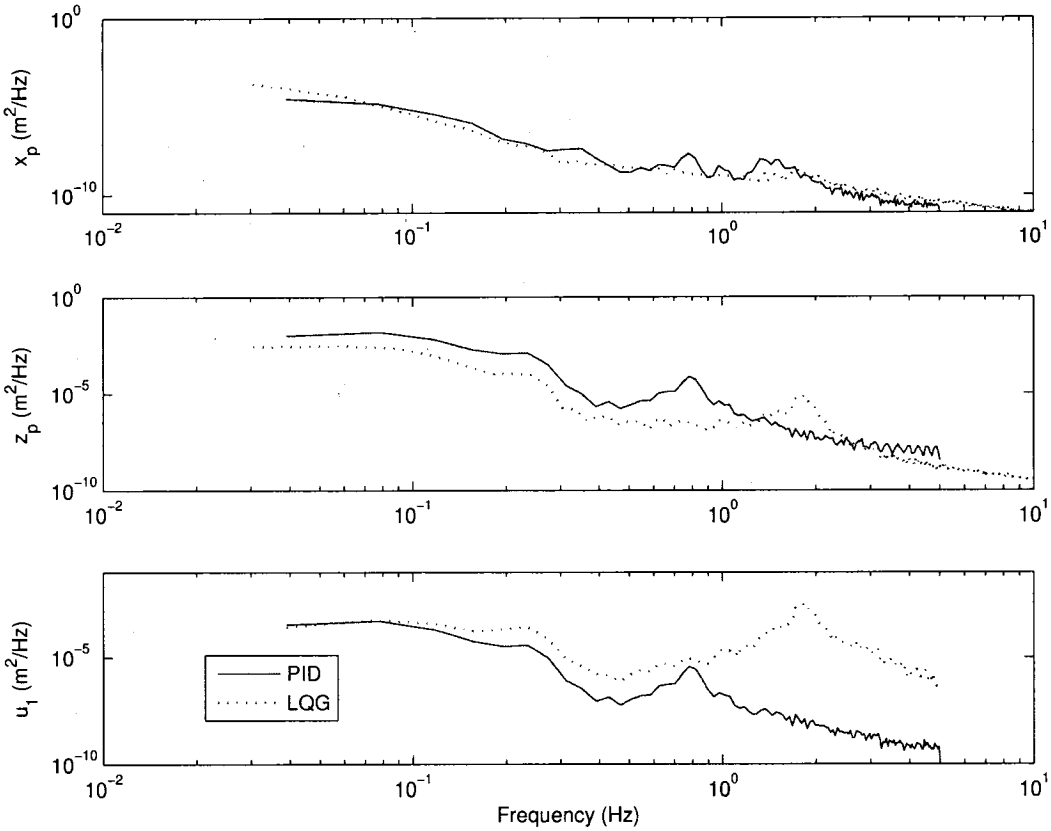

Figure 6.16: PSD comparison between LQG and PID controllers for winch input and platform position.

6.3.5 Measurement Noise

The simulations presented thus far have relied on perfect reporting of the measured state variables ($\mathbf{v} = \mathbf{0}$). Realistically, all measurements have some level of intrinsic inaccuracy or noise, which should be considered when designing practical control systems. The Kalman filter state estimation within the LQG regulator is designed to anticipate sensor noise and minimize its impact on the control process. The required assumptions are that both the plant noise and measurement noise are ZMWG processes, and reasonable estimates of their respective covariance matrices, $\mathbf{Q}_k$ and $\mathbf{R}_k$, are available. The more accurate the covariance estimates are, the more accurate the estimation process will be.

The LQG regulator in the preceding sections performed well, despite the fact that the

exogenous plant input was not ZMWG, only because of the absence of measurement noise and the specification that $\mathbf{Q}_k >> \mathbf{R}_k$. When even modest levels of measurement noise are present in the feedback output, $\mathbf{z}$, the state estimation within the LQG regulator degrades severely as the Kalman filter expects all the perturbations in the measurement to originate exclusively from the plant noise, which with noisy measurements is clearly not the case. Therefore because of the presence of measurement or sensor noise, accurate state estimation is only possible if the Kalman filter contains proper characterization of the exogenous plant input (plant noise) as a process driven by ZMWG noise with covariance $\mathbf{Q}_k$. The sensor noise itself must also be characterized as a process driven by ZMWG noise or a ZMWG process itself with covariance $\mathbf{R}_k$. For our system the measurement noise covariance matrix, $\mathbf{R}_k$ is:

$$\mathbf{R}_k = \begin{bmatrix} \sigma^2_{GPS_x} & 0 & 0 & 0 & 0 & 0 \\ 0 & \sigma^2_{GPS_y} & 0 & 0 & 0 & 0 \\ 0 & 0 & \sigma^2_{GPS_z} & 0 & 0 & 0 \\ 0 & 0 & 0 & \sigma^2_{u_1} & 0 & 0 \\ 0 & 0 & 0 & 0 & \sigma^2_{u_2} & 0 \\ 0 & 0 & 0 & 0 & 0 & \sigma^2_{u_3} \end{bmatrix} \tag{6.16}$$

Noise estimates are available for most sensors and alternatively, they can often be directly quantified during calibration. For the GPS sensors used for our position feedback, the noise can be estimated by observing output signals during static testing. Based on several tests, it was found that the average noise signal had a standard deviation of 0.005 m and a variance σ^2_{GPS} =(0.005 m)^2. The tether length change for each tether must also be measured, and although no specific sensors have been implemented to measure this, it is assumed that it can be measured more precisely than the platform position with GPS and its variance was chosen as σ^2_u =(0.001 m)^2 Although the actual noise inherent in the measurements will not be strictly white nor Gaussian, if its time-correlation is relatively small, the ZMWG assumption may produce acceptable results.

The plant noise for our system, represented by the leash force disturbances on the platform, $\mathbf{w}(t)$ was given in Figure 6.5. The disturbance is clearly not white noise, and therefore a pre-filter, referred to as a shaping filter, must be added to the dynamics model

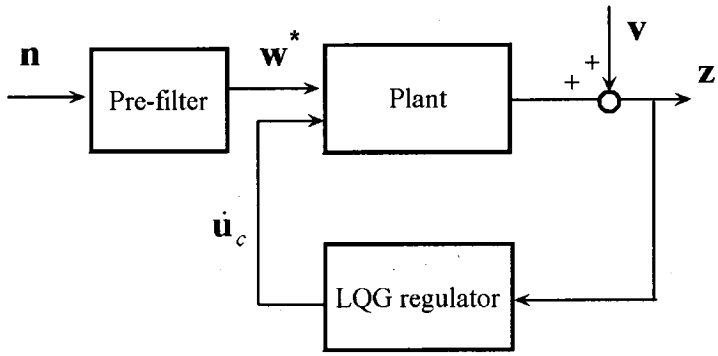

Figure 6.17: Representation of closed-loop LQG system with the leash force disturbance driven by a ZMWG process **n**.

of the system within the Kalman filter. The technique of filtering white noise to create a time-correlated process is known as colouring the noise. The concept is illustrated in Figure 6.17 where w* represents the disturbance force driven by the ZMWG process, $\mathbf{n}(t)$. It is important to state that the actual disturbance to the system remains the measured leash force, w, and w* is only a fictitious output of the shaping filter that should have the same stochastic properties as w. To include the shaping filter in the filter dynamics, the state-space description of the system within the Kalman filter must be modified to include the dynamics of the pre-filter.

Plant Noise Pre-Filter

A common approach for designing a pre-filter to colour a ZMWG process is to approximate the pre-filter output, w^*, as a first or second-order Gauss-Markov (GM) process. The first-order GM process is defined by the following differential equation:

$$\dot{w}^* = \frac{-w^*}{\tau} + n(t) \tag{6.17}$$

where $n(t)$ is a ZMWG process with a known intensity, Q and τ is the correlation time of w^*. The intensity is related to the covariance of the output signal, w^*, by $Q = 2\sigma^2/\tau$ [85]. The parameter identification for the pre-filter and the ZMWG input, $n(t)$, is accomplished by fitting the autocorrelation function of the GM process to the measured autocorrelation

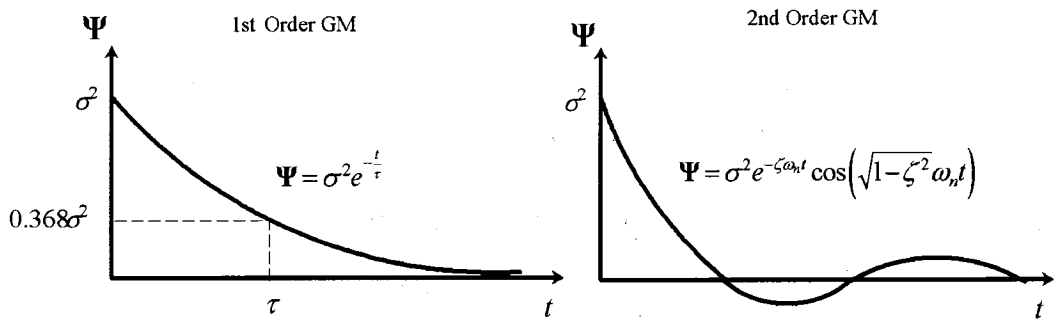

Figure 6.18: Typical autocorrelation function $\Psi(t)$ for first and second-order Gauss-Markov processes.

function of the components of $\mathbf{w}$. The features of a sample autocorrelation function, Ψ, for first and second-order Gauss-Markov processes are shown in Figure 6.18.

An attempt was made to characterize the three vector components of $\mathbf{w}(t)$ as first-order GM processes, but the y-component of the disturbance, $w_y(t)$, was clearly better defined by a second-order GM process. Figure 6.19 gives the autocorrelation function, $\Psi(t)$, for the components of the disturbance, $\mathbf{w}$, with the fitted autocorrelation functions for the virtual disturbance, $\mathbf{w}^*$.

A second-order Gauss-Markov process is generally expressed by the following transfer function [85]:

$$H(s) = \frac{as + b}{s^2 + 2\zeta\omega_n s + \omega_n^2} \tag{6.18}$$

which leads to a state-space description of:

$$\begin{aligned} \begin{bmatrix} \dot{w}_1 \\ \dot{w}_2 \end{bmatrix} &= \begin{bmatrix} 0 & 1 \\ -\omega_n^2 & -2\zeta\omega_n \end{bmatrix} \begin{bmatrix} w_1 \\ w_2 \end{bmatrix} + \begin{bmatrix} a \\ c \end{bmatrix} n(t) \\ w^* &= \begin{bmatrix} 1 & 0 \end{bmatrix} \begin{bmatrix} w_1 \\ w_2 \end{bmatrix} \end{aligned} \tag{6.19}$$

where the parameters a, b, and c can be solved for using the following relationships:

$$\begin{aligned} a &= \left(2\sigma^2\omega_n \sin\alpha\right)^{1/2} \\ c &= b - 2a\zeta\omega_n \\ b &= \left(2\sigma^2\omega_n^3 \sin\alpha\right)^{1/2} \\ \alpha &= \tan^{-1}\left(\frac{\zeta}{\sqrt{1-\zeta^2}}\right) \end{aligned} \tag{6.20}$$

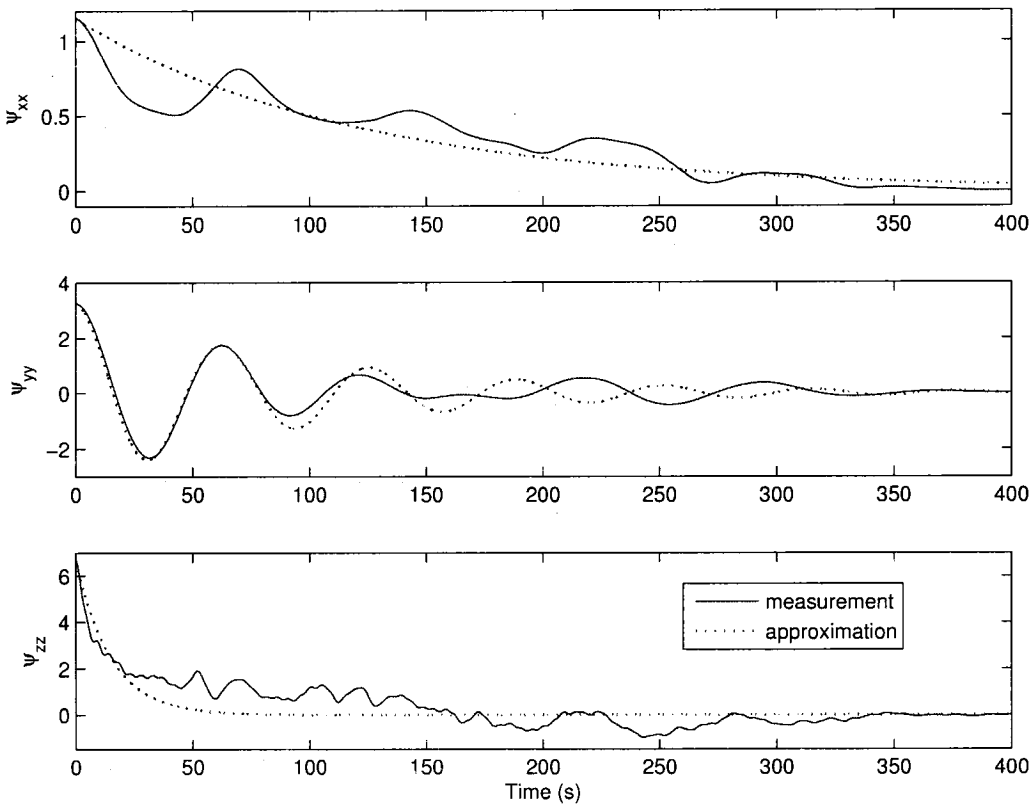

Figure 6.19: Autocorrelation for the leash disturbance input to the simulation, i.e. the plant noise. A fitted autocorrelation approximation for a process driven by ZMWG noise is also given.

The covariance, σ^2, damping ratio, ζ, and frequency, ω_n, of the output, $\mathbf{w}^*$, are determined by fitting the autocorrelation function for a second-order GM process to the experimental data. Table 6.3 summarizes the GM parameter estimation for the disturbance, $\mathbf{w}$.

The dynamics of the pre-filters must be incorporated into the state-space description of the system used by the Kalman filter. The total state vector must be expanded to include $\mathbf{w}^* = [w_x^* \; w_{y_1}^* \; w_{y_2}^* \; w_z^*]^T$ as the overall state-space system becomes:

$$\begin{aligned} \begin{bmatrix} \dot{\tilde{\mathbf{x}}} \\ \dot{\mathbf{w}}^* \end{bmatrix} &= \begin{bmatrix} \tilde{\mathbf{A}} & \tilde{\mathbf{G}}^* \\ \mathbf{0} & \mathbf{F}^* \end{bmatrix} \begin{bmatrix} \tilde{\mathbf{x}} \\ \mathbf{w}^* \end{bmatrix} + \begin{bmatrix} \tilde{\mathbf{B}} \\ \mathbf{0}_{4\times 3} \end{bmatrix} \dot{\mathbf{u}}_{c_{3\times 1}} + \begin{bmatrix} \mathbf{0}_{177\times 3} \\ \mathbf{H}^* \end{bmatrix} \mathbf{n} \\ \mathbf{z} &= \begin{bmatrix} \tilde{\mathbf{C}} & \mathbf{0}_{6\times 4} \end{bmatrix} \begin{bmatrix} \tilde{\mathbf{x}} \\ \mathbf{w}^* \end{bmatrix} + \mathbf{v} \end{aligned} \tag{6.21}$$

where $\tilde{\mathbf{G}}^*$ is similar to $\tilde{\mathbf{G}}$, but with an extra null column corresponding to the $w_{y_2}^*$ variable.

1st-order GM				2nd-order GM					
	σ^2	τ	Q		σ^2	a	c	ζ	Q
w_x	1.15	120	0.015	w_y	3.26	0.0255	0.0227	0.1	1
w_z	6.66	15	0.888						

Table 6.3: Summary of the GM parameters for the shaping filter for the disturbance **w**.

The remaining matrices are defined as:

$$\mathbf{F}^* = \begin{bmatrix} \tau_x^{-1} & 0 & 0 & 0 \\ 0 & 0 & 1 & 0 \\ 0 & -\omega_n^2 & -2\zeta\omega_n & 0 \\ 0 & 0 & 0 & \tau_z^{-1} \end{bmatrix} \quad \mathbf{H}^* = \begin{bmatrix} 1 & 0 & 0 \\ 0 & a & 0 \\ 0 & c & 0 \\ 0 & 0 & 1 \end{bmatrix} \tag{6.22}$$

The state-space description of eq. (6.21) is in the required form of eq. (6.10) for the Kalman filter. The filter also requires $\mathbf{R}_k$ from eq. (6.16) and the following $\mathbf{Q}_k$ to perform its state estimation.

$$\mathbf{Q}_k = \begin{bmatrix} Q_x & 0 & 0 \\ 0 & Q_y & 0 \\ 0 & 0 & Q_z \end{bmatrix} \tag{6.23}$$

where the variance of a stationary ZMWG process is equal to its signal strength.

Results with Measurement Noise

For this preliminary analysis, precise knowledge of the actual disturbance and the measurement noise are known. This is a luxury not available during operation of a practical system, however as mentioned before, ideal conditions are used to first simulate the 'best case' results in order to gauge the potential of the control system.

The noise, $\mathbf{v}(t)$, added to the measurements during the simulation was generated using Matlab's *randn* function, which outputs a pseudo-random ZMWG signal with a standard deviation $\sigma = 1$. The random noise signal is multiplied by the desired variance for each type of sensor as given in eq. (6.16).

Simulations were run using an LQG regulator with the modified state-space description of eq. (6.21) within the Kalman filter estimator. Figure 6.20 shows a comparison of LQG results for 10-Hz controllers both with and without measurement noise. The results are summarized in Table 6.4 along with results for a high-frequency 2000-Hz LQG controller and 10 Hz PID controller. The time history of the PID results are given in Figure 6.21.

Controller	σ_x	σ_y	σ_z	x_{max}	y_{max}	z_{max}
LQG 10 Hz	3.4(3.6)	7.9(8.1)	19.9(19.1)	11.7(11.9)	21.3(21.5)	57.9(55.9)
LQG 2000 Hz	1.4(0.7)	2.5(1.6)	6.9(4.4)	4.5(2.4)	7.2(4.3)	19.9(13.0)
PID 10 Hz	1.8(1.5)	3.3(3.1)	37.7(37.3)	5.3(4.7)	7.7(5.9)	93.5(92.4)

Table 6.4: Summary of standard deviation and maximum displacements (in mm) for discrete controllers with measurement noise; the results without noise are presented in brackets for comparison.

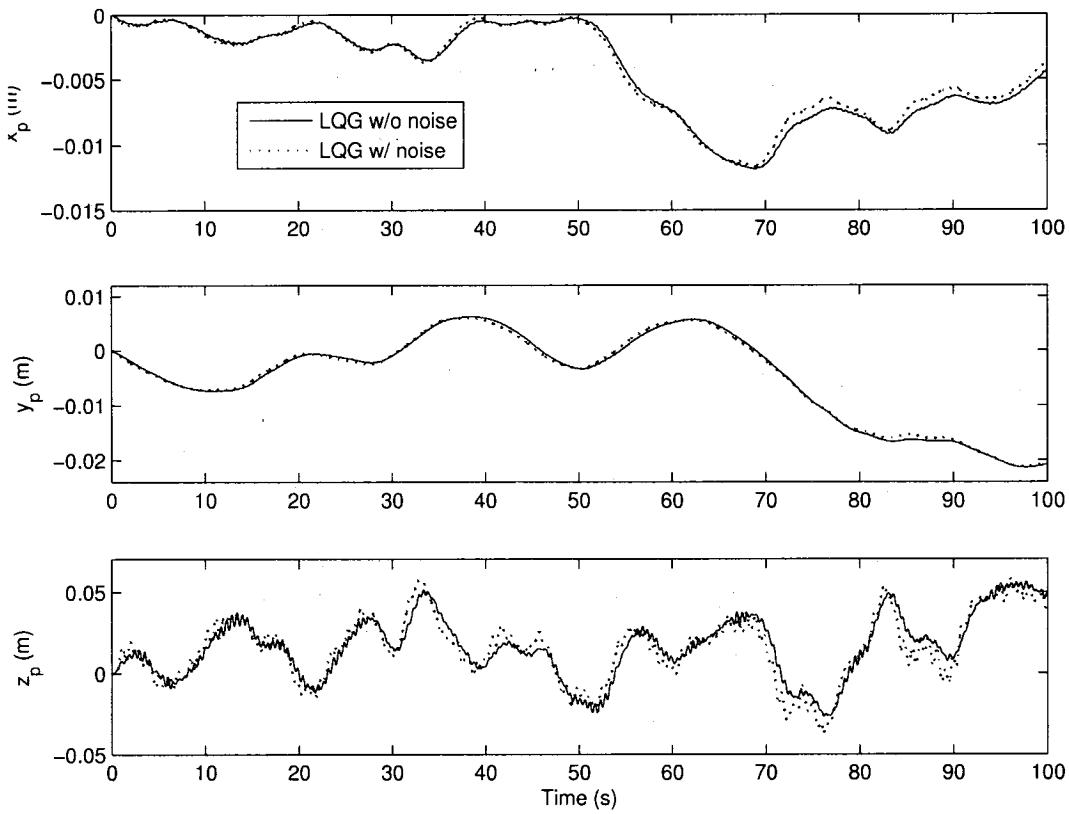

Figure 6.20: Comparison of simulation results for 10-Hz LQG controllers with and without the presence of measurement noise.

Overall, the measurement noise does not have a significant impact on the performance of the controllers. The 2000-Hz controller is the most sensitive to the noise as its platform motion nearly doubled. For the slower 10-Hz controllers, the effect of the noise was minor. For the LQG 10-Hz controller, the standard deviation of the vertical position increased slightly. A ringing effect is observed in the results which corresponds to the 2-Hz frequency

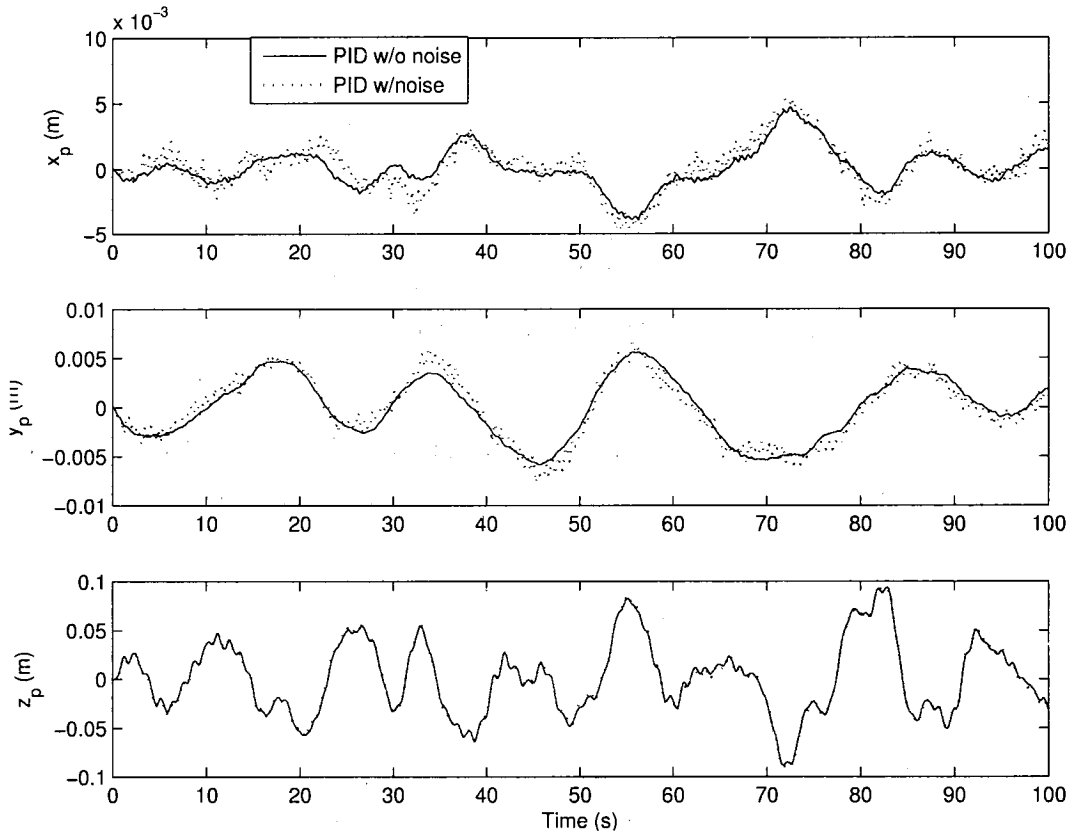

Figure 6.21: Comparison of simulation results for 10-Hz PID controllers with and without the presence of measurement noise.

observed in the 10-Hz LQG results in Section 6.3.4. From the PID results in Figure 6.21, the effects of the noise are observed as a low-amplitude high-frequency component of the platform position.

Relative to PID control, the LQG implementation is a much more complex and lengthy procedure as accurate models of the system, the disturbance and sensor noise are required. The advantage of the PID controller, although lacking optimality, is its adaptability as its gains are readily tuned prior to operation. In the presence of measurement noise, the LQG controller is observed to reduce the vertical motion by about 50% compared to the PID controller, which is encouraging and warrants further analysis for this application. However, the improvement in performance must be tempered with practical considerations associated with implementing the controller on the actual system.

Because the LQG results were based on ideal conditions that assumed: 1) the precise stochastic properties of the disturbance were available during the Kalman filter design stage and 2) the LQG's plant model exactly equals the real plant, further analysis of the LQG regulator is required.

Non-Ideal LQG Control

To further assess the LQG controller from a practical perspective, additional simulations were performed where the controller was not ideal in the sense mentioned in the previous section. The first set of simulation results are with an alternative disturbance, which has different stochastic properties than the filter was specially designed for, and the second set uses an alternative plant for the LQG design. The alternative disturbance implemented is from a flight on March 11, 2004 and is shown in Figure 6.22. This disturbance was chosen because of its obvious differences with the previously tuned disturbance of Figure 6.5.

Simulation results for 10-Hz optimal controllers are given in Figure 6.23 for the response to the alternative disturbance. One set of results are with an optimal LQR regulator with full-state feedback in the absence of noise, while the second set of results are with the previously developed LQG regulator performing state estimation with noisy measurements. The motion observed in Figure 6.23 is considerably greater than with the previous disturbance in Figure 6.20, which can be attributed to the larger magnitude disturbance. However, the performance of both controllers is similar, indicating that the Kalman filter estimation is effective for this disturbance, despite being specifically designed to anticipate a different disturbance.

To investigate the sensitivity of the Kalman filter to plant uncertainty, a simulation was performed where the LQG's plant model differs from the actual plant whose dynamics are being simulated. The same noise and disturbance from the previous results (Figure 6.22) were applied to the system. The difference now is that the controller design is based on alternative plant dynamics to the actual plant. The alternative plant model is provided by linearizing the system about an operating point at a configuration that differs from where the controller will be tested. The configuration selected for the alternative model is at a

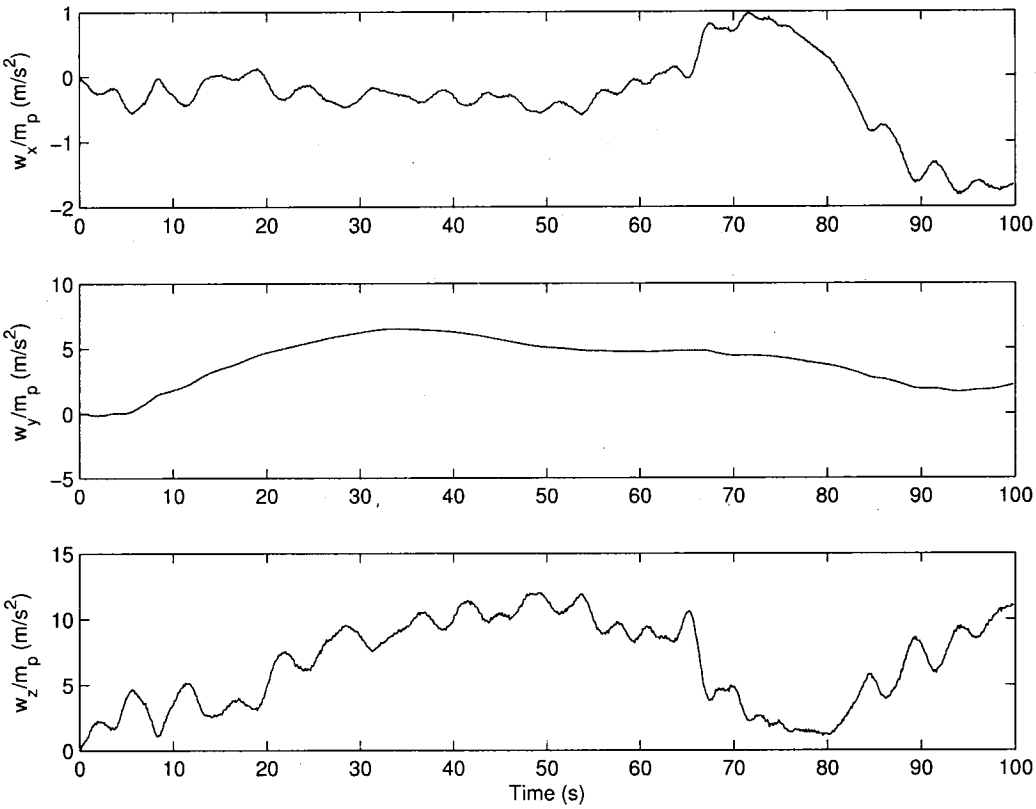

Figure 6.22: Leash disturbance measured during March 11, 2004 flight.

zenith angle of 30° and azimuth angle of 60°, which represents a departure across half the operational workspace from the zero zenith configuration where the controller will be tested. Both elements of the controller design including solving for the optimal gain as in Section 6.3, and the Kalman's filter's internal dynamics, ($\tilde{\mathbf{A}}$ and $\tilde{\mathbf{B}}$, from eq. (6.21) were based on the alternative plant.

The results for a 10-Hz alternative plant LQG controller are given in Figure 6.24 along with the LQR results from the previous plot and the uncontrolled response of the system. As with the previous results with an alternative disturbance, the results with the controller based on an alternative plant gives similar results to the ideal full-state feedback LQR controller. This suggests that the LQG can accommodate a certain level of plant uncertainty. Although not a comprehensive robustness analysis, these results suggest that good performance is possible with unknown disturbances and inexact plant modeling. It should also be

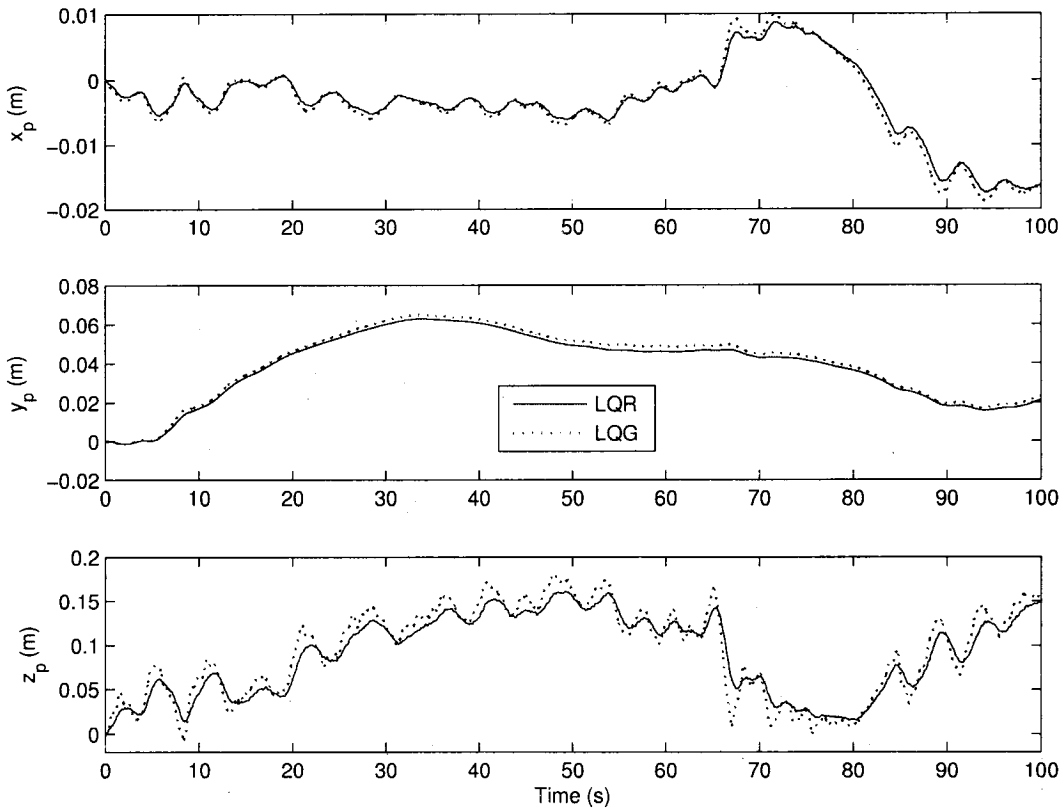

Figure 6.23: Simulation results for 10-Hz optimal controllers; LQR is with full-state feedback and LQG is with Kalman filter estimation without *a priori* knowledge of the March 11 disturbance.

mentioned that the simulations assumed that the use of accurate, low-noise sensors whose noise characteristics were precisely known.

Overall, the LQG optimal control demonstrated its potential to effectively limit platform motion while exhibiting some robustness in the presence of measurement noise, and disturbance and plant uncertainties. Prior to implementing the LQG controller on the actual system, robustness should be investigated thoroughly, as a common drawback of optimal control is its lack of robustness.

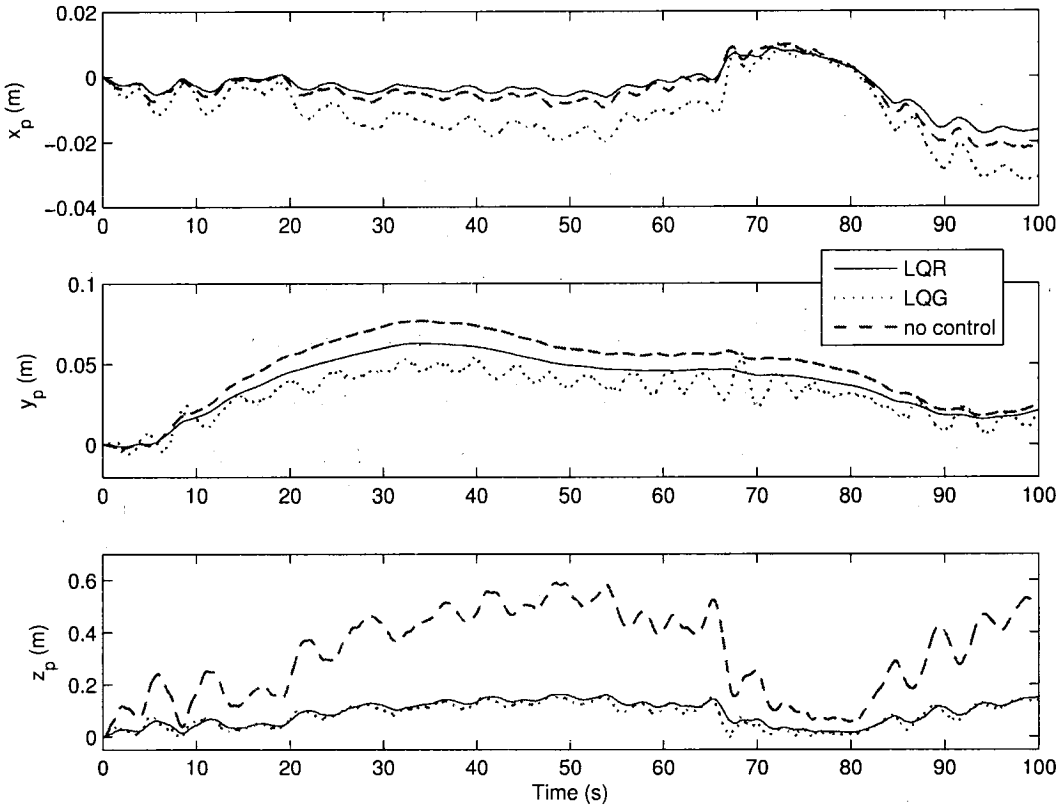

Figure 6.24: Simulation results with March 11 disturbance; LQR is with full-state feedback and LQG is with feedback based on an alternative plant for the system ($\theta_{ze} = 30°$).

6.4 Feedforward Control

Both the field-tested PID controller and the LQG controller tested in the simulation, relied exclusively on feedback of state variables. This has led to satisfactory results in terms of PID and LQG control, but it is possible that other measured quantities can be integrated into the control scheme to further improve the results.

Recognizing that the vast majority of motion disturbances to the platform are caused by the aerostat's leash, whose tension is a measured quantity in the experimental system, leads to the consideration of feedforward control strategies that exploit the knowledge of the disturbance force. Figure 6.25 gives a block diagram of controller that utilizes both feedback and feedforward control elements. The goal of the feedforward controller is to counteract the dynamics introduced by the disturbances. Revisiting the LTI model for the

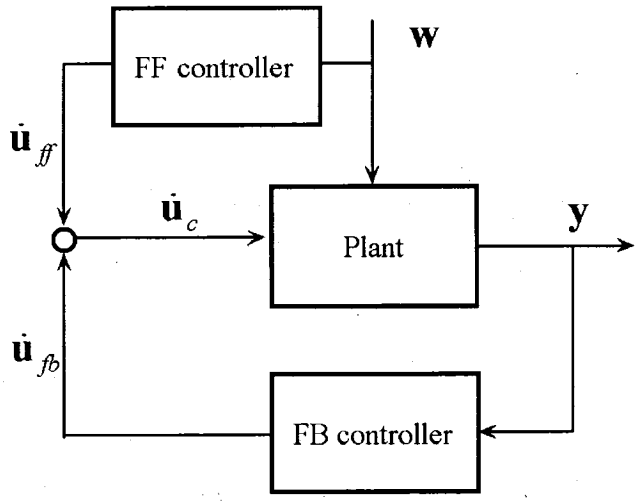

Figure 6.25: Block diagram of control system with feedback and feedforward control input.

system from eq. (6.7)

$$\dot{\tilde{\mathbf{x}}} = \tilde{\mathbf{A}}\tilde{\mathbf{x}} + \tilde{\mathbf{B}}\dot{\mathbf{u}}_c + \tilde{\mathbf{G}}\mathbf{w}$$

$$\mathbf{y} = \tilde{\mathbf{C}}\tilde{\mathbf{x}}$$

it becomes apparent that to completely cancel the disturbance, $\mathbf{w}$, the input $\dot{\mathbf{u}}_c$ must satisfy:

$$\tilde{\mathbf{B}}\dot{\mathbf{u}}_c = -\tilde{\mathbf{G}}\mathbf{w} \tag{6.24}$$

Exact cancellation of the disturbance is not possible for our system because of the non-collocation of the actuators and the disturbance force ($\tilde{\mathbf{B}}$ and $\tilde{\mathbf{G}}$ are sparse matrices that give their respective inputs, $\dot{\mathbf{u}}_c$, and $\mathbf{w}$, direct influence over only a few uncommon states, i.e. $\tilde{\mathbf{B}}$ and $\tilde{\mathbf{G}}$ are both matrices with dimensions of 177×3 that have three non-zero rows each that are not common to both). This is also demonstrated by considering the direct solution of eq. (6.24).

$$\dot{\mathbf{u}}_c = -\tilde{\mathbf{B}}^{+}\tilde{\mathbf{G}}\mathbf{w} \tag{6.25}$$

where $\tilde{\mathbf{B}}^{+}_{3\times 177}$ is a left pseudoinverse of $\tilde{\mathbf{B}}$. The generalized or Moore-Penrose pseudoinverse (which minimizes the least squares solution $\mathbf{x} = \mathbf{A}^{+}\mathbf{b}$ for a system of linear equations described by $\mathbf{Ax} = \mathbf{b}$) does not offer a meaningful solution to eq. (6.25) as it gives $\tilde{\mathbf{B}}^{+}\tilde{\mathbf{G}} = \mathbf{0}$.

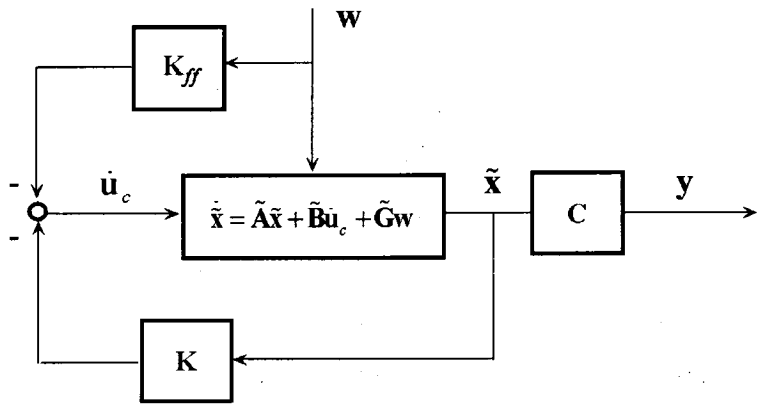

Figure 6.26: Block diagram of control system with feedback and feedforward gain matrices.

An alternative pseudoinverse $\tilde{\mathbf{B}}^+$, proposed by Friedland [86] can be calculated that gives a non-trivial solution to eq. (6.25), which effectively reduces the effects of the disturbance. A typical state-feedback controller is retained for this development to further reduce the effects of the disturbance. Expressing the input, $\dot{\mathbf{u}}_c$, as the sum of both feedforward and feedback control gives:

$$\dot{\mathbf{u}}_c = -\mathbf{K}_{ff}\mathbf{w} - \mathbf{K}\tilde{\mathbf{x}} \tag{6.26}$$

where $\mathbf{K}_{ff}$ is the feedforward gain given by:

$$\mathbf{K}_{ff} = \tilde{\mathbf{B}}^+\tilde{\mathbf{G}} \tag{6.27}$$

and $\mathbf{K}$ is the feedback gain. A block diagram showing the gain matrices is given in Figure 6.26. This controller development assumes the full-state vector, $\tilde{\mathbf{x}}$, is used for feedback, but when implemented it could be the estimated state, $\hat{\mathbf{x}}$. It is also currently assumed that there is no measurement noise, $\mathbf{v} = \mathbf{0}$, but noise will be addressed following the initial controller development.

To solve for $\tilde{\mathbf{B}}^+$ and eventually $\mathbf{K}_{ff}$, it is assumed that the feedback gain, $\mathbf{K}$, is already determined (using optimal or other techniques). The development starts with substituting eq. (6.26) into the state equation.

$$\dot{\tilde{\mathbf{x}}} = \tilde{\mathbf{A}}\tilde{\mathbf{x}} + \tilde{\mathbf{B}}(-\mathbf{K}_{ff}\mathbf{w} - \mathbf{K}\tilde{\mathbf{x}}) + \tilde{\mathbf{G}}\mathbf{w} \tag{6.28}$$

which can be simplified to:

$$\dot{\tilde{\mathbf{x}}} = (\tilde{\mathbf{A}} - \tilde{\mathbf{B}}\mathbf{K})\tilde{\mathbf{x}} - (\tilde{\mathbf{B}}\mathbf{K}_{ff} - \tilde{\mathbf{G}})\mathbf{w} \tag{6.29}$$

The desired controller should attempt to eliminate platform displacement, $\mathbf{y} = \tilde{\mathbf{C}}\tilde{\mathbf{x}} \equiv \mathbf{0}$ and system dynamics $\dot{\tilde{\mathbf{x}}} \equiv \mathbf{0}$. Satisfying both conditions, eq. (6.29) becomes:

$$\tilde{\mathbf{C}}(\tilde{\mathbf{A}} - \tilde{\mathbf{B}}\mathbf{K})^{-1}(\tilde{\mathbf{B}}\mathbf{K}_{ff} - \tilde{\mathbf{G}})\mathbf{w} = \mathbf{0} \tag{6.30}$$

The disturbance, $\mathbf{w}$, can be removed from the equation because the controller should be independent of $\mathbf{w}$, resulting in:

$$\tilde{\mathbf{C}}(\tilde{\mathbf{A}} - \tilde{\mathbf{B}}\mathbf{K})^{-1}(\tilde{\mathbf{B}}\mathbf{K}_{ff} - \tilde{\mathbf{G}}) = \mathbf{0} \tag{6.31}$$

which can be rewritten as:

$$\tilde{\mathbf{C}}(\tilde{\mathbf{A}} - \tilde{\mathbf{B}}\mathbf{K})^{-1}\tilde{\mathbf{B}}\mathbf{K}_{ff} = \tilde{\mathbf{C}}(\tilde{\mathbf{A}} - \tilde{\mathbf{B}}\mathbf{K})^{-1}\tilde{\mathbf{G}} \tag{6.32}$$

Finally, the feedforward gain can be solved for by:

$$\mathbf{K}_{ff} = \left[\tilde{\mathbf{C}}(\tilde{\mathbf{A}} - \tilde{\mathbf{B}}\mathbf{K})^{-1}\tilde{\mathbf{B}}\right]^{-1}\tilde{\mathbf{C}}(\tilde{\mathbf{A}} - \tilde{\mathbf{B}}\mathbf{K})^{-1}\tilde{\mathbf{G}} \tag{6.33}$$

The collection of terms in front of $\mathbf{G}$ is recognized as a left pseudo-inverse of the input matrix, $\tilde{\mathbf{B}}$.

$$\tilde{\mathbf{B}}^{+} = \left[\tilde{\mathbf{C}}(\tilde{\mathbf{A}} - \tilde{\mathbf{B}}\mathbf{K})^{-1}\tilde{\mathbf{B}}\right]^{-1}\tilde{\mathbf{C}}(\tilde{\mathbf{A}} - \tilde{\mathbf{B}}\mathbf{K})^{-1} \tag{6.34}$$

Friedland shows that the matrix $\tilde{\mathbf{C}}(\tilde{\mathbf{A}} - \tilde{\mathbf{B}}\mathbf{K})^{-1}\tilde{\mathbf{B}}$ will possess an inverse if $\tilde{\mathbf{A}}$ is nonsingular and $\left|\tilde{\mathbf{C}}\tilde{\mathbf{A}} - \tilde{\mathbf{B}}\right| \neq 0$ [86]. The specific value of the inverse clearly depends on the feedback gain, $\mathbf{K}$, but the existence of an inverse is independent of $\mathbf{K}$.

6.4.1 Results with Optimal Control

Simulations were performed with the additive feedforward/feedback controller. Initially the optimal gain matrix, $\mathbf{K}$, was based on the same output weighting matrix used in the previous sections ($\mathbf{Q} = 10^6\mathbf{I}_{3\times3}$), but the results required control inputs that exceeded the

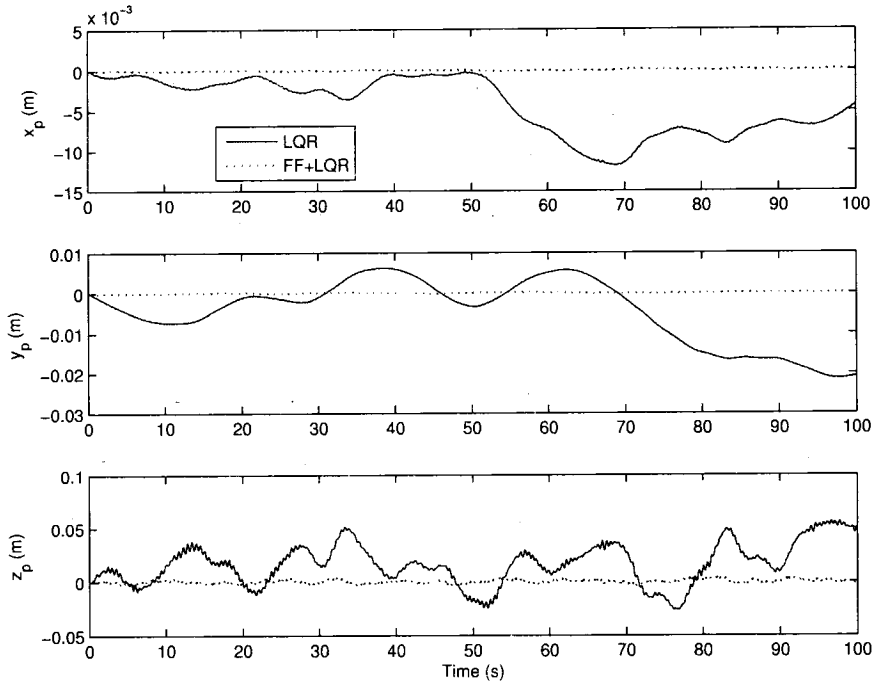

(a)

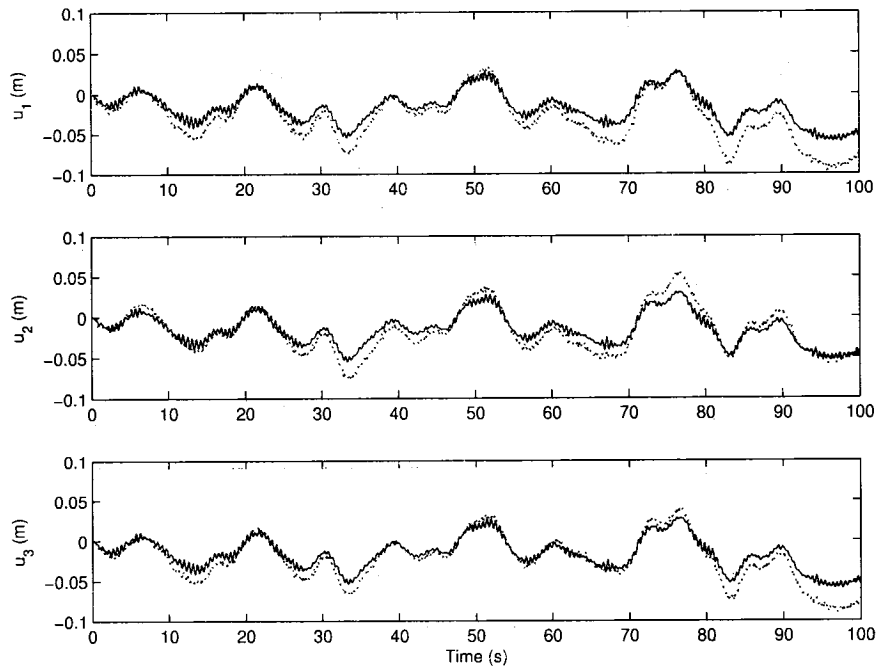

(b)

Figure 6.27: Comparison of simulation results for 10-Hz LQR controllers with and without feedforward input: (a) platform position (b) tether length change from winches.

23 cm/s velocity limits of our winches. Therefore, new gains were found using lighter weighting on the output ($\mathbf{Q} = 10^3\mathbf{I}_{3\times3}$), which produced favourable results without requiring unrealistic winch performance. The feedforward gain matrix, K_{ff}, for this case is:

$$K_{ff} = \begin{bmatrix} 0.112 & 0.048 & -0.220 \\ -0.015 & -0.124 & -0.213 \\ -0.097 & 0.078 & -0.214 \end{bmatrix}$$

The entries of K_{ff} have relevance to the physical layout of the system as the columns relate to the disturbance in the x, y, and z-directions, and the rows relate to the three winch inputs. For example, the large magnitude of the similar entries in the third column suggests that the control inputs of all three winches are most sensitive to vertical disturbances. Also, the large magnitude of the diagonal elements in the first and second rows/columns indicates that winches #1 and #2 will react mostly to disturbances in the x and y-directions respectively, which can be confirmed in the overhead view of the system in Figure 4.1 as winch #1 is near the x-axis and winch #2 is near the negative y-axis.

Figure 6.27 shows results for discrete 10-Hz controllers with and without feedforward winch commands. The platform displacement appears almost nonexistent for the feedforward case relative to the feedback only. The tether displacement is also shown, which shows that the improvement is not due to large amplitude winch inputs. The ringing observed in the control input and the platform's vertical position is also significantly reduced with the feedforward case. Results are summarized in Table 6.5 for various 10-Hz controllers. The displacement for each case is approximately an order of magnitude smaller than the noise-free LQG results reported in Table 6.4.

Although the extraordinary precision observed during the simulations of the feedforward/feedback controller is not likely realizable in practice due the full-state feedback assumption and unmodeled effects such as sensor noise and time delays, the results suggest that millimeter-level precision is approachable with the mechanical components of the aerostat positioning system.

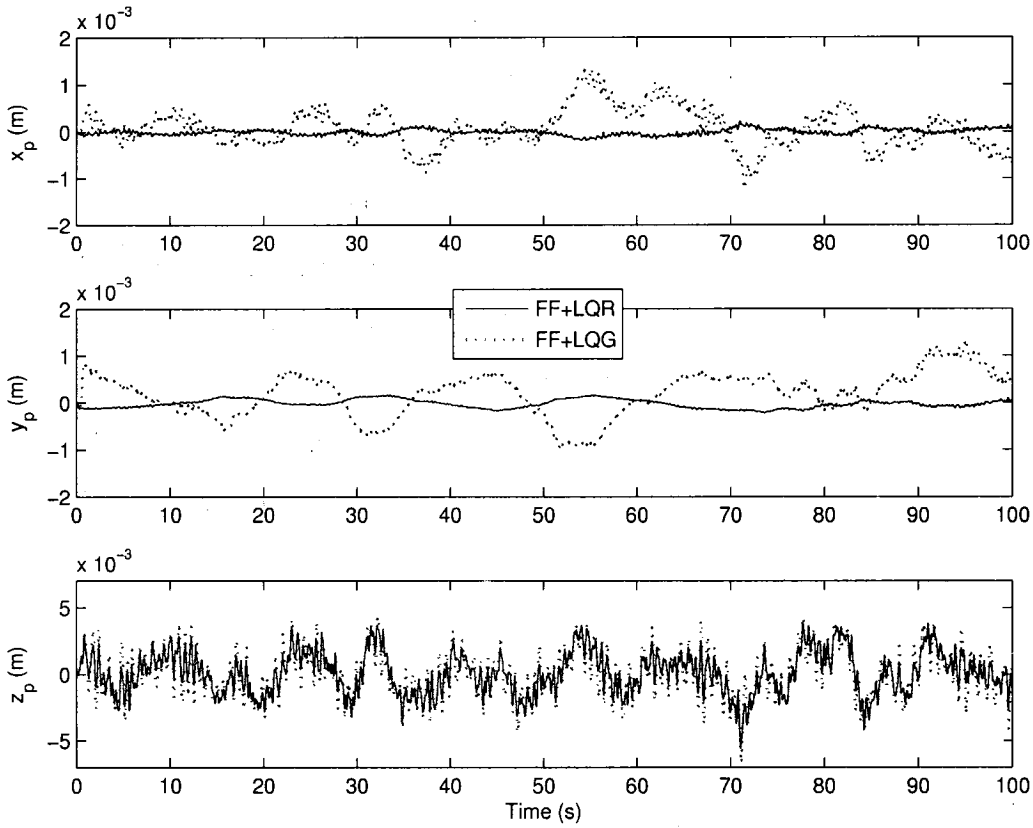

Figure 6.28: Simulation results for feedforward/feedback LQR and LQG controllers at 10 Hz.

Results with LQG Feedback

Adding the feedforward controller to the more practical LQG feedback controller that involves state estimation adds complexity and uncertainty to the control process. The state estimation performed by the Kalman filter requires inherent knowledge of the feedforward gain in its plant model of the system. The state equation of eq. (6.29) with feedforward and feedback components can be re-written as follows:

$$\dot{\tilde{\mathbf{x}}} = \tilde{\mathbf{A}}\tilde{\mathbf{x}} + \tilde{\mathbf{B}}\dot{\mathbf{u}}_{fb} + (\tilde{\mathbf{G}} - \tilde{\mathbf{B}}\mathbf{K}_{ff})\mathbf{w} \tag{6.35}$$

The matrix $(\tilde{\mathbf{G}} - \tilde{\mathbf{B}}\mathbf{K}_{ff})$ must replace the $\tilde{\mathbf{G}}$ matrix that leads to $\tilde{\mathbf{G}}^*$ in the Kalman filter's state-space description of the plant, i.e. eq. (6.21).

Simulations were performed for the feedforward/LQG system with the appropriate

Controller	v = 0	σ_x	σ_y	σ_z	x_{max}	y_{max}	z_{max}
FF + LQR	Yes	0.06	0.1	1.6	0.2	0.2	5.6
LQG	No	3.4	7.9	19.9	11.7	21.3	57.9
FF + LQG	No	0.4	0.5	1.7	1.3	1.3	6.7
PID	No	1.8	3.3	37.7	5.3	7.7	92.4
FF+PID	No	0.8	1.1	6.8	2.9	3.3	20.3

Table 6.5: Summary of standard deviation and maximum displacements (in mm) for various 10-Hz feedforward + feedback controllers.

state-space model of the system within the Kalman filter. Results are given in Figure 6.28 for 10 Hz-controllers that compare the LQG results, with the same measurement noise used in Section 6.3.5, to the LQR results of the previous section. A summary of the results are provided in Table 6.5. The measurement noise and state estimation is observed to decrease the controller's performance, but the results are encouraging as sub-centimeter precision is achieved. This is approximately a five-fold increase over previous results with LQG feedback only for the same disturbance and noise (Figure 6.20), which limited the platform position to deflections of less than 5 cm.

6.4.2 Results with PID Control

Although the feedforward controller, $\mathbf{K}_{ff}$, was developed specifically for controllers using full-state feedback with the gain matrix, $\mathbf{K}$, the advantages of using the feedforward input in conjunction with PID feedback was also investigated. Initially the same feedforward gain, $\mathbf{K}_{ff}$, from eq. (6.27) and the same PID gains from Section 6.3.4 ($K_P = 0.4\ s^{-1}, K_I = 0.05\ s^{-2}, K_D = 0.05$) were used and it was observed that the PID feedback was not sufficiently responsive to compensate for the feedforward input. Therefore, alternative feedforward gains were determined that anticipate a less responsive feedback controller. This was achieved by altering the output weighting, $\mathbf{Q}$ of the LQR objective function of eq. (6.9) in search of a suitable $\mathbf{K}_{ff}$ for the PID feedback. Reducing the output weighting relative to the input leads to a less responsive feedback controller, which in turn results in a feedforward gain, $\mathbf{K}_{ff}$, that expects less from the feedback input. Using an output

weighting matrix of $\mathbf{Q} = 10^2\mathbf{I}_{3\times3}$ produced a $\mathbf{K}_{ff}$ that worked well with this PID controller, which is:

$$K_{ff} = \begin{bmatrix} 0.068 & 0.029 & -0.149 \\ -0.009 & -0.077 & -0.144 \\ -0.059 & 0.048 & -0.145 \end{bmatrix}$$

The pattern is similar to the K_{ff} for the optimal control, but the magnitudes of the entries are reduced.

This heuristic controller design process is able to produce favourable simulation results, but it should be noted that it is achieved by calculating a feedforward gain based on a fictitious optimal feedback controller. It is likely that the feedforward gain could be better tuned if the actual characteristics of the PID controller were incorporated in the calculation of $\mathbf{K}_{ff}$, however, this calculation becomes complicated because the PID feedback involves a nonlinear equation of the state variables for platform position, see eqs. (3.23) and (3.24). Instead of attempting to include the PID controller when determining $\mathbf{K}_{ff}$, results are presented which demonstrate the effectiveness of combining the heuristically tuned feedforward gains with PID feedback.

Figure 6.29 gives PID results at 10 Hz with and without feedforward input and a summary of the results is included in Table 6.5. For these results measurement noise was added to the feedback ($\mathbf{v} \neq \mathbf{0}$) as in the previous sections. The platform displacement is clearly smaller with feedforward control and again the improvement is not due to large amplitude tether length variations. The feedback-only winch input lags the much quicker feedforward controller, which explains the difference in performance. The maximum winch tether speed is higher in the feedforward case but at 10 cm/s it is well below the 23 cm/s limit. The results for the feedforward PID results and the feedforward LQG results are similar in the horizontal directions, but vertically the optimal feedback outperforms the PID by more than a factor of three.

Although the PID with feedforward control does not match the precision of the optimal feedback/feedforward controllers, the PID remains attractive for several reasons. It is easy to implement, insensitive to modeling errors, and it is easier to tune and readapt if problems with the controller are encountered in the field. It was demonstrated that exploiting the

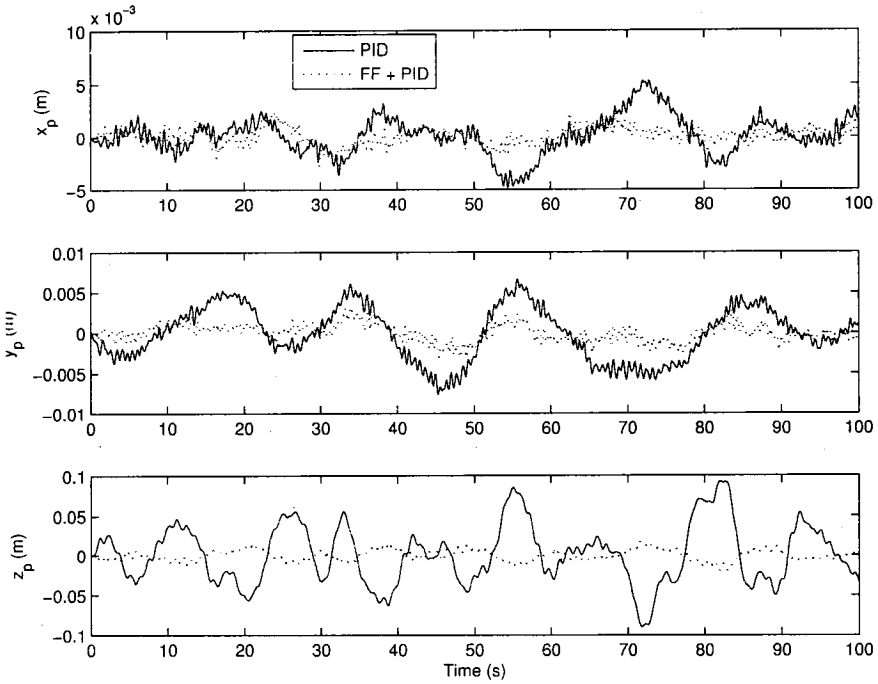

(a)

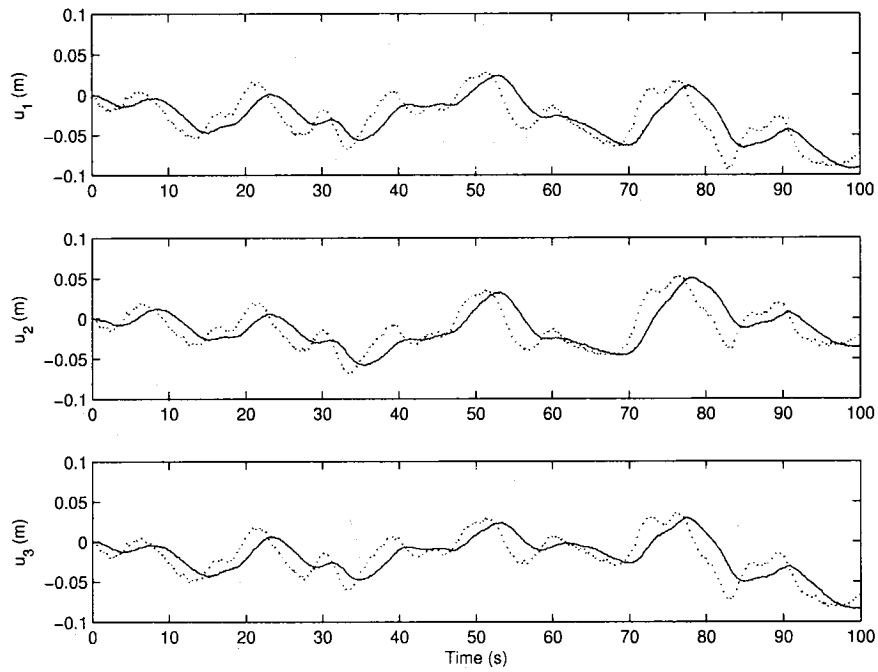

(b)

Figure 6.29: Comparison of simulation results for 10-Hz PID controllers with and without feedforward input (a) Platform position (b) Tether length change from winches.

readily available knowledge of the primary disturbing force, the aerostat leash tension, in the form of an additive feedforward component to the control input has the potential to drastically improve the performance of the controller and the overall positioning system.

6.5 Covering the Operational Workspace

For a fully operational telescope, the platform/receiver traverses set trajectories along a hemisphere at a very slow rate (equivalent to the Earth's rotation rate when tracking a celestial object). Because of the slow trajectory following, the control problem within the context of this study has applied exclusively to regulating the output about a fixed point, instead of tracking a specified trajectory.

Thus far, all controller development and analysis in this chapter has focused on only one location within the desired workspace for the 3-dof positioning system. The central, symmetric, or zero zenith configuration is the natural starting point for analysis, however, it is imperative to verify the extent to which controllers developed for this configuration apply to other fixed points within the desired workspace. To accomplish this, a controller will first be developed at the extreme zenith angle based on a LTI model about that point. Next, controllers will be tested at locations other than their equilibrium point to assess the controller sensitivity to changes in configuration.

6.5.1 Extreme Zenith Angle

For the experimental closed-loop system the maximum zenith angle achieved was 50°, which is less than the desired 60° zenith workspace because the base winch radius in the field was 364 m instead of 400 m. To maintain consistency with all the previous closed-loop results, both experimental and simulated, the extremity of the workspace will be considered at $\theta_{ze} = 50°$ with the assumption that results here can be applied to $\theta_{ze} = 60°$ with a base radius of 400 m.

It is understood that the system at high zenith angles is more challenging to control than at the zenith as its stiffness is reduced. As observed in the experimental results, the

Controller	σ_x	σ_y	σ_z	x_{max}	y_{max}	z_{max}
none	9.4(4.2)	21.3(9.7)	118(66.1)	24.8(14.3)	54.5(26.3)	324(189)
PID 10 Hz	5.0	9.9	67.7	12.0	26.0	169
FF+PID 10 Hz	2.8	10.1	12.3	6.9	28.2	30.0
LQG 10 Hz	2.9	9.3	21.9	9.6	23.5	56.8
FF+LQG 10 Hz	0.5	0.5	2.0	1.5	1.5	7.2

Table 6.6: Summary of standard deviation and maximum displacements (in mm) for discrete controllers with system at $\theta_{ze} = 50°$ controllers (values in brackets are for uncontrolled case at $\theta_{ze} = 0°$).

platform motion is significantly larger when $\theta_{ze} = 50°$. Simulations were performed at $\theta_{ze} = 50^o$, $\theta_{az} = 60°$ (which was previously found to be among the configurations with the worst performance [24]) with the identical May 27 disturbance force. For the uncontrolled response, the platform position approximately doubled the previous results at $\theta_{ze} = 0°$. Figure 6.30 gives the time history of the passive or uncontrolled response and shows the improvement with 10-Hz LQG feedback. Table 6.6 compares the uncontrolled response at the two configurations and also the controlled response including PID and LQG feedback control and feedback/feedforward control. Both the feedback gain, $\mathbf{K}$, and the feedforward gain, $\mathbf{K}_{ff}$, were recalculated using the linear model obtained at this high zenith configuration. The PID feedback gains are unchanged from previous sections. Attempts were made during several high-zenith flight tests to obtain more appropriately-tuned gains, but these efforts were unsuccessful. Because the effectiveness of the PID feedback control is weaker at higher zenith angles, the feedforward gain used with the PID controller had to be designed with a more lightly weighted matrix $\mathbf{Q}$ ($\mathbf{Q} = \mathbf{I}_{3\times3}$ instead of $\mathbf{Q} = 10^2\mathbf{I}_{3\times3}$ used previously).

The effectiveness of the feedback/feedforward combination is demonstrated at this configuration as considerable motion reduction is achieved with both PID and LQG feedforward control over their feedback only counterparts. The feedforward/LQG controller nearly matches its precision at $\theta_{ze} = 0°$ from Table 6.5, whereas the feedforward/PID results are weaker at this high zenith angle, especially in the y-direction. The weaker performance of the feedforward/PID control arises from its less effective feedback control

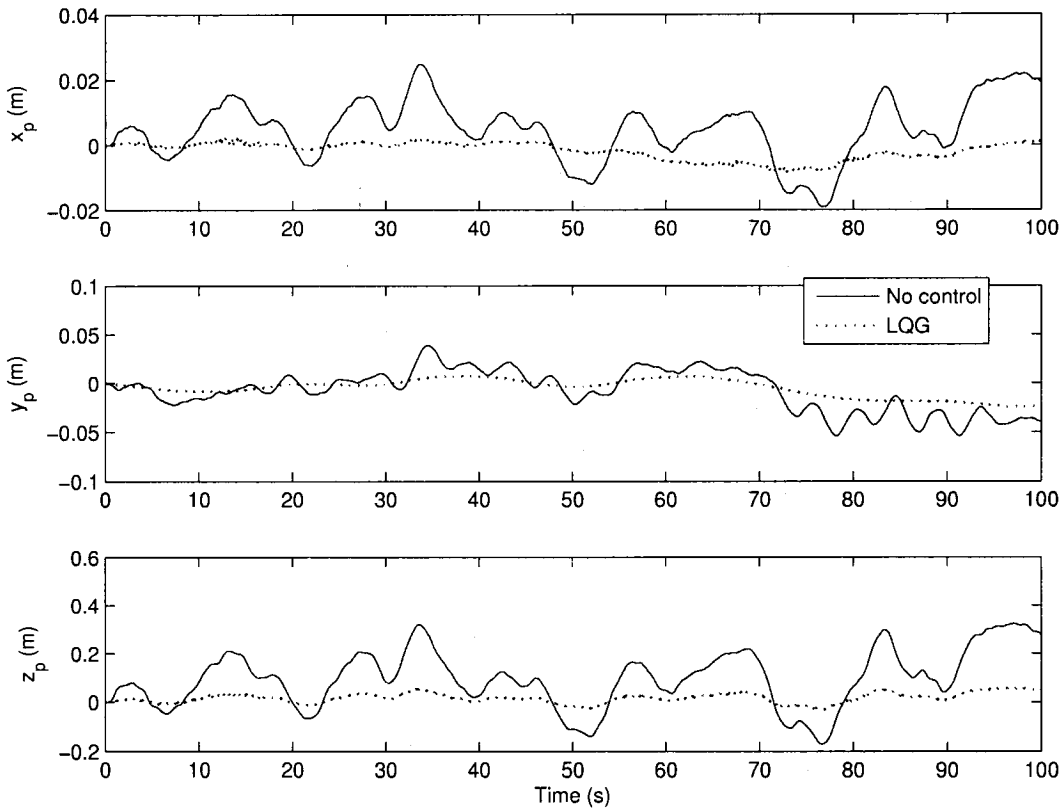

Figure 6.30: Comparison of simulation results for uncontrolled response and 10-Hz LQG feedback for system at $\theta_{ze} = 50°$.

and less aggressive feedforward gains. Overall, this analysis shows that the system has the ability to achieve sub-centimetre precision at the edge of the workspace despite an inherent loss of stiffness.

6.5.2 Non-Local Controller

The effectiveness of a locally designed controller at the center and edge of the workspace has been established. However, because there are infinite workspace locations and the system may pass through a large number of them, albeit slowly, while following a trajectory, it is essential to quantify the relative size of the region at which a locally developed controller is valid or effective. One example of using a controller based on a non-local linear model was provided in Section 6.3.5 when plant uncertainty was investigated.

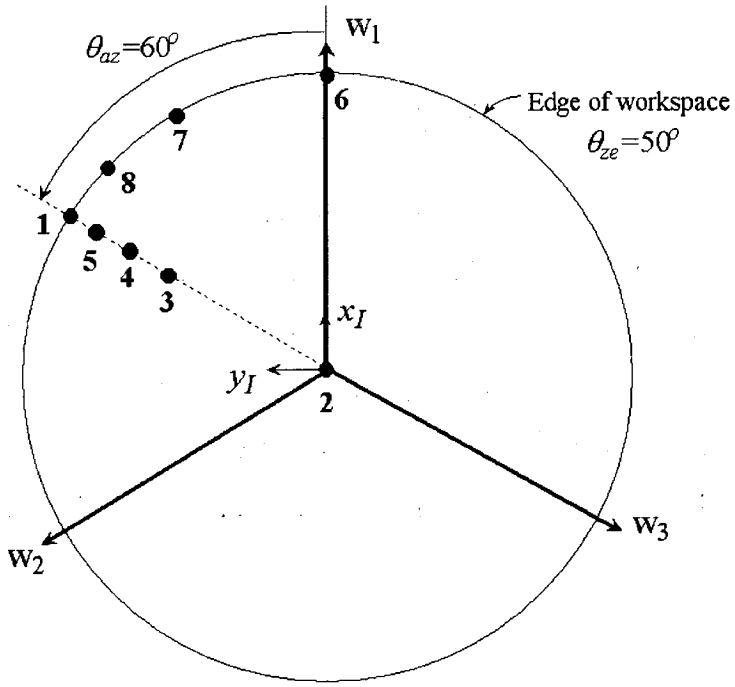

Figure 6.31: Overhead view of the LAR workspace with the eight locations of locally developed controllers.

Stability can be assessed with a non-local optimal controller from the eigenvalues of the modified state matrix $\mathbf{A}'$, given by:

$$\mathbf{A}' = \tilde{\mathbf{A}}_1 - \tilde{\mathbf{B}}_1 \mathbf{K}_2 \tag{6.36}$$

where $\tilde{\mathbf{A}}_1$ and $\tilde{\mathbf{B}}_1$ are the local state-space matrices and $\mathbf{K}_2$ is an optimal feedback gain based on an LTI model linearized about a different operating point. When the local LTI system is the symmetric configuration at $\theta_{ze} = 0°$, and the feedback gain is based on the LTI model at the extreme zenith angle, $\theta_{ze} = 50°$, or vice versa, all the real parts of the eigenvalues of $\mathbf{A}'$ have negative real parts. Although not a rigourous proof, by exchanging controllers with two local systems representing the minimum and maximum zenith angles, this may imply that any local LQG can be applied anywhere within the workspace without inducing instability.

Multiple simulations were performed at the extreme zenith, $\theta_{ze} = 50°$, $\theta_{az} = 60°$ configuration with optimal LQG feedback with gains based on LTI models at several other

Case	θ_{ze}(deg)	θ_{az}(deg)	σ_x	σ_y	σ_z	x_{max}	y_{max}	z_{max}
1	50	60	2.9	9.3	21.9	9.6	23.5	56.8
2	0	-	4.6	17.4	28.4	11.4	52.3	86.4
3	30	60	3.6	13.2	29.7	10.2	41.6	89.4
4	40	60	3.2	11.3	27.2	9.6	34.7	78.2
5	45	60	3.0	10.1	25.3	9.3	29.0	73.6
6	50	0	4.9	19.9	25.1	17.2	72.7	75.1
7	50	30	3.6	15.0	27.0	10.8	48.5	76.7
8	50	50	2.7	11.1	25.2	9.4	14.5	79.9

Table 6.7: Summary of standard deviation and maximum displacements (in mm) for 10-Hz LQG controllers designed at various locations and implemented at the operating point of $\theta_{ze} = 50°$, $\theta_{az} = 60°$).

locations within the workspace. The locations of the local controllers are given in Figure 6.31, which gives an overhead view of the workspace. Table 6.7 summarizes the results. All the controllers tested are generally better at limiting vertical motion, which had a maximum value of 324 mm with no control, than horizontal deflections, which had a maximum value of 25 mm and 55 mm in the respective x and y directions (see Table 6.6). Not surprisingly, the best performance, apart from the actual local controller of Case 1, is observed with controllers designed at configurations nearest to the operating point–Cases 5 and 8. This trend continues with the performance deteriorating as the local controllers deviate further from the operating point, culminating in the worst performance at the furthest locations of Case 2 and Case 6.

These results suggest that some type of adaptive controller is necessary to achieve good precision while traversing the workspace. One possible approach, termed gains scheduling, involves using different gains depending on the location of the platform. The results in Table 6.7 indicate that for favourable results, controllers should be applied while the system is within 5 to 10° of its design point.

6.6 Implementation Issues / Options

The study and design of controllers for the LAR positioning system has revealed several potential approaches to improve performance beyond the PID controller tested in the field. However, some of the most significant improvements are not only due to a superior algorithm, but also to improved sensor bandwidth and to making better use of existing sensors. The control strategies investigated can be separated into two paths in terms of complexity and potential payoff.

The first option requires less effort both computationally and in terms of new hardware as it involves modifying the existing PID controller to include feedforward input. Current sensors can be used and the PID algorithm only needs a few lines of code to accommodate the feedforward gain multiplication. The plots in Figure 6.29 show that the combined controller responds more quickly to disturbances resulting in enhanced precision. The strength of this approach stems from the combination of the PID's ease of implementation and the predictive qualities of the feedforward term which utilizes the dynamics model of the system. The drawbacks are related to the heuristic nature of the control development and to the PID controller's known performance limitations.

The second option involves LQG regulators which demonstrated encouraging precision and some robustness in response to plant uncertainty. The optimal feedback controller was also shown to benefit from feedforward input based on measured leash tension. The accuracy and bandwidth of the position measurements limits the performance of the control system. Depending on available resources and the required precision of the positioning system, an instrumentation upgrade involving replacing the GPS measurement system may be suitable for future developments. For instance, ground-based laser measurements systems offer superior bandwidth and accuracy over GPS, though they may also be more sensitive to weather conditions.

Chapter 7

Conclusions

The focus of this work is the study of a novel tethered aerostat position system, which is specialized for the operation of the large-scale LAR radio telescope. The study encompasses comprehensive dynamics modeling, experimental demonstrations with model validation, and advanced state-space controller development and analysis.

The experimental testing facility, built at one-third scale of the LAR telescope, was constructed to test the accuracy of the positioning system and verify our computational model. The dynamics model of the multi-tethered system was achieved by discretizing the tethers into a series of lumped-masses and estimating the aerodynamic properties of each of the physical elements, such as the aerostat, the tethers and the payload. The disturbance to the model is provided by a turbulent wind input with specified gust properties. A control system was included in the model that uses position feedback to actively adjust the length and mass properties of the discrete tether element nearest to the ground.

A series of experimental flight tests were conducted over a two-year period to determine the precision of the aerial positioning system and the reliability of the dynamics model. Both the experimental testing program and the simulation validation can be divided into passive and active results. The initial flight tests, analysis, and validation involved fixed tether lengths to study the passive response of the system. The second round of testing involved active tether control achieved with the ground-based winches operation with a PID controller using position feedback.

The effectiveness of the passive tripod structure in limiting motion of an airborne pay-

load was demonstrated experimentally as the horizontal platform motion was as much as two orders of magnitude smaller than the ensuing motion of the aerostat (approx. 10 m for the aerostat and 10 cm for the platform). The stiffness of the system decreased when the system was configured for higher zenith angles, but the stiffness improved when the tethers were spread out radially.

The passive components of the dynamics model such as lumped-mass tethers, the aerostat aerodynamics and the wind model, were assessed by comparing simulated results to experimental measurements. Initially the comparison involved only the tether model as the leash force measured during flights tests replaced the simulated disturbance of the aerostat in response to the wind. The predicted motion of the tether model was shown to have excellent agreement with the measured motion, and confidence in the tether model was established. Validation of the aerostat and wind model was only achieved at a statistical level because our recreation of the wind disturbance was only a statistical approximation of the actual wind field. Overall, the passive model corresponded well to the measurements as the standard deviation of the simulated platform position was estimated to within 3 cm of the measured response. Considering the large scale of the system, the results create an adequate level of confidence that the model is capable of predicting realistic behaviour for a general wind condition. To demonstrate the utility of a validated dynamics model as a design tool, simulations were performed to evaluate the relative effectiveness of a streamlined and spherical for the LAR system. The comparison showed that the spherical aerostat, despite its much higher drag forces, results in smaller platform deflections.

For the second round of testing, computer-controlled winches were installed and operated in both open and closed-loop. The open-loop tests consisted of applying sinusoidal winch inputs over a range of frequencies while measuring the platform position as the output to create a Bode diagram for the system. The closed-loop tests were performed by actuating the winches according to simple PID feedback of the position error of the platform. This regulator-type control was designed to limit the platform motion about any specified location within the operational workspace of the positioning system. The platform's posi-

tion was measured using differential GPS at a rate of 10 Hz, which limited the PID control frequency to 10 Hz as well. The closed-loop response of the system was encouraging as the standard deviation of the platform motion was between 45% to 69% lower than uncontrolled tests performed at various geometric configurations within the workspace. The precision achieved with the positioning system over a range of tests in terms of RMS error was less than 5 cm horizontally and less than 10 cm vertically. It was also observed that the system was susceptible to a vertical bounce mode near 0.15 Hz that occasionally led to instabilities when gains were tuned aggressively.

The validation of the active or controlled behaviour of the system was conducted for both open and closed-loop control. For the open-loop response, the input/output relationship of a linear version of the dynamics model compared favourably to the experimental Bode diagram. Next, the closed-loop model was validated by subjecting the payload to the actual measured leash force disturbance and comparing the predicted behaviour to the measured response. The simulation results correspond well to the measurements in both the time and frequency domain; the maximum discrepancy between the standard deviation of the simulated and measured platform position in any direction is 15 mm. The complete dynamics model was used in a second design analysis which evaluated the advantages of changing the radius of the tether's ground terminations and increasing the number of tethers beyond three. This analysis concluded that using six tethers and a reduced winch perimeter radius of 240 m, the mean error could be reduced by an order of magnitude relative to using three tethers. As the LAR radio telescope design advances, the model will be an important tool in fine-tuning important design variables and controllers.

To improve on the closed-loop performance of the basic PID controller tested in the field, various control strategies with potential to exploit our validated dynamics model were investigated. Optimal control was the focus of the analysis as LQG regulators were developed and applied in simulation to linear state-space versions of our dynamics model. The LQG controller was observed to approximately double the precision of the system compared to PID control, but the LQG design procedure is far more complex and assumes

relatively accurate models of the system, disturbance and sensor noise are available. A limited robustness analysis showed that the LQG's performance was only modestly affected by model uncertainty. Simulations also showed that the effectiveness of both the PID and LQG significantly improved if the control frequency was increased from 10 Hz to 100 Hz, suggesting that for future tests an upgrade in sensor bandwidth should be considered.

To take advantage of measurable quantities that are not state variables, a feedforward control scheme was developed that utilizes the measured tension in the aerostat's leash. It was previously known that the vast majority of the exogenous disturbances felt by the platform were transmitted through the leash. Therefore, the measured disturbance was incorporated with the feedback control system by adding a feedforward term to the winch input. The feedforward term consists of the disturbance vector multiplied by a control gain, which is calculated based on the linear model of the closed-loop system. The feedforward input was applied to both PID and LQG feedback control systems and exceptional results were observed. For PID control, the RMS platform error for the system in the symmetric configuration dropped from approximately 4 cm to less than 1 cm, while with LQG the RMS error dropped from about 2 cm to to 2 mm.

Most of the control system design and analysis focused on the system in the symmetric configuration, but simulations were also performed at the extreme zenith angles at the edge of the workspace, where the system is inherently less stiff. The feedforward/LQG controller was nearly able to match its precision at the symmetric configuration, but the precision of the feedforward/PID controller decreased by approximately 50% at the extreme zenith angle. To consider the need for some type of adaptive control to achieve control during tracking, several controllers designed at various locations within the workspace were tested during operation at the extreme zenith angle. The results showed that the best results were obtained when the controller applied was within 5 to 10° of the extreme zenith operationg point, suggesting that some form of adaptive control is required to achieve high precision while traversing the workspace.

7.1 Recommendations for Further Research

Extending from the study presented in this work, several avenues have been identified for future research.

- Although the total dynamics model was satisfactorily validated against experimental data, a certain level of uncertainty persists with the wind model and the aerostat model due to incomplete wind data. To overcome this limitation, efforts should be made to obtain wind measurements closer to the aerostat and in all three directions, not just the horizontal components. With a better understanding of the characteristics of the wind disturbance, a more detailed and precise model validation process could be performed.

- Simulation results in Chapter 4 suggest that a spherical aerostat should outperform a streamlined aerostat for this type of tethered positioning system, however, efforts should be made to test this hypothesis in the field. Uncertainty related to the vortex shedding behaviour and the aerodynamic drag of a tethered sphere suggest that the aerostat should be tested with the system before definitive claims of its superiority over the streamlined aerostat can be asserted.

- The controller development for the tethered positioning system is still in a premature stage. Benefits and limitations of a PID and optimal controllers were documented, however, several other control strategies should be investigated for this application. Because of the known variability of the plant over the workspace, an adaptive or a linear parameter varying controller could prove effective. Robustness was only superficially addressed in this work although it is an important consideration for any practical control system. Prior to implementation in the filed, a robustness analysis should be performed and depending on the outcome, synthesis of a robust controller could be considered.

- To accomplish the tracking maneuvers required by the operational telescope, the tether actuation model in this work, which involves changing the parameters of

only one discretized element, must be modified to accommodate larger variations in length. Also with respect to tracking maneuvers, adaptive control strategies such as gain scheduling should be evaluated since tracking represents a significant departure from the regulator-type control of this study.

- The results in Chapter 6 clearly show that performance of the system can be improved not only by changing the control algorithms, but also by increasing the sampling frequency of the feedback variables. Therefore, upgrades to the sensors and instrumentation should be considered prior to any future testing of the scaled experimental system.

- The advantages of increasing the number of tethers from three to six should be studied further, preferably at both theoretical and experimental levels. The dynamics behaviour of the system becomes much more complex when tethers are added and the platform is modeled as a rigid body instead of a point mass, and any modeling of the system should be checked against measured tests.

Bibliography

[1] R. Leclaire and C. Rice, "The local motions of a payload supported by a tritethered natural shape balloon," *US Air Force Report AFCRL-TR-73-0748*, December 1973.

[2] M. Nahon, "Dynamics and control of a novel radio telescope antenna," in *AIAA Modeling and Simulation Technologies Conference and Exhibit*, Portland, OR, August 1999, pp. 214–222.

[3] M. Nahon, G. Gilardi, and C. Lambert, "Dynamics and control of a radio telescope receiver supported by a tethered aerostat," *AIAA Journal of Guidance, Control, and Dynamics*, vol. 25, no. 6, pp. 1107–1115, 2002.

[4] T. Legg, "A proposed new design for a large radio telescope," *Astronomy and Astrophysics Supplement Series*, vol. 130, no. 4, pp. 369–379, 1998.

[5] B. Carlson, L. Bauwens, L. Belototski, E. Cannon, Y. Deng, P. Dewdney, J. Fitzsimmons, D. Halliday, K. Krschner, G. Lachapelle, D. Lo, P. Mousavi, M. Nahon, L. Shafai, S. Stiemer, R. Taylor, and B. Veidt, "The large adaptive reflector: A 200-m diameter, wideband, cm-wave radio telescope," in *Radio Telescopes-Proc. of SPIE Meeting 4015*, Bellingham, WA, 2000, pp. 33–44.

[6] J. Fitzsimmons, B. Veidt, and P. Dewdney, "Steady-state stability analysis of the multi-tethered aerostat platform for the large adaptive reflector telescope," in *Proc. of SPIE International Symposium on Astromical Telescopes and Instrumentation*, Munich, Germany, March 2000, pp. 476–487.

[7] E. Young, "Tethered balloons: Present and future," in *AIAA Aerodynamic Deceleration Systems Conference*, El Centro, CA, September 1968.

[8] L. Bairstow, E. Relf, and R. Jones, "The stability of kite balloons: Mathematical investigation," *British Aeronautical Research Council*, no. RM 208, December 1915.

[9] J. DeLaurier, "Prediction of tethered-aerostat response to atmospheric turbulence," *AIAA Journal of Aircraft*, vol. 14, no. 4, pp. 407–409, 1977.

[10] ——, "A stability analysis for tethered aerodynamically shaped balloons," *AIAA Journal of Aircraft*, vol. 9, no. 9, pp. 646–651, 1977.

[11] T. Redd, R. Bland, and R. Bennett, "Stability analysis and trend study of a balloon tethered in a wind, with experimental comparisons," *NASA TN D-7272*, pp. 1–109, 1973.

[12] S. Jones and J. Krausman, "Nonlinear dynamics simulation of a tethered aerostat," *AIAA Journal of Aircraft*, vol. 19, no. 8, pp. 679–686, 1982.

[13] S. Jones, "Nonlinear dynamic simulation of a moored aerostat," in *Proc. of the 7th AIAA Lighter-Than-Air Systems Technology Conference*, Monterey, CA, August 1987, pp. 72–77.

[14] S. Badesha and S. P. Jones, "Aerodynamics of the TCOM 71m aerostat," in *Proc. of the 10th AIAA Lighter-Than-Air Systems Technology Conference*, Scottsdale, AZ, September 1993, pp. 36–42.

[15] S. Jones and L. Schroeder, "Nonlinear dynamics simulation of a tethered aerostat: A fidelity study," *AIAA Journal of Aircraft*, vol. 38, no. 1, pp. 64–68, 2001.

[16] K. Stanney and C. Rahn, "Response of a tehtered aerostat to simulated turbulence," *Communications in Nonlinear Science and Numerical Simulation*, vol. 11, no. 6, pp. 759–776, 2005.

[17] B. Etkin, "Stability of a towed body," *AIAA Journal of Aircraft*, vol. 35, no. 2, pp. 197–205, 1998.

[18] F. Zhu and C. Rahn, "Stability analysis of a circularly towed cable-body system," *Journal of Sound and Vibration*, vol. 217, no. 3, pp. 435–452, 1998.

[19] P. Williams and P. Trivailo, "Study on the transitional dynamics of a towed-circular aerial cable system," in *Proc. of the AIAA Atmospheric Flight Mechanics Conference*, San Franscisco, CA, August 2005.

[20] S. Oh, K. Pathak, and S. Agrawal, "Autonomous helicopter landing on a moving platform using a tether," in *Proc. of the IEEE International Conference on Robotics and Automation*, Barcelona, Spain, April 2005, pp. 3960–3965.

[21] M. A. Masterskikh, "A method for holding a pilot balloon or light aerostat at a predetermined height for meteorological observations," *Meteorologiya I Gidrologiya*, vol. 4, pp. 102–104, 1978.

[22] B. Veidt and P. Dewdney, *Steady-State Stability Analysis of a Triple Tethered Balloon Platform.* DRAO Future Radio Facilities Report 1, 1996.

[23] C. Lambert, A. Saunders, C. Crawford, and M. Nahon, "Design of a one-third scale multi-tethered aerostat system for precise positioning of a radio telescope receiver," in *Canadian Aeronautics and Space Institute Flight Mechanics and Operations Symposium*, Montreal, QC, April 2003.

[24] C. Lambert, "Dynamics modeling and conceptual design of a multi-tethered aerostat system," M.A.Sc. Thesis, University of Victoria, Vicotria, British Columbia, Canada, 2002.

[25] C. Lambert and M. Nahon, "Stability analysis of a tethered aerostat," *AIAA Journal of Aircraft*, vol. 40, no. 4, pp. 705–715, 2003.

[26] X. Zhao, "Statics and dynamics simulation of a multi-tethered aerostat system," M.A.Sc. Thesis, University of Victoria, Victoria, B.C., 2005.

[27] H. L. Coroller, J. Dejonghe, C. Arpesella, D. Vernet, and A. Labeyrie, "Tests with a carlina-type hypertelescope prototype," *Astronomy and Astrophysics*, vol. 426, no. 2, pp. 721–728, 2004.

[28] J. Albus, R. Bostelman, and N. Dagalakis, "The NIST robocrane," *Journal of Robotic Systems*, vol. 10, no. 5, pp. 709–724, 1993.

[29] R. Roberts, T. Graham, and T. Lippit, "On the inverse kinematics, statics, and fault tolerance of cable-suspended robots," *Journal of Robotic Systems*, vol. 15, no. 10, pp. 581–597, 1998.

[30] C. Kossowski and L. Notash, "Cat4 (cable actuated truss-4 degrees of freedom): A novel 4 dof cable actuated parallel manipulator," *Journal of Robotic Systems*, vol. 19, no. 12, pp. 605–615, 2002.

[31] S. Oh, K. Mankala, and S. Agrawal, "Dynamic modeling and robust controller design of a two-stage parallel cable robot," *Multi Body System Dynamics*, vol. 13, no. 4, pp. 385–399, 2005.

[32] G. Barrette and C. Gosselin, "Determination of the dynamic workspace of cable-driven planar parallel mechanisms," *Trans. of the ASME Journal of Mechanical Design*, vol. 127, no. 2, pp. 242–248, 2005.

[33] B. Duan, "A new design project of the line feed structure for large spherical radio telescope and its nonlinear dynamic analysis," *Mechatronics*, vol. 9, no. 1, pp. 53–64, 1999.

[34] Y. Su, C. Zheng, and B. Duan, "Fuzzy learning tracking of a parallel cable manipulator for the square kilometer array," *Mechatronics*, vol. 15, no. 6, pp. 731–746, 2005.

[35] Y. Terumich, M. Ohtsuka, M. Yoshizawa, Y. Fukawa, and Y. Tsujioka, "Nonstationary vibrations of a string with time-varying length and a mass-spring system attached at the lower end," *Nonlinear Dynamics*, vol. 12, no. 1, pp. 39–55, 1997.

[36] Y. Zhang, H. Pota, and S. Agrawal, "Modification of residual vibrations in elevators with time-varying cable lengths," in *Proc. of the American Control Conference*, Anchorage, AK, May 2002, pp. 4962–4966.

[37] A. Banerjee and V. Do, "Deployment of a cable connecting a ship to an underwater vehicle," *AIAA Journal of Guidance, Control, and Dynamics*, vol. 17, no. 6, pp. 1327–1332, 1994.

[38] A. Makarenko, V. Poddubnyi, and V. Kholopova, "Study of the nonlinear dynamics of self-propelled submersibles controlled by a cable," *International Applied Mechanics*, vol. 33, no. 3, pp. 251–257, 1997.

[39] J. Kamman and R. Huston, "Modeling of variable length towed and tethered cable systems," *AIAA Journal of Guidance, Control, and Dynamics*, vol. 22, no. 4, pp. 602–608, 1999.

[40] A. Misra and V. Modi, "A survey of the dynamics and control of tethered satellite systems," *Tethers in Space, Advances in the Astronautical Sciences, American Astronaitucal Society*, vol. 62, pp. 667–719, 1986.

[41] M. Cosmo and E. Lorenzini, *Tethers in Space Handbook.* Smithsonian Astrophysical Observatory, December 1997, prepared for NASA Marshall Space Flight Center.

[42] J. Kamman and R. Huston, "Validation of a finite segment cable model," *Computers and Structures*, vol. 15, no. 6, pp. 653–660, 1982.

[43] F. Driscoll, R. Lueck, and M. Nahon, "Development and validation of a lumped-mass dynamics model," *Applied Ocean Research*, vol. 22, no. 3, pp. 471–485, 2000.

[44] C. Lambert, M. Nahon, B. Buckham, M. Seto, and X. Zhao, "Dynamics simulation of a towed underwater vehicle system, part ii: Model validation and turn maneuver optimization," *Ocean Engineering*, vol. 30, no. 4, pp. 471–485, 2003.

[45] T. Walton and H. Polacheck, "Calculation of transient motion of submerged cables," *Mathematics of Computation*, vol. 14, no. 69, pp. 27–46, 1960.

[46] S. Huang, "Dynamic analysis of three-dimensional marine cables," *Ocean Engineering*, vol. 21, no. 6, pp. 587–605, 1994.

[47] F. Driscoll and M. Nahon, "Mathematical modeling and simulation of a moored buoy system," in *Proc. of MTS/IEEE Oceans '96*, Fort Lauderdale, FL, September 1996, pp. 517–523.

[48] C. Yamamoto, M. Inoue, and O. Nagatomi, "A study on dynamics of submarine cables during laying and recovering," in *Proc. of the International Offshore Mechanics and Arctic Engineering Conference*, vol. 1B, September 1997, pp. 183–189.

[49] J. Kamman and R. Huston, "Multibody dynamics modeling of variable length cable systems," *Multibody Sytem Dynamics*, vol. 5, no. 3, pp. 211–221, 2001.

[50] P. Bainum and V. Kumar, "Optimal control of the shuttle-tethered-subsatellite system," *Acta Astronautica*, vol. 7, pp. 1333–1348, May 1980.

[51] E. Netzer and T. Kane, "Estimation and control of tethered satellite systems," *AIAA Journal of Guidance, Control, and Dynamics*, vol. 18, no. 4, pp. 851–858, 1995.

[52] R. Lea, J. Villarreal, Y. Jani, and C. Copeland, "Tether operations using fuzzy logic based length control," in *Proc. of IEEE International Conference on Fuzzy Systems*, San Diego, CA, March 1992, pp. 1335–1342.

[53] S. Pradhan, V. Modi, and A. Misra, "Tether-platform coupled control," *Acta Astronautica*, vol. 44, no. 5, pp. 243–256, 1999.

[54] B. Yang and C. Mote, "On time delay in noncolocated control of flexible mechanical systems," *ASME Journal of Dynamic Systems, Measurement, and Control*, vol. 114, no. 3, pp. 409–415, 1990.

[55] C. Wagner-Nachshoni and Y. Halevi, "Control of multi-link flexible structures," in *Proc. of the 2005 IEEE International Symposium on Intelligent Control*, Limassol, Cyprus, June 2005, pp. 507–512.

[56] R. Kalman, "When is a linear control system optimal?" *ASME Journal of Basic Engineering*, vol. 86D, no. 1, pp. 51–60, March 1964.

[57] M. Athans and P. Falb, *Optimal Control: An Introduction to the Theory and its Applications.* New York City, NY: McGraw-Hill, 1966.

[58] R. Kalman and R. Bucy, "New results in linear filtering and linear prediction theory," *ASME Journal of Basic Engineering*, vol. 83D, pp. 95–108, 1961.

[59] *Technical Data Sheet*, Cortland Cable Company.

[60] *Technical Data Sheet, MHD090*, Rexroth Indramat.

[61] *Technical Data Sheet, SP210*, Alpha, SP Low-Backlash Planetary Gear Reducer.

[62] M. Nahon, "A simplified dynamics model for autonomous underwater vehicles," in *Proc. of IEEE Symposium on Autonomous Underwater Vehicle Technology, 1996*, Monterey, CA, June 1996, pp. 373–379.

[63] B. Buckham, M. Nahon, and M. Seto, "Three-dimensional dynamics simulation of a towed underwater vehicle," in *Proc. of OMAE'99, the 18th International Conference on Offshore Mechanics and Arctic Engineering*, St. John's, NL, July 1999.

[64] J. Hamilton, "Vibration-based techniques for measuring the elastic properties of ropes and the added mass of submerged objects," *Journal of Atmospheric and Oceanic Technology*, vol. 17, no. 7, pp. 688–697, 2000.

[65] X. Huang and O. Vinogradov, "Extension of a cable in the presence of dry friction," *Structural Engineering and Mechanics*, vol. 4, no. 3, pp. 313–329, 1996.

[66] E. Genho-Hreiche, "Etude de cables soumis a de fortes tensions," Research Project Report, McGill University, 2004.

[67] B. McCormick, *Aerodynamics, Aeronautics and Flight Mechanics.* John Wiley and Sons, 1995.

[68] I. Abbot and A. V. Doenhoff, *Theory of Wing Sections.* Dover Publications, 1959.

[69] S. Hoerner, *Fluid Dynamic Drag.* 148 Busteed Dr, Midland Park, NJ: Published by author, 1958.

[70] J. Newman, *Marine Hydrodynamics.* Cambridge, MA: MIT Press, 1989.

[71] A. Davenport, "Rationale for determining design wind velocities," *Journal of Structural Division ASCE*, vol. 86, no. ST5, pp. 39–68, May 1960.

[72] ESDU, *Characteristics of Atmospheric Turbulence Near the Ground*, Engineering Sciences Data Unit Item Number 74031, UK, 1974.

[73] B. Etkin, *Dynamics of Atmospheric Flight.* New York: Wiley, 1972.

[74] C. Lambert, M. Nahon, and D. Chalmers, "Study of a multi-tethered aerostat system - experimental observations and model validation," in *Proc. from the 16th AIAA Lighter-Than-Air Systems Technology Conference*, Arlington, VA, September 2005.

[75] J. Bendat and A. Piersol, *Measurement and Analysis of Random Data*. New York City, NY: John Wiley and Sons, 1966.

[76] J. Houbolt, "Atmospheric turbulence," *AIAA Journal*, vol. 11, no. 4, pp. 421–437, 1973.

[77] R. Govardham and C. Williamson, "Vibration-based techniques for measuring the elastic properties of ropes and the added mass of submerged objects," *Journal of Wind Engineering and Industrial Aerodynamics*, vol. 69, no. 71, pp. 375–385, 1997.

[78] P. Coulombe-Pontbriand, "Modeling and experimental characterization of a tethered spherical aerostat," M.A.Sc. Thesis, McGill University, Montreal, Qc., 2005.

[79] P. Coulombe-Pontbriand and M. Nahon, "Experimental characterization and simulation of a tethered spherical helium balloon in an outdoor environmental," in *Proc. of the 16th AIAA Lighter-Than-Air Systems Technology Conference*, Arlington, VA, September 2005.

[80] C. von Wieselsberger, "Weitere festellungen uber dei geset des flussigkeits and luftwiderstandes," *Physikalische Zeitschrift*, vol. 23, pp. 219–224, 1922.

[81] F. Deschenes and M. Nahon, "Design improvements for a multi-tethered aerostat system," in *Proc. of AIAA Flight Mechanics Conference*, San Francisco, CA, August 2005.

[82] H. Kwakernaak and R. Sivan, *Linear Optimal Control Systems*. John Wiley and Sons, 1972.

[83] R. Stefani, B. Shahian, C. Savant, and G. Hostetter, *Design of Feedback Control Systems, Fourth Edition*. Oxford University Press, 2002.

[84] K. Ogata, *Discrete-Time Control Systems*. Upper Saddle River, NJ: Prentice Hall, 1994.

[85] P. Maybeck, *Stochastic models, estimation and control - Volume 1*. New York, NY: Academic Press, 1979.

[86] B. Friedland, *Control System Design - An Introduction to State-Space Methods*. McGraw-Hill Book Company, 1986.